Timekeeping and Accelerometry with Robust Light Pulse Atom Interferometers

by

Krish Kotru

Submitted to the Department of Aeronautics and Astronautics
in partial fulfillment of the requirements for the degree of
Doctor of Philosophy in Aeronautics and Astronautics
at the
MASSACHUSETTS INSTITUTE OF TECHNOLOGY
June 2015

Signature redacted

Author .....
Department of Aeronautics and Astronautics
May 21, 2015

Signature redacted

Certified by ... .
Richard E. Stoner
Distinguished Member of the Technical Staff, C.S. Draper Laboratory
Thesis Supervisor

Signature redacted

Certified by ....
Paulo C. Lozano
Associate Professor of Aeronautics & Astronautics
Thesis Supervisor

Signature redacted

Certified by ....
Vladan Vuletic
Professor of Physics
Thesis Supervisor

Signature redacted

Accepted by ....
Paulo C. Lozano
Associate Professor of Aeronautics & Astronautics
Chair, Graduate Program Committee

Timekeeping and Accelerometry with Robust Light Pulse Atom Interferometers

by

Krish Kotru

Submitted to the Department of Aeronautics and Astronautics
on May 21, 2015, in partial fulfillment of the
requirements for the degree of
Doctor of Philosophy in Aeronautics and Astronautics

Abstract

Light pulse atom interferometry (LPAI) is a powerful technique for precision measurements of inertial forces and time. Laboratory LPAI systems currently achieve state-of-the-art acceleration sensitivity and establish the international atomic time standard. However, the realization of practical LPAI in dynamic environments (e.g., rapidly accelerating or rotating platforms) has been limited in part by atom optics—the analogues to optical beamsplitters and mirrors. Atom optics in traditional LPAIs are composed of resonant laser pulses that are susceptible to variations in optical detuning and intensity expected in sensors designed for dynamic environments. This thesis investigates atom optics that use frequency- and intensity-modulated laser pulses to suppress sensitivity to these inhomogeneities.

For atomic timekeeping applications, a Ramsey LPAI sequence based on stimulated Raman transitions and frequency-swept adiabatic rapid passage (ARP) was developed. Raman ARP drives coherent transfer in an effective two-level atomic system by sweeping the Raman detuning through the two-photon resonance. In experiments with ^{133}Cs atoms, Raman ARP reduced the sensitivity of Ramsey sequences to differential AC Stark shifts by about two orders of magnitude, relative to standard Raman transitions. Raman ARP also preserved fringe contrast despite substantial intensity inhomogeneity. The fractional frequency uncertainty of the ARP Ramsey sequence was limited by second-order Zeeman shifts to $\sim 3.5 \times 10^{-12}$ after about 2500 s of averaging. For accelerometry applications, Raman ARP provided efficient, large momentum transfer (LMT) atom optics in an acceleration-sensitive LPAI. These atom optics produced momentum splittings of up to 30 photon recoil momenta between interfering wavepackets—the largest to date for Raman atom optics. This splitting, in principle, enables up to a factor-of-15 improvement in sensitivity over the nominal interferometer. By forgoing cooling methods that reduce atom number, this LMT method reduces the measurement uncertainty due to atom shot-noise and enables large area atom interferometry at higher data-rates. These features could prove useful for fielded inertial sensors based on atom interferometry.

Thesis Supervisor: Richard E. Stoner
Title: Distinguished Member of the Technical Staff, C.S. Draper Laboratory

Thesis Supervisor: Paulo C. Lozano
Title: Associate Professor of Aeronautics & Astronautics

Thesis Supervisor: Vladan Vuletic
Title: Professor of Physics

Acknowledgments

We see further by standing on the shoulders of giants. Many proverbial giants have bolstered me up during my time as a graduate student, and all these individuals deserve my deepest gratitude. First, I thank my research advisor, Rick Stoner, for being a wonderful mentor over the years. His consideration of the important theoretical questions pertaining to this work provided a firm foundation for my research and served as a textbook example of original scientific thinking. Rick struck a remarkable balance between giving students guidance and supporting new ideas, especially when students became more experienced. Witty and often humorous, he also had a knack for working his favorite idioms into almost any conversation. Listed below are some of his more memorable (and less colorful) lines.

- Regarding a hackneyed idea: "That's about as fresh as a Foghat concert"
- Preamble to making a wish: "Good Lord willing and the creek don't rise, ..."
- On meeting a famous physicist: "Even a cat can look at a king"
- On a dying research project: "It's dead in the water and listing to port"
- Regarding a busy colleague: "That guy's busier than a one-armed paper-hanger"

To access the complete collection of Rick's favorite idioms, contact students in the group or simply have a few conversations with the man himself. I imagine Dave Butts, a recent graduate of our group, would readily corroborate these claims. Being two years ahead of me on a similar trajectory, Dave naturally assumed the role of second mentor during my early days as a graduate student. He provided a blueprint for succeeding in graduate school, which I at least attempted to follow. I'm grateful to him for his camaraderie in the lab, at the gym, behind the mic on occasion, and in life at large. Dave, amongst others, was kind enough to review this dissertation in its unpolished state and make suggestions that undoubtedly improved the quality of the finished product.

I thank members of my thesis committee, Vladan Vuletic, Paulo Lozano, and the late Shaoul "Ziggy" Ezekiel, for taking interest in my work and time out of their busy schedules to periodically meet and discuss my research progress. Ziggy had an impact on students over many decades. As a testament to his sustained influence, several of Ziggy's former students visited him during his final days or paid their respects at his burial, despite his desire to not "bother" anybody. He will surely be missed. As his last advisee, I hope my dissertation would have met his high standards. I also thank Vladan and Paulo for reading my thesis, asking interesting questions, and coming together to fill Ziggy's rather large shoes over the past few months.

At Draper Labs, where I carried out my graduate research, I was fortunate to have worked with and learned from experienced staff members who regularly devoted time to helping students. A prime example is Joe Kinast, who smoothly transitioned to me his software for some crucial laboratory equipment over an extended period of time. Joe was always accommodating when I interrupted his workday—usually to talk shop, but sometimes to gloat/cry over the Yankees. Ever the patient listener, Joe the Pirates fan couldn't quite empathize with these frustrations. He managed, nonetheless, to effectively mask his feelings with inspired and hilarious impressions of Arnold Schwarzenegger. I am also grateful to Justin Brown, who similarly devoted time and energy to reviewing experimental data, carefully revising journal papers, and pushing me to communicate in the clearest way possible. Justin's high-energy, jovial approach to everything from science and love to friendly pranks and added sugar kept my spirits up during difficult stretches in the lab. Equally beneficial to my morale were his donations of Thorlabs snacks, Wisconsin cheese curds, and leftover cookies from catered meetings.

Dave Johnson, another Draper staff member, also frequently made himself available for consultation on experimental problems, especially when I was learning the ropes as a junior student. Dave's genuine optimism and natural curiosity were often reflected in his favorite question for me: "Hey Krish, want to see something cool?" I can only hope these qualities have rubbed off on me. Dave also graciously agreed to review a draft of my thesis and provided valuable feedback, for which I am most

appreciative. Draper staff member Brian Timmons was a valuable resource throughout graduate school, due to his Labview acumen, mastery of optical and vacuum systems, and deep knowledge of laser cooling. Brian brought an easygoing style and a penchant for straight-talk to every conversation, which made it very simple to work or consult with him. Fellow New Yorker Jen Choy was also a pleasure to have in the lab. Though we did not directly work together, Jen still found a way to earn the title of Nicest Person on Earth in my book. Her willingness to lend a hand, find common ground in a technical discussion, loan out lab equipment, and buy me coffee or cafeteria tater tots won't soon be forgotten.

Student researchers at Draper also played important roles in this work and are deserving of my gratitude. Marissa Galfond contributed her Labview skills to our implementation of large area atom interferometry and ran early experiments related to the timekeeping results presented here. Though Marissa chose to pursue other ventures after two years at MIT, her contributions had a lasting impact in our lab, as evidenced by our continued use of the "dataUnbin" VI (what a lifesaver!). Nicole Pomeroy, who recently took on a staff position at Draper, ran experiments on my behalf when I was occupied with thesis or paper writing. Ever-willing to lend a hand, Nicole helped me bakeout the vacuum system, reassemble optics, and move the entire apparatus at various times during the past year. Her organized approach likely saved me time, effort, and even money when it came to avoiding late fees for course registration. I am excited to see what the future holds for Nancy Wu, our newest group member and torchbearer. Nancy has already carried forward our timekeeping work and shown great promise in the lab. Her nuanced portrayal of our group in a hand-drawn Christmas card spoke not only to her subtle sense of humor, but also her observation skills. Many thanks go out to lab technician Paul Jones, who was instrumental in moving my research forward during my first few years in the lab. Paul taught me how to splice, coil, clean, and handle bare optical fiber, and also provided an excellent soundtrack during his tenure in our lab.

I am also grateful to the managerial and administrative staff at Draper, who have come through time and again to secure funding and help me meet short deadlines.

Steve Smith, Tim McCarthy, Tony Radojevic, and Tony Kourepenis championed cold atom sensor development with the higher-ups at Draper, provided extensions and a seemingly endless stream of approval signatures, and supported me at various times as both supervisors and friends. The cultural benefit of Draper's flat hierarchy was well-illustrated when then-CEO Jim Shields took the time to help me become unlost in a hallway near his office. I guess even kings can look at cats, on occasion. I would like to also thank Linda Fuhrman, Stephan Kolitz, and Gail Dourian at the Draper Education Office for running the Draper Laboratory Fellow program, of which I was a beneficiary for many years. On the administrative side, special thanks to Andrea Matos for always finding a way to place my last-minute orders, and to Denise Bilodeau for that thing with the airline tickets. Thanks also to Lei-Sanne Doo and Stacey Goulet for helping me meet publication deadlines.

I spent an amazing month in the Bay Area during the fall of 2014, working with the Kasevich group on the 10-m atom interferometer at Stanford. I would like to thank Mark Kasevich, Rick Stoner, and Draper Labs for making this opportunity possible. Many thanks to Tim Kovachy, Jason Hogan, Christine Donnelly and Chris Overstreet for acquainting me with the sprawling apparatus, creating ample opportunity for contribution, and briefly including me as part of their team. Jesse Gossett, thank you for playing tour guide and making Palo Alto feel a little more like home.

My respites from work were often taken in the company of The Hooligans of 65 Bromfield Road. Justin, Jayson, Jared, Tim, Katz, Scarv, and I made many memories and shared some stitch-inducing laughs over the years. Fortunately, no houses in the Berkshires were burned down in the process.

Finally, I must acknowledge the enduring love and support of my family. My parents, biological and otherwise, have been guilty on occasion of believing in me even more than I believe in myself. While their stubborn faith got me through some tough stretches, genetics were probably helpful too: my mother's drive and my father's curiosity took root in me at an early age and seemingly produced a person capable of scientific endeavors. But even more important was the value Mom, Dad, and Joe placed in education and the simple joy of understanding something. Today,

I am grateful for the boundless love and affection they bestow upon their children. I am also grateful for my grandparents, who played a pivotal role in my upbringing by caring for me when I was a child. Resuming parental duties in their sixties, they mustered the energy to teach me to ride a bike, play Holi in the street, and spell tricky English words correctly. Their roles as parents diminished as I got older, but their interest in my future and well-being was a constant. My sister, Rhea, had the misfortune of having her preschool years coincide with my adolescence. Luckily, she has since forgiven my many youthful transgressions and now even claims to enjoy my company. This outcome is really a testament to Rhea's instinctive kindness and compassion. I thank her for always reminding me of the importance of these human qualities. Thanks also to Hasanain and Nisreen, who reminded me of home and kept me connected to our family traditions, culture, and food while in Boston. My in-laws, MM, DD, and Laura, have also been supportive during my time in graduate school. Their cookie-filled care packages and visits to Boston were a frequent source of joy. Also, their home in Minnesota was a welcome retreat from the hustle and bustle of the Boston–Cambridge area.

Most of all, I am grateful for my wife, Allison, who stood by me through the highs and sporadic lows of lab work, all while making her own journey through medical and journalism school. It is only natural that Allison completed two forms of graduate school in this time, as she does everything at about twice my speed. Her swiftness benefited me too, as it periodically left us with enough spare time to enjoy our personal life (and take naps). Few things are as enjoyable as watching Allison extract happiness from the little stuff, like a Beanie Baby, a chocolate bar, or a walk outside on a nice day. Thank you, Allie, for showing me the joy of little things.

This thesis was prepared at the Charles Stark Draper Laboratory, Inc., under the Internal Research and Development Program. Project ID 30720 Activity ID 001.

Publication of this thesis does not constitute approval by Draper or the sponsoring agency of the findings or conclusions contained herein. It is published for the exchange and stimulation of ideas.

Signature redacted

Krish Kotru

For Allison and my family.

Contents

List of Figures

List of Tables

List of Selected Symbols and Nomenclature

Symbol	Description
$\hbar$	Planck's constant
m	Atomic mass
g	Local gravity
ω_{HFS}	Hyperfine ground state splitting frequency
ω_1, ω_2	Raman laser frequencies
Δ	Single-photon detuning of the Raman laser fields
ϕ_1, ϕ_2	Raman laser phase offsets
φ	Effective Raman laser phase offset $\phi_1 - \phi_2$
$\mathbf{k}_1$, $\mathbf{k}_2$	Raman laser wave vectors
$\mathbf{k}_{\text{eff}}$	Effective Raman wave vector $\mathbf{k}_1 - \mathbf{k}_2$
Ω_1, Ω_2	Single-photon Rabi frequencies of the Raman laser fields
δ	Two-photon Raman detuning
Ω_{eff}	Two-photon Rabi frequency
δ_{AC}	Difference between the AC Stark shifts of the hyperfine ground states
$\mathbf{\Omega}_{\text{gen}}$	Raman pulse "drive field" on the Bloch sphere; $\lvert\mathbf{\Omega}_{\text{gen}}\rvert = \sqrt{\delta^2 + \Omega_{\text{eff}}^2}$
$\hat{\mathbf{p}}$	Bloch vector
$\mathbf{p}_{\parallel}$	Projection of the Bloch vector onto the drive field
T	Interferometer dwell time
t_π	Duration of Raman π pulse

T_π	Duration of Raman ARP inversion pulse
δ_{max}	Maximum detuning of Raman ARP frequency sweep
Ω_{arp}	Overall coefficient of Raman ARP frequency sweep function
β	Free parameter in ARP intensity modulation function
N	Large momentum transfer order
τ_{lmt}	Time between beamsplitter augmentation pulses in large area interferometers
ω_r	Two-photon recoil frequency

ARP	Adiabatic rapid passage
BEC	Bose Einstein condensate
CSAC	Chip-scale atomic clock
FOG	Fiber-optic gyroscope
LMT	Large momentum transfer
LPAI	Light pulse atom interferometry
MOT	Magneto-optical trap
NMR	Nuclear magnetic resonance
OCXO	Oven-controlled crystal oscillator
PIGA	Pendulous integrating gyroscopic accelerometer
RLG	Ring laser gyroscope

Chapter 1

Introduction

Self-contained sensors of motion and time are vital to many technological and scientific applications, including navigation, communication, and network synchronization. Detailed information about these physical quantities can be encoded in the quantum wave-like nature of matter. To extract this information, matter-waves must be interfered in a manner analogous to the interference of light. Laboratory demonstrations of matter-wave interferometry have already produced precise measurements of acceleration, rotation rate, and gravity gradients, as well as stable timing references. With an eye toward practical applications, this work develops atom interferometry techniques for inertial sensing and timekeeping.

1.1 Inertial sensing

Inertial navigators use onboard accelerometers and gyroscopes to respectively measure linear acceleration and either rotation rate or angle. The measurements are integrated to determine position, velocity, and orientation. Inertial navigation is desirable when external references, such as the Global Positioning System (GPS) or star-sightings, are either unavailable or unreliable. Applications include air and spacecraft navigation, underwater and indoor navigation, and satellite pointing.

Like all forms of dead reckoning, inertial navigation is susceptible to accumulated measurement errors. Consider an accelerometer with a fixed bias of $\Delta a = 0.01$ m/s^2.

After $t = 1$ hr of operation, the resulting position offset is $\Delta x = \Delta a t^2/2 = 65$ km. If the offset is replaced by a white noise process, a sensor that averages the noise down to $\Delta a = 0{:}01$ m/s^2 in 1 s would produce a position uncertainty of $\Delta x = \Delta a t^{3/2}/\sqrt{3} = 1.2$ km after $t = 1$ hr of operation. Navigation applications with stringent stability and accuracy requirements typically rely on inertial sensors that heavily suppress these measurement errors. Accelerometers that currently satisfy these requirements, such as the Pendulous Integrating Gyroscopic Accelerometer (PIGA), are electromechanical in nature. PIGAs measure acceleration using a sensing element based on a spinning rotor attached to a pendulum. With the rotor spinning about the x axis, and the pendulum free to swing about the y axis, an input acceleration along the z axis—which would cause an ordinary plum bob to swing—induces precession of the spinning rotor in the x-y plane. Acceleration is determined by measuring the angular rate of precession (velocity is determined by the total angle). Refinements to this physical concept spanned multiple decades, ultimately resulting in perhaps the most stable and accurate accelerometer ever made: the Specific Force Integrating Receiver (SFIR) [1]. PIGA-like accelerometers achieve bias stabilities of $\sim$1 μg [2], significantly outperforming other presently available accelerometer technologies, as shown in Table 1.1 (see Appendix A for background on the Allan variance, sensitivity, and bias stability). Electromechanical instruments, however, require expensive and specialized materials, as well as highly-skilled labor for assembly. A single SFIR accelerometer, for instance, requires six months for the assembly of its 19,000 components [1]. As a result, inertial sensor development has moved toward technologies based on microelectromechanical systems (MEMS), optical interference, and frequency metrology with atoms.

Technology	Bias stability (μg)	Applications
Electromechanical [2]	1	Missile & submarine guidance
MEMS [3]	10	Aircraft navigation
Consumer MEMS [4]	>10,000	Electronics
Atomic [5]	<1	Inertial-only navigation

Table 1.1: Applications and the best demonstrated bias stabilities for various accelerometer technologies.

MEMS-based inertial sensors achieve miniaturization and economy in bulk manufactured devices that are ideal for consumer electronics [4]. At present, PIGAs continue to outperform the best MEMS accelerometers, which often suffer from intrinsically poor long-term stability (though suitable MEMS options for aircraft navigation are available [3]). Inertial sensors based on optical interference have primarily impacted rotation sensing. The ring laser gyroscope (RLG), for example, measures rotations using the interference of two laser beams that counter-propagate in a ring. The fiber-optic gyroscope (FOG) senses rotation by interfering laser beams that have counter-propagated through compact coils of kilometer-long optical fiber. Compared to RLGs, FOGs achieve significant volume reduction through the use of coiled fibers. As a result, FOGs are poised to replace electromechanical instruments used for ballistic missile guidance [6]. Optical accelerometers also measure inertial forces through interference. In one such device, deflections of a flexured mass are detected using interference in a Michelson interferometer [6]. Another approach involves passing light through an optical fiber with an embedded Bragg grating (i.e., modulated index of refraction). A proof mass is attached to one end of the fiber so that accelerations along the fiber axis alter the periodicity of the grating. Since the grating periodicity affects the wavelength of the transmitted light, accelerations create shifts in optical frequency that are detected interferometrically [7]. These devices offer high bandwidth and serve as excellent vibration sensors.

Advances in electro-optics and vacuum cell fabrication have also kindled interest in atom-based sensors. In particular, the potential for high precision inertial sensing with atom interferometry was evident from initial demonstrations in the early 1990s [8]. Atom interferometers have since produced measurements of local gravity, gravity gradients, and rotation rate that are competitive with state-of-the-art methods. Atomic sensors generally exhibit excellent long-term stability, because their measurements are referenced to quantum energy-level structures that are inherently stable and well-characterized. Atom interferometers, in particular, benefit from solid-state designs (no moving parts) that are capable of sensing rotation, acceleration, gravity gradients, and time using the same measurement paradigm. These features could

drive substantial reductions in maintenance and manufacturing costs. The demonstrated performance of atom interferometers also could enable inertial-only navigation with meter-scale position accuracy over tens of minutes. Such a navigator would obviate the need for GPS in missions of <1-hour duration.

One example of the remarkable performance offered by atom interferometric inertial sensors is a gravimeter that achieved a sensitivity of $\sim$4 ng after 1 s of averaging [5]. By comparison, the short-term stability of the best commercially-available gravimeter—an optical Michelson interferometer with a free-falling corner cube reflector—is roughly 3 times worse [9]. Atomic gravimeters have also provided evidence for detailed tidal effects [10]. Operating two such interferometers at different positions in a gravitational field results in a highly sensitive gravity gradiometer [11]. A sensor in this configuration was used to measure the Newtonian gravitational constant G by monitoring changes in the gravity gradient due to motion of a large proximate mass [12]. The result agreed with the accepted value of G to within 1.5 standard deviations and required a short-term sensitivity to differential acceleration of 3 ng$/\sqrt{\text{Hz}}$, as well as an accuracy of 5×10^{-11} g [13]. However, a more traditional measurement of G, based on deflections of a torsion balance, still achieves a fractional uncertainty that is a factor of 11 smaller than that of the atomic measurement [14].

The first high-precision gyroscope based on atom interferometry achieved a sensitivity of 2 μdeg$/\sqrt{\text{hr}}$ using an atomic beam that propagated over a 2-m baseline [15]. This technique was improved upon in another atomic beam gyroscope, which through tracking of temperature-driven fluctuations in laser beam parameters, achieved a long-term stability of 68 μdeg/hr at 10^4 s [16]. Mature optical gyroscope technologies, however, still outperform their atomic counterparts: a large 16-m^2 RLG achieved a short-term stability of 1.3 nano-deg$/\sqrt{\text{hr}}$, as well as long-term stability that enabled detection of Earth's Chandler wobble at 26.6 nHz [17]. More compact, high-performance FOGs provide short-term stability of 80 μdeg$/\sqrt{\text{hr}}$ and bias stability of 300 μdeg/hr [18].

The state-of-the-art atom interferometry demonstrations described above required large vacuum chambers, floated optical tables, and high-power electro-optical systems

to establish a suitable environment. To address a wide range of applications, significant reductions in the size, weight, and power of these instruments will be necessary. Equally important will be the development of robust interferometry techniques that maintain sensitivity in dynamic environments.

1.2 Precision timekeeping

Stable and precise clocks are essential to a broad range of technologies, including GPS, distributed networks, communication systems, and laboratory instruments. Modern clocks tell time by counting the cycles of a repeatable oscillation, such as those of a swinging pendulum. If each swing occurs over the same period dt, the number of swings M indicates that a time $t = Mdt$ has passed. Of course, the period of any real mechanism changes slightly from one oscillation to the next, leading to errors that grow with time. To minimize these timing errors—and thereby improve accuracy—clockmakers generally use the most stable oscillatory mechanism available. Over the past four centuries, the search for a better mechanism has led from swinging pendulums to atomic oscillators, and timing accuracy has consequently improved by about 10 orders of magnitude.

Today, the most stringent timing applications require atomic clocks based on atom interferometry. The international time standard, for example, is currently realized by an ensemble of atomic clocks, the best of which achieves a fractional frequency uncertainty of 3×10^{-16} [19]. At this performance level, time can be tracked at the ~10-ps level for 24 hours. The technological benefits of such accurate timekeeping are manifest in everyday life: cellular networks, electrical power grids, and GPS navigation all rely on microsecond-level timing at a fundamental level [20]. But how is this timing information globally distributed? The atomic clocks that set international time require room-sized devices, with demands on environmental control that preclude operation in a dynamic environment. Commercially available atomic clocks with good long-term stability are considerably smaller, but still occupy ~30-L packages, weigh ~30 kg, and only operate stably in controlled environments [21]. Since

high-performance atomic clocks cannot yet be widely distributed, accurate time is disseminated internationally through the GPS constellation [22]. Each GPS satellite uses multiple onboard atom clocks, along with corrections from the master clock of the U.S. Naval Observatory, to distribute timing information that is accurate to within 1–10 ns. When GPS becomes unavailable, oven-controlled crystal oscillators (OCXOs) typically substitute as primary references (see Table 1.2 for a performance comparison). These clocks, however, are only accurate to within a microsecond for several hours. Applications that require sub-microsecond accuracy over longer periods of time stand to benefit from onboard or locally available atomic references [20].

Portable atomic clocks recently achieved an important developmental milestone with the advent of chip-scale atomic clocks (CSACs). CSACs are non-interferometric clocks that probe resonance frequencies derived from alkali-metal atoms in high-pressure vapor cells. In a 17 mL package, and with power consumption of just 120 mW, CSACs provide a fractional stability of $2.5 \times 10^{-10}/\sqrt{\tau}$ [23, 24, 25]. Their long-term stability, however, is limited to $\sim 10^{-11}$ at 1000 s by pressure-dependent frequency shifts [26, 27]. As a result, CSACs serve as secondary references, which require periodic external corrections. Between CSACs and laboratory-scale clocks, there remains a vast, unpenetrated performance-space for primary frequency references that operate in a small volume and beyond the laboratory environment.

Technology	Short-term stability	Long-term stability
OCXO [28]	1×10^{-12}	1×10^{-12} at 10^1 s
CSAC [23]	2.5×10^{-10}	1×10^{-11} at 10^3 s
Rb vapor cell [28]	1×10^{-11}	1×10^{-12} at 10^4 s
Cs beam [21]	5×10^{-12}	$<1 \times 10^{-14}$ at 10^6 s
NIST-F2 [19]	2×10^{-13}	$<4 \times 10^{-16}$ at $>3 \times 10^4$ s
Optical [29]	3×10^{-16}	$<6 \times 10^{-18}$ at $>10^4$ s

Table 1.2: Performance specifications for several clock technologies. For atom-based devices, the short-term stability generally averages down with a slope of $\tau^{-1/2}$ from 1 to 100 s or longer. The atomic fountain clock, NIST-F2, provides the US contribution to international atomic time. "Optical" refers to clocks that probe atomic transitions at optical frequencies. They offer unsurpassed stability and accuracy, but are currently limited to laboratory environments. The reported long-term stability limits of these last two clocks are due not to flicker noise, but to limits of total operation time.

Compact and robust clocks based on atom interferometry may fill this void in the near future. In the early 1990s, a demonstration of a compact atom interferometric clock achieved a fractional frequency stability ($6.5 \times 10^{-12}/\sqrt{\tau}$ [30]) that was competitive with the best commercially-available atomic clocks. A more recent reincarnation of this approach reduced the volume required for atom collection, preparation, and measurement to ~15 mL [31, 32]. Both these demonstrations relied on microwave radiation to perform atom interferometry. Microwave interrogations often require cavities or waveguides that fundamentally limit size-reduction and add complexity. An alternative method, which is explored in this thesis, uses laser pulses to drive atomic transitions between energy levels spaced by microwave frequencies. Atom interferometric clocks based on laser pulses have achieved fractional frequency uncertainties of 2×10^{-12} at 1000 s [33]. Another promising technique, which provides excellent long-term stability, relies on non-interferometric spectroscopy of trapped ions. A compact Ytterbium ion clock, for example, maintained stable operation over many days, resulting in a fractional uncertainty of $\sim 10^{-14}$ [34]. The development of compact ion clocks is presently limited by reliance on expensive ultraviolet laser sources.

1.3 Light pulse atom interferometry

1.3.1 Basic principles

The first four unique realizations of neutral atom interferometers were reported over a six-week period in 1991. One of these demonstrations used microfabricated slits to produce the atomic analog of Young's double-slit experiment [35]. Measurements of the spatially-varying atomic interference pattern are shown in Fig. 1-1. Another approach used diffraction gratings to create an atomic Mach-Zehnder interferometer [36]. The final two demonstrations used light pulse atom interferometry (LPAI), in which single-photon [37] and two-photon laser pulses [38] diffracted the atom wavepackets. LPAI has historically been the most successful method for inertial sensing and is an

area of continued interest for atomic timekeeping. Nevertheless, these early interferometry demonstrations paved the road for precise measurements of fundamental constants, atomic and molecular properties, and inertial forces. In a remarkable example of the progress to date, one recent demonstration of matter-wave interferometry produced interference in complex organic molecules composed of up to 430 atoms [39].

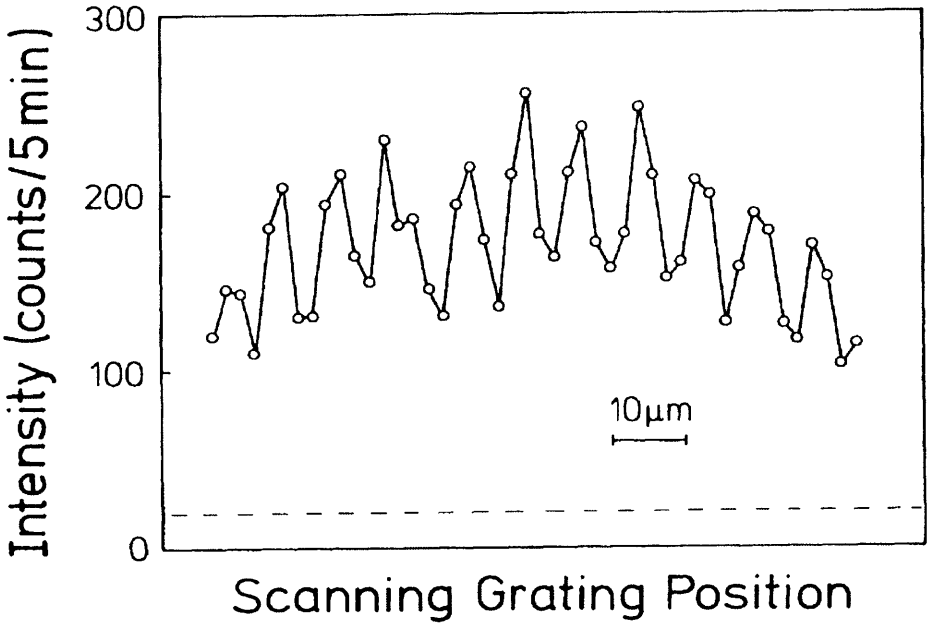

Figure 1-1: Experimental results from the first atomic anologue of Young's double-slit experiment. A collimated beam of helium atoms impinged on a screen containing a microfabricated slit. The transmitted atoms traveled farther downstream toward a second screen with two closely-spaced slits. Behind the second screen, a spatially-varying atomic interference pattern was detected with an atom counter. Troughs (peaks) in the measurements represent detector locations where the probability of seeing an atom was minimized (maximized). Reprinted with permission from [35].

At a basic level, atom interferometry can be understood through analogies with optical interferometers. Consider the optical Mach-Zehnder interferometer, shown in Fig. 1-2a. Light entering the first beam splitter is coherently divided into two paths, reflected by mirrors, and superposed by the final beam splitter. If we assume the beams are perfectly overlapped after the final beam splitter, the intensity measured at the optical detector is proportional to $\cos[k\Delta x + \Delta\phi]$, where k is the optical wave

number, Δx is the difference in path lengths between the interferometer arms, and $\Delta\phi$ is the difference in phase offsets. Path length changes clearly shift the relative phase, which perturbs the optical powers at the output ports of the second beam splitter. Measurements of the optical power are thus sensitive to path lengths shifts at the nanometer-scale. In a general sense, the same holds true for an atom traversing the analogous interferometer in Fig. 1-2b. The matter wave in this case represents a probability amplitude of atom location, and "atom optics" are fashioned from laser pulses or material gratings.

Unlike photons, atoms are massive particles that interact strongly with external potentials and have complex internal structure. These features make the phase of the atomic matter wave a sensitive tool for precision measurements. As a simple example, consider a Mach-Zehnder interferometer in which the upper arm experiences a locally different potential energy U_o due to gravity. Time evolution of the quantum state[1] in this arm induces a phase shift of $\Delta\phi = mU_oT/\hbar$ relative to the state in the lower arm, where m is the atomic mass and T is the time spent in U_o. As $\Delta\phi$ varies from 0 to π rad, the probability that the detector in Fig. 1-2b senses the atom will vary from 0 to 1. Importantly, the sensitivity to U_o scales with T, the measurement interval. In the 1970s, this scenario was realized experimentally in a neutron Mach-Zehnder interferometer [40, 41]. The plane of this interferometer was vertically oriented so that each arm experienced a different gravitational potential.

A theoretical comparison of atomic and optical Mach-Zehnder interferometers illustrates the remarkable sensitivity afforded by the use of atoms. In a phenomenon known as the Sagnac effect, waves passing through a Mach-Zehnder interferometer experience path length shifts induced by rotation rates. In Fig. 1-2, both interferometers are sensitive to rotation about the axis normal to the page. The Sagnac phase is proportional to $A/(\lambda v)$, where A is the area enclosed by the interferometer, λ is the de Broglie or optical wavelength, and v is the wave propagation speed. The ratio

[1]The unitary time evolution adds a phase factor $e^{iHT/\hbar}$ to the quantum state, where H is the time-independent Hamiltonian.

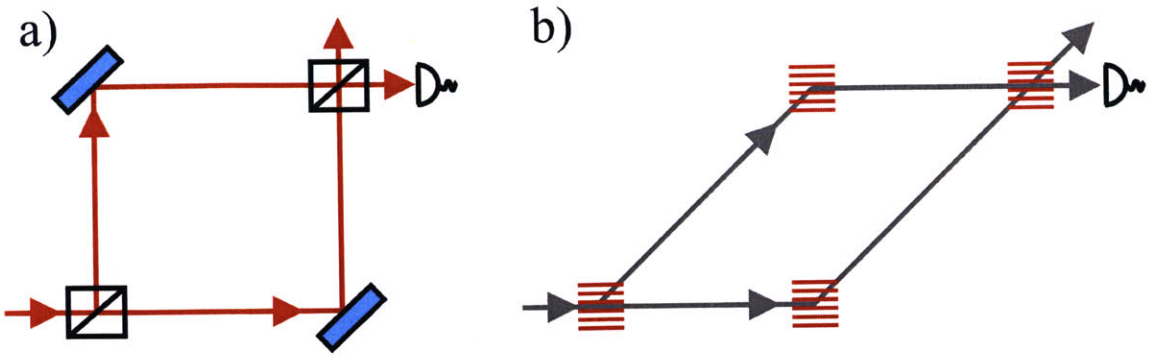

Figure 1-2: Mach-Zehnder interferometers for atoms and light. a) A laser beam incident from the left is divided by a beam splitter, reflected, and recombined by a second beam splitter. A photodetector monitors the optical power after the second beam splitter, providing a sensitive measure of shifts in the optical phase difference between the interferometer arms. b) In the analogous atom interferometer, an atom incident from the left is coherently divided, deflected, and recombined by atom optics, which act as beam splitters and mirrors. The atom optics are either laser pulses or mechanical gratings and slits. The probability of an atom exiting the interferometer through a particular output port is affected by shifts in the relative phase between wavepackets in each interferometer arm perturb.

of Sagnac phase shifts arising from matter versus electromagnetic waves is

$$\frac{\phi_{at}}{\phi_{em}} = \frac{c\lambda_{em}}{v\lambda_{at}}\frac{A_{at}}{A_{em}} = \frac{mc\lambda_{em}}{h}\frac{A_{at}}{A_{em}} \approx 10^{10}\frac{A_{at}}{A_{em}}. \tag{1.1}$$

For typical atomic and optical interferometers, $A_{at}/A_{em} = 10^{-7}$ [42]. Therefore, atom interferometers enhance the Sagnac phase shift by roughly three orders of magnitude—an attractive prospect for precision rotation sensing.

1.3.2 Measurement overview

In our apparatus, an LPAI produces a stream of discrete atomic phase measurements. During each measurement cycle, alkali-metal atoms in ultrahigh vacuum ($<10^{-8}$ Torr) are cooled to extremely low temperatures and then interfered. Cooling the atoms to microkelvin temperatures (~1-cm/s velocities) enables dramatic reductions in sensor size, since the atom sample remains inside a small volume throughout the measurement. To achieve microkelvin temperatures in ~1-100 ms, we employ laser cooling, in

which three orthogonal pairs of counter-propagating laser beams are overlapped and red-detuned with respect to an atomic transition, as depicted in Fig. 1-3a. This configuration produces optical forces that damp out atom motion in the overlap region. The addition of a magnetic quadrupole field in this region produces a position-dependent optical force that, together with the damping force, creates a stable trap [43]. This magneto-optical trap (MOT) was first demonstrated with sodium atoms in 1987 [44] and has since become a ubiquitous tool in atomic physics. Atomic beams serve as viable alternatives to the MOT [42]. However, over a fixed measurement time, a beam requires larger volumes to generate, contain, and interrogate atoms moving at ~100-m/s velocities. In a fixed volume, atomic beams also shorten the available interrogation times, which can degrade sensitivity.[2]

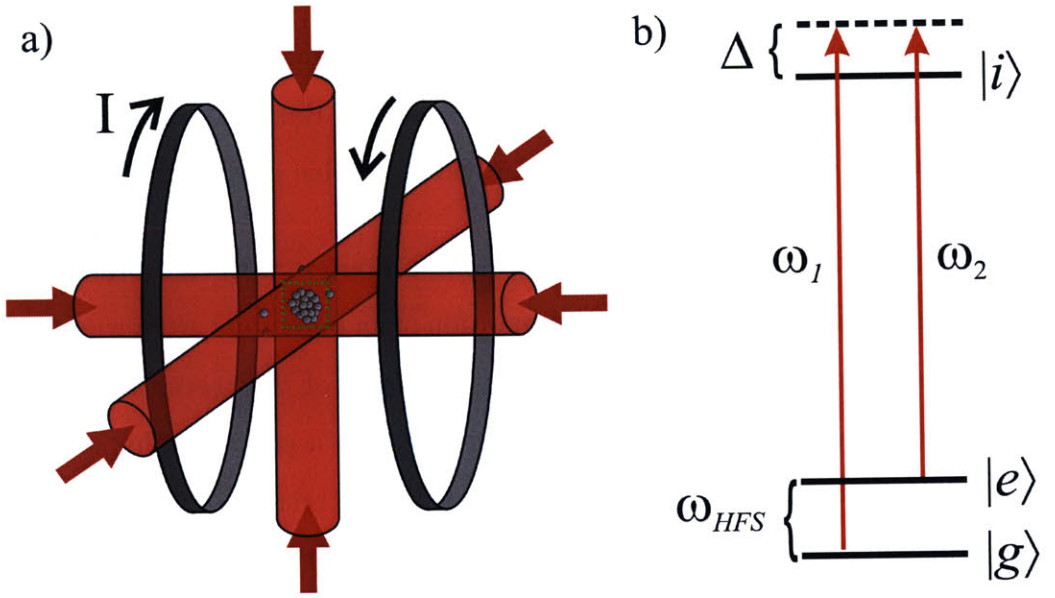

Figure 1-3: Atom trapping and atom optics. a) Three pairs of counter-propagating lasers are orthogonally oriented, overlapped, and red-detuned from an atomic transition frequency. Atoms in the overlap region (dotted green box) experience a velocity-damping force. To produce a position-dependent restoring force, anti-Helmholtz coils supply a quadrupole magnetic field that appropriately shifts the atomic resonance via the Zeeman effect. b) A stimulated Raman transition, in which two photons with frequencies ω_1 and ω_2 transfer atoms between the hyperfine ground states $|g\rangle$ and $|e\rangle$ when $\omega_1 - \omega_2 \approx \omega_{HFS}$. Each Raman frequency is detuned by Δ from the intermediate excited state $|i\rangle$ to suppress single-photon transitions.

[2]The higher atom flux of a beam balances this loss of sensitivity in some interferometers.

We begin LPAI once the trapped atoms have been sufficiently cooled and prepared in the correct internal energy state. At that point, a millimeter-scale cloud of $\sim 10^6$ atoms, which is free of any mechanical contacts, falls under the influence of gravity and other environmental potentials. A sequence of *atom optics* are applied to the cloud to create the LPAI during this time. The atom optics are short laser pulses that drive two-photon, stimulated Raman transitions (depicted in Fig. 1-3b). To coherently separate and recombine the atom wavefunction, the Raman process requires a frequency difference between the two photons, $\omega_1 - \omega_2$, that matches the atomic resonance frequency ω_{HFS} between hyperfine ground states $|g\rangle$ and $|e\rangle$ [38]. Raman transitions will be discussed further in Sec. 2.1. The frequency spacings between levels $|g\rangle$ and $|e\rangle$ in alkali-metal atoms are GHz-scale. Stability requirements on the Raman difference frequency are thus easily achieved with standard RF electronics. Raman transitions are also readily driven by commercially-available diode lasers. Depending on the sequence of atom optics, an LPAI based on Raman transitions measures inertial forces and external potentials, or provides a stable reference frequency.

It is emphasized that atoms in the LPAI do not interfere with each other. Interference results from the division and recombinantion of an individual atom wavefunction. During the interferometer, shifts in the relative phase of the *wavepackets* alter the probability that an atom will exit the interferometer in a particular hyperfine state. To access this probabilistic information—and thus the relative phase—we build up counting statistics by interfering many identical, non-interacting atoms simultaneously.[3] The probability is then determined by the fraction of atoms in each hyperfine state, which we measure using laser-induced fluorescence. Following this readout process, the measurement cycle is restarted with the trapping of a new cloud of cold atoms.

[3] A similar situation arises when assessing the probability of landing heads or tails with a weighted coin. Individual tosses result in either heads or tails. But if q identical coins are tossed, the probability of landing heads can be determined with an uncertainty of $1/\sqrt{q}$.

1.4 Progress toward atom interferometry in dynamic environments

In this section, we describe research efforts aimed toward demonstrating sensitive atom interferometry in dynamic environments. The discussion focuses on size-reduction, robust atom optics, and large area atom interferometry.

1.4.1 Mobility and size

Work towards reducing the size of atom interferometers is underway. A compact gravimeter was demonstrated at Draper Laboratory [45, 46], with interferometry and atom trapping occurring inside a small octagonal glass cell (2.75" in diameter, 1.5" thick, 80 mL). The apparatus used short interrogation times of 2 to 10 ms to help achieve data-rates ranging from 2–10 Hz. High data-rates are necessary for inertial sensors to maintain bandwidth and detect time-varying inputs in dynamic environments. Because of the short interrogation, atoms remained inside a 1-cc volume throughout the measurement. This system achieved sensitive interferometry while retaining key features for size-reduction (e.g., short interrogations, small cell, no atomic fountain or 2D MOT). A similar subsequent effort achieved data-rates ranging from 50-330 Hz using a quartz vacuum cell of dimensions $14 \times 16 \times 80$ mm^3 [47]. The substantial increase in data-rate was due to the recapturing of cold atoms. Since the atom cloud after the interferometer was colder and denser than the background vapor, the atom trapping time was substantially reduced. In addition to high data-rates, this apparatus achieved acceleration sensitivities ranging from 0.57 to 36.7 $\mu g/\sqrt{\text{Hz}}$. Follow-up efforts have produced simultaneous measurements of acceleration and rotation rate with similar sensitivities (64 $\mu\text{rad}/\sqrt{\text{hr}}$) at 60-Hz data-rates [48]. A compact atomic gyroscope has also been demonstrated with cold atoms that were guided [49]. Atoms trapped in a straight magnetic guide were split and recombined using standing wave laser pulses, and the guide was translated laterally with respect to the beam. This motion allowed the wavepacket trajectories to enclose a spatial area and thereby

sense rotation. Since the wavepackets traversed the loop multiple times during an interferometer, this method may provide a path toward compact atomic gyroscopes with large effective areas.

Recent developments in mobile atom interferometry have proceeded in dramatic fashion. LPAI has already been demonstrated aboard a plane in 1 g and 0 g environments [50, 51]. In these efforts, large accelerations were coarsely measured with mechanical sensors and then finely resolved with the atom interferometer. This hybrid approach exploited the wide dynamic range of mechanical instruments and the extreme sensitivity of atomic sensors. The same concept is being employed in the Chip-Scale Combinatorial Atomic Navigator [52], which aims to provide inertial navigation in GPS-denied environments. One of the earliest portable atomic inertial sensors was a gradiometer that achieved a differential acceleration sensitivity of 4.2 $\mathrm{n}g/\sqrt{\mathrm{Hz}}$ in a laboratory environment [53]. The apparatus included two atom interferometers connected over a 70 cm baseline. Each sensor was packaged in a 30-cm cube containing the vacuum chamber, readout system, and optics. A box truck transported the sensor to survey the local gravity gradient with an accuracy of 7×10^{-9} s^{-2} [54]. The vacuum components and electro-optic systems were also employed in the parallel development of a portable gyroscope [55] that achieved a rotation rate sensitivity of 295 $\mu\mathrm{deg}/\sqrt{\mathrm{hr}}$ [56].

1.4.2 Robust atom optics

In dynamic environments, Raman laser beam intensity and frequency errors will be challenging to control, due to atom cloud motion in a Gaussian spatial intensity distribution and light-induced perturbations of the atomic resonance frequency. Intensity gradients in the Gaussian beam limit the fidelity of atom optics acting on a spatially distributed atom cloud, and strongly degrade fringe visibility (i.e., signal-to-noise ratio) if the cloud accelerates transverse to the beam axis, into regions with large gradients. For example, a transverse acceleration of $5g$ during a 10-ms interferometer places the atom cloud at the 1σ intensity radius of a Gaussian beam with 1-cm diameter (typical beam width), where the intensity gradient is nearly maximized. Also

problematic are light shifts of the atomic resonance frequency, induced by interactions between the atom electric dipole moment and oscillating electric fields in the Raman laser pulses. These so-called AC Stark shifts perturb the clock interferometer phase and, in turn, could limit the frequency stability.

Atomic sensors in dynamic environments will benefit from atom optics that suppress systematic effects associated with detuning and intensity variation. Promising candidates for robust atom optics are stimulated Raman transitions that incorporate adiabatic rapid passage (ARP) or composite pulses—both of which were originally developed to mitigate analogous problems in the physics of nuclear magnetic resonance (NMR) [57, 58]. In ARP, efficient atom population transfer results from slowly sweeping the Raman difference frequency through the atomic resonance and modulating the optical intensity [59, 60]. Composite pulses, on the other hand, typically use resonant pulses with fixed intensity, but add discrete phase shifts between contiguous "subpulses" of varying duration. These NMR techniques translate well to Raman transitions given the isomorphism between NMR and Raman processes (discussed in Sec. 2.1.1). Raman ARP was proposed in the context of molecular spectroscopy [61] and has been discussed theoretically [62, 63]. Raman composite pulses have also been proposed as efficient atom optics for interferometry [11, 64].

The traditional approach to adiabatic rapid passage involves linearly sweeping the field detuning. Linear sweeps generally require excessively long pulses or limit the magnitude of initial and final detunings. Several frequency sweeps have been proposed that significantly shorten the pulse duration without sacrificing population transfer efficiency [60, 65]. Theoretical motivations for the various sweep functions will be discussed in Sec. 2.3. NMR physicists have more recently formalized methods for numerically designing fast, broadband adiabatic sweeps [66, 67, 68]. A review of these techniques can be found in [69]. Composite pulse techniques have been similarly developed [70] to compensate field inhomogeneities and detuning offsets in NMR applications. A recent experimental study of composite pulses with stimulated Raman transitions identified several pulses that could prove useful for LPAI [64].

Adiabatic transfer has already been demonstrated outside the realm of NMR.

The first demonstration of optical ARP, used the energy level-spacing between two rotational states in ammonia. The level-spacing was slowly changed via application of an external electric field, such that the molecular resonance passed through the optical frequency of an incident laser [71]. Optical adiabatic passages are also possible in multilevel systems. Coherent transfer across nine Zeeman sub-levels has been demonstrated in cesium by adiabatically raising and lowering the intensities of two temporally-delayed laser pulses [72]. This scheme delivered $8\hbar k$ worth of momentum to the atoms, but functioned only as a deflector. A related technique, known as stimulated Raman adiabatic passage (STIRAP), uses temporally-delayed laser pulses with Raman transitions to coherently split and reflect atom wavepackets. This approach fundamentally differs from ARP, as STIRAP requires unique intensity modulations of each Raman laser field, which furthermore carry fixed and (typically) resonant frequencies [73, 74]. STIRAP was used to demonstrate the first atom interferometer with atom optics based on adiabatic passage [75]. Later, a measurement of the photon recoil frequency with these atom topics was interpreted as a precise measurement of the fine structure constant [76].

1.4.3 Enhancement of inertial sensitivity

Atom interferometric inertial sensors in dynamic environments must operate at relatively high data-rates ($\sim$100 Hz) to maintain suitable bandwidth, as discussed in Sec. 1.4.1. A natural consequence of fast data-rate is shortened measurement times, which significantly reduce interferometer sensitivity. The accelerometer sensitivity, for example, depends quadratically on measurement time. Laboratory gravimeters often use measurement durations of 100 ms, whereas a dynamic environment sensor would likely shorten this time to 5 ms. The phase shift for a given acceleration would correspondingly shrink by a factor of 400.

Sensitivity can be enhanced, without sacrificing data-rate, by increasing the effective area enclosed by the interferometer. In a fixed interrogation time, area enlargement requires atom optics that increase momentum transfer beyond $2\hbar k$ (the nominal case). One method for achieving large momentum transfer (LMT) involves applying

additional light pulses that separate the atom wavepackets farther apart. A proof-of-principle demonstration of this technique used Raman transitions to produce $6\hbar k$ of momentum transfer and a threefold increase in phase shift per unit acceleration [77]. Other promising methods for LMT include using beam splitters based on Bragg transitions and optical standing waves (i.e., optical lattices). Interferometry with Bragg transitions and ultracold atoms ($\sim$100 nK) has already resulted in coherent beam-splitters that transfer $\sim$1-m/s velocities ($102\hbar k$ worth of momentum) to the diffracted wavepacket. This interferometer took an important step toward realizing large spatial separation between atom wavepackets [78]. An alternative method for LMT involves separating the wavepackets with a Bragg transition and then further accelerating them with optical lattices. An experimental demonstration of atom interferometry with this technique achieved $24\hbar k$ momentum separation between diffracting wavepackets [79]. Both these approaches were limited by the purity of optical phase fronts, though this problem could be mitigated with higher-quality optics. Optical lattices have also been proposed as atom waveguides that could transfer $\sim 10^3\hbar k$ of momentum to the interferometer arms. This approach may lead to order-of-magnitude increases in interferometer sensitivity [80].

Most of these demonstrations, however, relied on cooling methods (e.g., evaporative cooling and velocity selection) that typically discard the vast majority of the laser cooled atom sample. Discarding atoms degrades the atom shot-noise-limited measurement uncertainty and also lowers data-rate, since cold atoms can no longer be recaptured by the MOT. In this work, we use broadband ARP and composite pulse atom optics to efficiently create LMT with the entire laser cooled sample. Use of the entire sample implies that our approach is compatible with high data-rate operation, and thus useful for dynamic sensing applications.

1.5 Thesis contributions

The contributions in this thesis fall into two broad categories: timekeeping and accelerometry.

1. With regard to the former, we present a method for robust timekeeping in which alkali atoms are interrogated in a Ramsey sequence based on stimulated Raman transitions. To suppress systematic effects introduced by differential AC Stark shifts and optical intensity gradients, we employ atom optics derived from frequency-swept Raman ARP. Our experimental implementation of Raman ARP reduced the phase sensitivity of Ramsey sequences to Stark shifts in ^{133}Cs atoms by about two orders of magnitude, relative to fixed-frequency Raman transitions. This technique also preserved Ramsey fringe contrast for cloud displacements reaching the $1/e^2$ intensity radius of the laser beam. In a magnetically unshielded apparatus, second-order Zeeman shifts limited the fractional frequency uncertainty to $\sim 3.5 \times 10^{-12}$ after about 2500 s of averaging.

2. With regard to accelerometry, we demonstrate large momentum transfer atom optics in an LPAI using atom optics based on frequency-swept Raman ARP. These atom optics produced high contrast and maintained coherence for momentum splittings of up to 30 photon recoil momenta in an acceleration-sensitive interferometer. We experimentally verified the enhancement of phase shift per unit acceleration and used Monte Carlo simulations to study loss of interferometer contrast. By forgoing evaporative cooling or velocity selection, both of which substantially reduce atom number, our method improved the atom shot-noise limit and enabled large area atom interferometry at high data-rates. These features should prove useful for inertial sensing with atom interferometry.

Now that we have introduced precision sensing with LPAI and discussed challenges associated with making these sensors practical, we turn our attention in Chapter 2 to the theoretical background that underpins this work. In Chapter 3, we review the apparatus and methods used to carry out the demonstrations described above. Chapter 4 covers robust atomic timekeeping with Raman ARP (the first thesis contribution) and Chapter 5 details our demonstration of LMT atom interferometry with Raman ARP (the second thesis contribution). In Chapter 6, we offer conclusions and suggest future directions for this work.

Chapter 2

Theory and background

In this chapter, we present the theory of stimulated Raman transitions in the context of interferometry with alkali-metal atoms. Three approaches to interferometer analysis are discussed, and analytic expressions for Ramsey and Mach-Zehnder interferometers are derived. The dynamics of the Raman transition are extended to the time-dependent case of ARP, and a brief qualitative description of laser-cooling and trapping concludes the chapter.

2.1 Stimulated Raman transitions

Atom optics divide, deflect, and mix matter waves to create atomic interference. In this work, atom optics are based on laser pulses that drive stimulated Raman transitions. A Raman process occurs when two photons irradiate a three-level quantum system, and the photon frequency difference matches the quantum resonance frequency. Figure 2-1 depicts a Raman transition between cesium hyperfine ground states $|g\rangle$ and $|e\rangle$. The ground states are coupled to an excited state $|i\rangle$ by two optical photons with frequencies ω_1 and ω_2. The Raman transition occurs if $\omega_1 - \omega_2 \approx \omega_{HFS}$, where ω_{HFS} is the hyperfine splitting frequency between $|g\rangle$ and $|e\rangle$. An offset from this two-photon resonance condition is called a Raman detuning δ. To suppress spontaneous emission (i.e., single-photon excitations), the optical frequencies are detuned from all intermediate $|F'\rangle$ states by a frequency $\sim\Delta$ that is orders of magnitude larger

than the transition linewidth Γ (5.2 MHz in ^{133}Cs). Typical magnitudes of frequency parameters that define the Raman transition are given in Fig. 2-1 (not to scale).

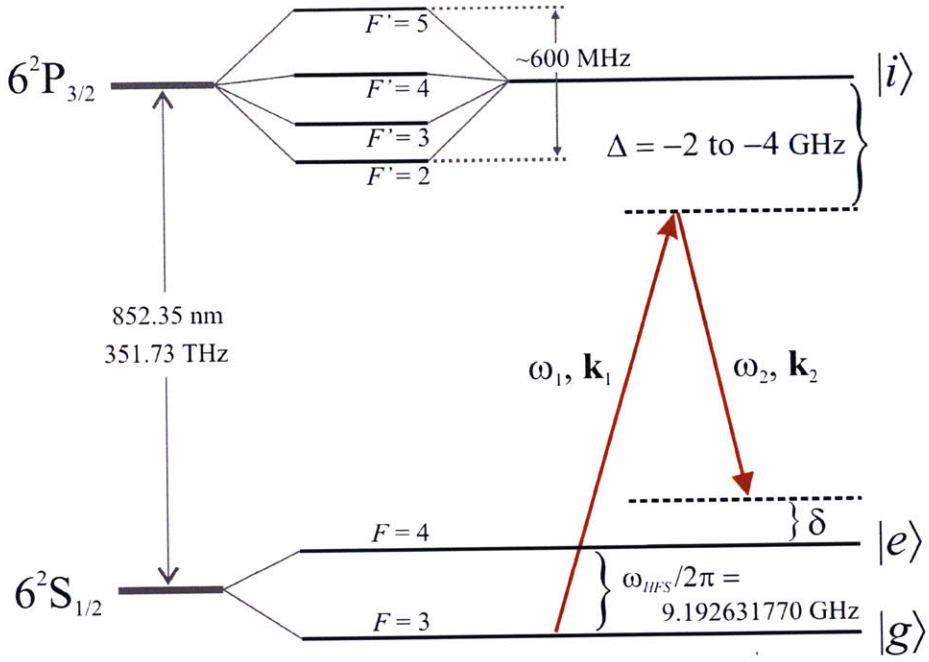

Figure 2-1: Energy level diagram for a stimulated Raman transition on the ^{133}Cs D2 line. The hyperfine ground states $|g\rangle$ and $|e\rangle$ are coupled to an intermediate state $|i\rangle$ by two optical photons with frequencies ω_1 and ω_2. The optical photons are detuned from the single-photon resonance by Δ. A Raman transition between $|g\rangle$ and $|e\rangle$ occurs when $\omega_1 - \omega_2 \approx \omega_{HFS}$.

Atom optics also exist for single-photon transitions at optical frequencies, though they demand state-of-the-art, narrow-linewidth laser sources. Conversely, Raman transitions require only *relative* stability between the optical frequencies. For Raman transitions between hyperfine ground states in alkali-metal atoms, the optical frequencies must differ at the GHz-scale. In this case, stable Raman frequencies can be produced using low-noise RF signals that phase-modulate a single optical frequency or provide a reference for phase-locking two lasers. We use the former approach in our experimental work (see Sec. 3.5.1). Suitable RF signal sources include relatively inexpensive, oven-controlled crystal oscillators that achieve short-term fractional frequency stability at the part-per-trillion level [28].

The Raman frequency components can be spatially oriented to deliver either neg-

ligible or macroscopic[1] momentum transfer to the atoms. As we will soon discuss, timekeeping (accelerometry) applications require negligible (macroscopic) momentum kicks. Fig. 2-2(a) shows the incident Raman frequencies in a co-propagating orientation, which produces essentially no momentum transfer. Absorption of a photon with wave vector $\mathbf{k}_1$ and stimulated emission of a photon with wave vector $\mathbf{k}_2$ changes the internal atomic state while giving the atom a miniscule velocity of 90 nm/s. An alternative orientation with counter-propagating Raman frequencies, shown in Fig. 2-2(b), also uses absorption and stimulated emission to change the internal atomic state. This approach, however, results in an atomic recoil velocity of 7 mm/s due to the addition of two photon recoil momenta. For both Raman frequency orientations, the probability of an atom being detected in a particular ground state oscillates sinusoidally with increasing pulse duration. This behavior, known as Rabi cycling, is shown in Fig. 2-2(c). A quarter-cycle serves as an atom beamsplitter, while a half-cycle results in an atom mirror.

We formalize these ideas by studying the atom-light interactions during a Raman transition. This analysis follows the approach taken in [81] and takes place in a reference frame co-moving with the lower ground state $|g\rangle$. Other treatments can be found in [82, 8, 83]. The two Raman frequency components are modeled as electromagnetic plane waves:

$$\mathbf{E}_1 = \mathbf{E}_{1,0}(t)\cos[\tilde{\phi}_1(t) + \phi_1] \tag{2.1}$$

$$\mathbf{E}_2 = \mathbf{E}_{2,0}(t)\cos[\tilde{\phi}_2(t) + \phi_2]. \tag{2.2}$$

Here, $\mathbf{E}_{1,0}(t)$ is slowly-varying compared to $\tilde{\phi}_{1,2}(t)$. Also, ϕ_1 and ϕ_2 represent arbitrary phase offsets, and the phase terms $\tilde{\phi}_1(t)$ and $\tilde{\phi}_2(t)$ include time-dependent frequencies

[1]The term "macroscopic" refers to a level of momentum transfer that produces large atom displacements relative to the atom wavepacket coherence length.

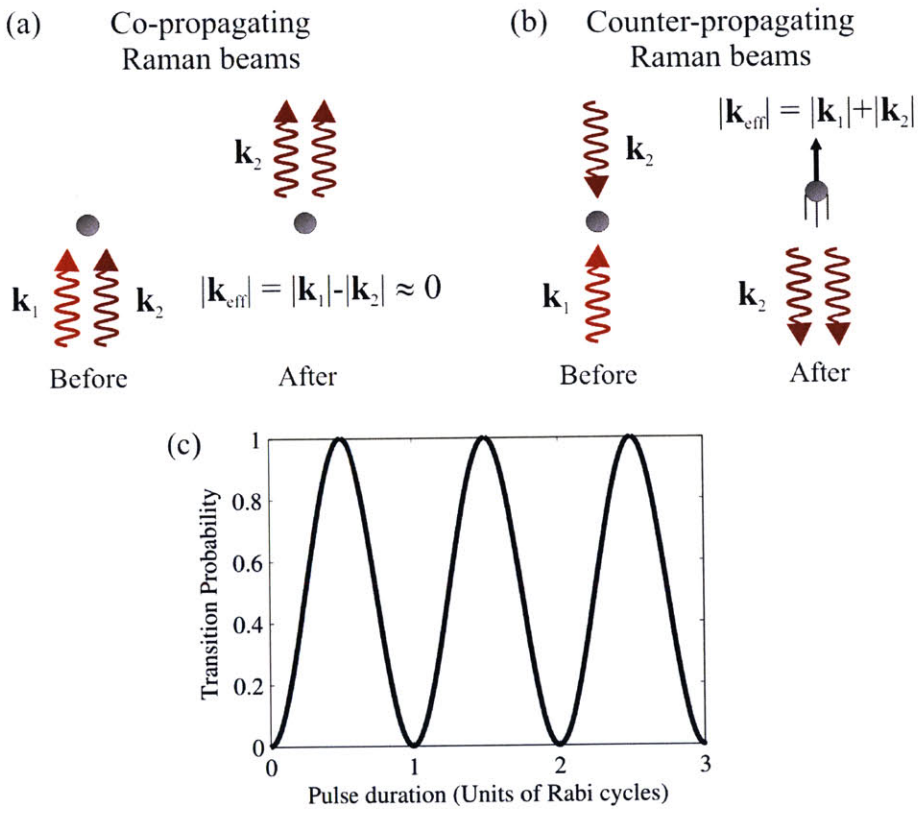

Figure 2-2: Raman pulse momentum transfer and Rabi oscillations. (a) When the Raman laser wave vectors $\mathbf{k}_1$ and $\mathbf{k}_2$ co-propagate, the atom receives a momentum kick $\hbar|\mathbf{k}_{\text{eff}}| = \hbar(|\mathbf{k}_1| - |\mathbf{k}_2|) \approx 0$. (b) With counter-propagation, the atom receives a momentum kick $\hbar|\mathbf{k}_{\text{eff}}| = \hbar(|\mathbf{k}_1| + |\mathbf{k}_2|) \approx 2\hbar|\mathbf{k}_1|$, resulting in a deflection of 7 mm/s for cesium. (c) Application of a resonant Raman pulse produces Rabi oscillations in the probability of an atom to transition from $|g\rangle$ to $|e\rangle$.

and spatial phases. More specifically,

$$\tilde{\phi}_1(t) = \int_0^t [\omega_1(t') - \mathbf{k}_1 \cdot \dot{\mathbf{z}}(t')]dt' \tag{2.3}$$

$$\tilde{\phi}_2(t) = \int_0^t [\omega_2(t') - \mathbf{k}_2 \cdot \dot{\mathbf{z}}(t')]dt' - \mathbf{k}_2 \cdot \frac{\hbar \mathbf{k}_{\text{eff}}}{m} t. \tag{2.4}$$

The integrand is associated with the usual temporal and spatial phase components of a plane wave. Optical frequencies ω_1 and ω_2 are varied in experiments to satisfy the two-photon resonance condition for a freely-falling atom, whose Doppler detuning grows linearly in time. Wave vectors are treated as constants, since their magnitudes change at the part-per-billion level in response to typical variations in ω_1 and ω_2. The $\dot{\mathbf{z}}$-proportional term captures the Doppler shift induced by motion of an atom in state $|g\rangle$. In the expression for $\tilde{\phi}_2(t)$, the term outside the integrand arises from the recoil velocity $\hbar\mathbf{k}_{\text{eff}}/m$ of an atom in state $|e\rangle$, where $\mathbf{k}_{\text{eff}} = \mathbf{k}_1 - \mathbf{k}_2$. This discrepant phase term reflects the assumption that laser fields $\mathbf{E}_1$ and $\mathbf{E}_2$ exclusively and respectively couple the ground states $|g\rangle$ and $|e\rangle$ to the intermediate state $|i\rangle$.

The Raman transition is described by the Schrodinger equation $i\hbar\partial\mathbf{\Psi}/\partial t = [\hat{H}_0 + \hat{V}]\mathbf{\Psi}$. $\hat{H}_0$ is the Hamiltonian operator governing the rest frame internal energies of the atom, and $\mathbf{\Psi}$ is the atomic state. In the electric dipole approximation, the potential energy $\hat{V}$ is dominated by the dipole interactions $q\mathbf{r}\cdot\mathbf{E}_{1,2}(t)$. The Schrodinger equation comprises a system of three, first-order differential equations that correspond to the three coupled atomic energy levels. In matrix form, the equation becomes

$$i\hbar \begin{bmatrix} \dot{\Psi}_e \\ \dot{\Psi}_i \\ \dot{\Psi}_g \end{bmatrix} = \frac{\hbar}{2} \begin{bmatrix} 2\omega_e & \Omega_2(t)e^{i(\tilde{\phi}_2(t)+\phi_2)} & 0 \\ \Omega_2^*(t)e^{-i(\tilde{\phi}_2(t)+\phi_2)} & 2\omega_i & \Omega_1^*(t)e^{-i(\tilde{\phi}_1(t)+\phi_1)} \\ 0 & \Omega_1(t)e^{i(\tilde{\phi}_1(t)+\phi_1)} & 2\omega_g \end{bmatrix} \begin{bmatrix} \Psi_e \\ \Psi_i \\ \Psi_g \end{bmatrix}, \tag{2.5}$$

where $\Psi_{e,i,g}$ are complex amplitudes that determine the superposition of internal atomic states. Diagonal matrix elements come from $\hat{H}_0$, off-diagonal elements come from $\hat{V}$, and we define the complex, resonant, single-photon Rabi rates to be $\Omega_1(t) = \langle i|q\mathbf{r}|g\rangle \cdot \mathbf{E}_{1,0}(t)/\hbar$ and $\Omega_2(t) = \langle i|q\mathbf{r}|e\rangle \cdot \mathbf{E}_{2,0}(t)/\hbar$.

To transform Eq. (2.5) into a more tractable form, we first subtract $\hbar(\omega_e+\omega_g)/2$ from the diagonal matrix elements, which resets the energy origin and has no measurable effect. Second, the laser phase offsets $\phi_{1,2}$ are absorbed into the complex Rabi rates. Third, we define the unitary transformation

$$\begin{bmatrix}\Psi_e\\ \Psi_i\\ \Psi_g\end{bmatrix} = \begin{bmatrix} e^{-\frac{i}{2}(\tilde{\phi}_1(t)-\tilde{\phi}_2(t))} & 0 & 0\\ 0 & e^{-\frac{i}{2}(\tilde{\phi}_1(t)+\tilde{\phi}_2(t))} & 0\\ 0 & 0 & e^{\frac{i}{2}(\tilde{\phi}_1(t)-\tilde{\phi}_2(t))}\end{bmatrix}\begin{bmatrix}b_e\\ b_i\\ b_g\end{bmatrix} \tag{2.6}$$

and substitute this definition into Eq. (2.5). It can be shown that the Schrodinger equation in this frame takes the form

$$\begin{bmatrix}\dot{b}_e\\ \dot{b}_i\\ \dot{b}_g\end{bmatrix} = -\frac{i}{2}\begin{bmatrix}-\delta(t) & \Omega_2(t) & 0\\ \Omega_2^*(t) & -2\Delta & \Omega_1^*(t)\\ 0 & \Omega_1(t) & \delta(t)\end{bmatrix}\begin{bmatrix}b_e\\ b_i\\ b_g\end{bmatrix}, \tag{2.7}$$

where the Raman detuning is

$$\delta(t) = \omega_1(t) - \omega_2(t) - \left[\omega_{HFS} + \frac{\hbar k_{eff}^2}{2m} + \mathbf{k}_{eff}\cdot\dot{\mathbf{z}}\right], \tag{2.8}$$

with $\omega_{HFS} = \omega_e - \omega_g$, and the single-photon detuning is

$$2\Delta = \omega_1(t) + \omega_2(t) - \left[2\omega_i - (\omega_e+\omega_g) - \frac{\hbar k_{eff}^2}{2m} + (\mathbf{k}_1+\mathbf{k}_2)\cdot\dot{\mathbf{z}}\right]. \tag{2.9}$$

Note that $O(k_{1,2}^2)$ terms have been dropped from the definitions of $\delta(t)$ and Δ.

In the limit where $2\Delta^2 \gg |\Omega_2(t)\Omega_1^*(t)|$, the time-derivative of the intermediate state amplitude $\dot{b}_i$ is negligible. Letting $\dot{b}_i = 0$ eliminates b_i from the system of equations and results in an effective two-level system

$$\begin{bmatrix}\dot{b}_e\\ \dot{b}_g\end{bmatrix} = -\frac{i}{2}\begin{bmatrix}\delta_{AC}(t)-\delta(t) & |\Omega_{\text{eff}}(t)|e^{-i\varphi}\\ |\Omega_{\text{eff}}(t)|e^{i\varphi} & -[\delta_{AC}(t)-\delta(t)]\end{bmatrix}\begin{bmatrix}b_e\\ b_g\end{bmatrix}. \tag{2.10}$$

We arrive at this form by defining the two-photon Rabi rate $\Omega_{\text{eff}}(t)$, the differential

AC Stark shift δ_{AC}, and the Raman laser phase φ as follows:

$$\Omega_{\text{eff}}(t) = \frac{\Omega_1(t)\Omega_2^*(t)}{2\Delta} = \frac{|\Omega_1(t)||\Omega_2(t)|}{2\Delta} e^{i\varphi} \tag{2.11}$$

$$\varphi = \phi_1 - \phi_2 \tag{2.12}$$

$$\delta_{AC}(t) = \frac{|\Omega_2(t)|^2 - |\Omega_1(t)|^2}{4\Delta}. \tag{2.13}$$

Additionally, the generalized Rabi rate is

$$\Omega_{\text{gen}} = \sqrt{\Omega_{\text{eff}}^2 + (\delta_{AC} - \delta)^2}. \tag{2.14}$$

For a typical Raman transition, in which laser fields have fixed detunings and amplitudes, the dynamics matrix in Eq. (2.10) is constant and allows for simple integration. An analytic solution is given by the equation $\mathbf{b}(t) = e^{\bar{H}t}\mathbf{b}(0)$, where $\bar{H}$ is the dynamics matrix with constant parameters. Writing out the matrix exponential, we find

$$\begin{bmatrix} b_e(t) \\ b_g(t) \end{bmatrix} = \begin{bmatrix} C^* & -iS^* \\ -iS & C \end{bmatrix} \begin{bmatrix} b_e(0) \\ b_g(0) \end{bmatrix}, \tag{2.15}$$

where

$$C = \cos\left(\frac{\Omega_{\text{gen}}t}{2}\right) + i\frac{\delta_{AC} - \delta}{\Omega_{\text{gen}}} \sin\left(\frac{\Omega_{\text{gen}}t}{2}\right) \tag{2.16}$$

$$S = \frac{\Omega_{\text{eff}}}{\Omega_{\text{gen}}} \sin\left(\frac{\Omega_{\text{gen}}t}{2}\right) e^{i\varphi} \tag{2.17}$$

From Eqs. (2.15), (2.16), and (2.17), we see that a Raman pulse with $\delta_{AC} - \delta = 0$, acting on an atom prepared in $|g\rangle$ or $|e\rangle$, produces sinusoidal (i.e., Rabi) oscillations in the ground state probabilities. A resonant $\pi/2$ Raman pulse, with duration $t_{\pi/2} = (\pi/2)/\Omega_{\text{gen}}$, serves an atom beamsplitter, because the resultant state has an equal probability of being in $|g\rangle$ or $|e\rangle$. To produce a π Raman pulse, which inverts the internal state, the pulse duration is increased to $t_\pi = \pi/\Omega_{\text{gen}}$. We note that this analysis neglects spontaneous emission, which is reasonable since $\Delta \approx 500\Gamma$ in the experiments presented in this thesis. We account for spontaneous emission empirically

in many-pulse sequences when it becomes significant.

2.1.1 Raman transitions on the Bloch sphere

The time-dependent dynamics for a two-level system (see Eq. (2.10)) are conveniently visualized on a three-dimensional space called the Bloch sphere. This spatial representation will prove useful in subsequent discussions of ARP, Raman atom interferometry, and systematic error mechanisms.

We arrive at the Bloch sphere picture by first forming the density matrix for the atomic state

$$\rho = \mathbf{b}(t) \cdot \mathbf{b}^T(t) = \begin{bmatrix} \rho_{ee} & \rho_{eg} \\ \rho_{ge} & \rho_{gg} \end{bmatrix}. \tag{2.18}$$

Diagonal terms in the density matrix represent population in $|e\rangle$ and $|g\rangle$, whereas off-diagonal terms characterize superpositions of these states. This matrix is time-evolved using the equation $i\hbar\dot{\rho} = [H, \rho]$, where $H/(i\hbar)$ is the dynamics matrix from Eq. (2.10). Linear combinations of the density matrix elements define the quantum state on the Bloch sphere via the Bloch vector

$$\hat{\mathbf{p}}(t) = \begin{bmatrix} p_x(t) \\ p_y(t) \\ p_z(t) \end{bmatrix} = \begin{bmatrix} 2\mathrm{Re}\,(\rho_{ge}) \\ 2\mathrm{Im}\,(\rho_{ge}) \\ \rho_{ee} - \rho_{gg} \end{bmatrix}. \tag{2.19}$$

Note that population difference appears in the $p_z(t)$ component, while the $p_x(t)$ and $p_y(t)$ components capture the relative phase between $|g\rangle$ and $|e\rangle$. An atom prepared purely in $|g\rangle$ ($|e\rangle$) is thus aligned with the negative (positive) z axis of the Bloch sphere, while an equal superposition state has no z component at all. The time derivative of $\hat{\mathbf{p}}(t)$ is obtained from the equation of motion for ρ and takes a simple form. For convenience, we define a polar angle θ as

$$\cos\theta = \frac{\delta_{AC} - \delta}{\Omega_{\mathrm{gen}}} \qquad \sin\theta = \frac{|\Omega_{\mathrm{eff}}|}{\Omega_{\mathrm{gen}}}. \tag{2.20}$$

Furthermore, the Raman laser, or "drive field," is characterized by the vector

$$\mathbf{\Omega}_{\text{gen}} = \begin{bmatrix} \Omega_{\text{gen},x} \\ \Omega_{\text{gen},y} \\ \Omega_{\text{gen},z} \end{bmatrix} = \Omega_{\text{gen}} \begin{bmatrix} \sin\theta\cos\varphi \\ \sin\theta\sin\varphi \\ \cos\theta \end{bmatrix}. \tag{2.21}$$

With these definitions, the equation of motion for $\hat{\mathbf{p}}(t)$ on the Bloch sphere becomes

$$\frac{d\hat{\mathbf{p}}(t)}{dt} = \mathbf{\Omega}_{\text{gen}} \times \hat{\mathbf{p}}(t), \tag{2.22}$$

which describes precession of $\hat{\mathbf{p}}(t)$ about $\mathbf{\Omega}_{\text{gen}}$. Equation (2.22) is identical in form to the equation of motion for NMR, in which a nuclear spin is manipulated by a magnetic drive field. *This isomorphism indicates that NMR techniques for robust spin control—such as ARP and composite pulses—could serve as useful atom optics for interferometry.*

As a prelude to subsequent discussion on interferometry and ARP, we visualize simple examples of precession on the Bloch sphere. Figure 2-3(a) shows the action of a resonant Raman $\pi/2$ pulse on an atom initially prepared in state $|e\rangle$. Resonance implies that the drive field is parallel to the x-y plane.[2] Precession induced by the drive field rotates $\hat{\mathbf{p}}(t)$ from the z axis to the x axis during a $\pi/2$ pulse. A π pulse lasts twice as long and continues the precession of $\hat{\mathbf{p}}(t)$ until it reaches the $-z$ axis. For a detuned Raman pulse, the drive field tilts out of the x-y plane ($\theta \neq \pi/2$ rad) and induces precession that no longer traces a great circle, as shown in Fig. 2-3(b). The shift seen in the azimuthal angle of $\hat{\mathbf{p}}(t_{\pi/2})$ can alter the interferometer phase, meaning detuning variations affect the measurement stability.

2.2 Raman atom interferometry

A Raman LPAI can be viewed as a sequence of temporally-separated Raman transitions that serve as atom beamsplitters and mirrors. In Sec. 2.2.1, we describe a

[2] We have chosen $\varphi = \pi/2$ so that $\mathbf{\Omega}_{\text{gen}}$ aligns with the y axis.

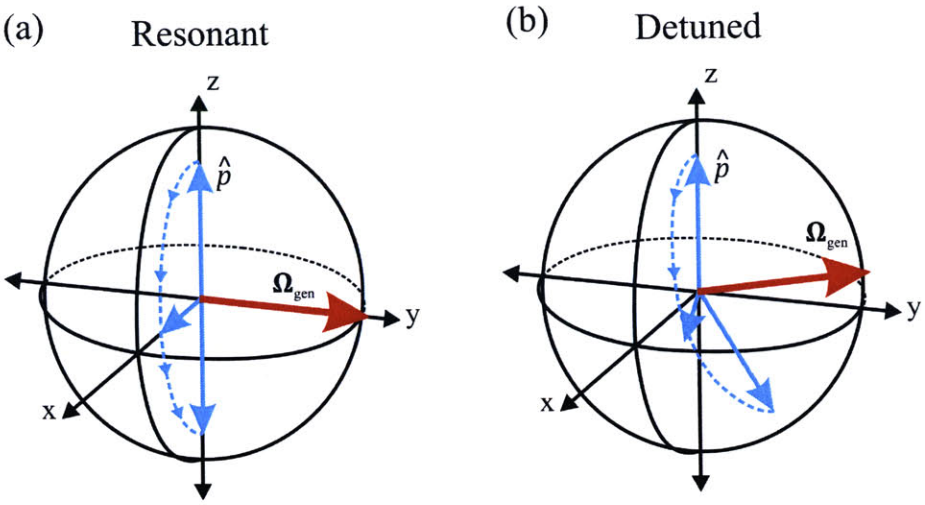

Figure 2-3: Raman transitions visualized on the Bloch sphere. (a) A resonant pulse produces a drive field $\mathbf{\Omega}_{\text{gen}}$ in the equatorial plane, and precession of the Bloch vector follows a great circle. (b) A detuned pulse tilts $\mathbf{\Omega}_{\text{gen}}$ out of the equatorial plane, and precession of $\hat{\mathbf{p}}$ results in systematic phase shifts for a $\pi/2$ pulse.

two-pulse Ramsey sequence on the Bloch sphere. Section 2.2.2 provides a method from [81] for the calculation of interferometer output states for timekeeping and acceleration sensing. Later, in Sec. 2.2.3, we discuss an intuitive picture from [84] of the origins of various phase shifts in Mach-Zehnder interferometers.

2.2.1 Interferometry on the Bloch sphere

Section 2.1.1 described the action of an individual Raman pulse in the Bloch sphere picture. Visualizing an interferometer on the Bloch sphere requires an understanding of Bloch vector evolution during a dwell time. Since the Raman fields are off during this time, $\Omega_{\text{eff}} = 0$ and the drive field becomes $\mathbf{\Omega}_{\text{gen}} = [0, 0, \delta]$. The differential AC Stark shift during this time is $\delta_{AC} = 0$, because the light is off. In experiments, spurious detunings due to magnetic field variation and AC Stark shift from scattered light can systematically affect δ. The alignment of $\mathbf{\Omega}_{\text{gen}}$ with the $\pm z$ axis implies that the Bloch vector rotates about that axis during the dwell time. Solving Eq. (2.22) for this simple case, where $\dot{p}_z(t) = 0$, shows that the rotation rate is δ.

The simplest interferometer to consider is a Ramsey sequence, in which two $\pi/2$

pulses are separated by time T. If $\Omega_{\text{eff}} \gg (\delta_{AC} - \delta)$ during a pulse, the first $\pi/2$ pulse rotates the Bloch vector nearly into the x-y plane, as shown in Fig. 2-4. Evolution

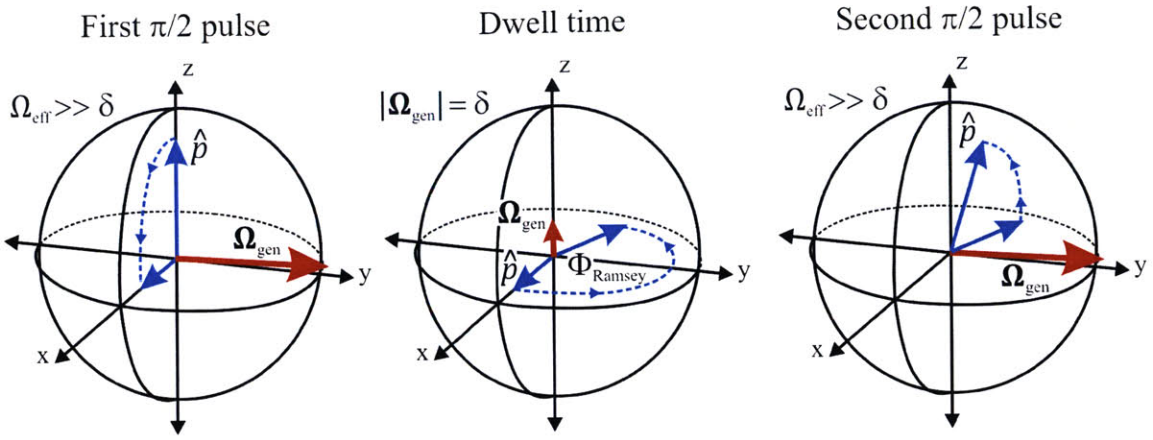

Figure 2-4: Raman Ramsey sequence on the Bloch sphere. Two $\pi/2$ pulses are separated by a time T and carry detunings δ that are small compared to Ω_{eff}. The drive field is non-zero and vertically oriented during the dwell time because of δ. Rotation about the z axis by an angle Φ_{Ramsey} is then measured as a shift in population difference after application of the second $\pi/2$ pulse.

during the dwell time changes the azimuthal angle Φ_{Ramsey} between the Bloch vector and the x axis by δT. The second pulse then torques $\mathbf{p}(t)$ such that Φ_{Ramsey} is mapped into population difference p_z. Standard state readout methods, such as laser induced fluorescence, measure the population difference after the interferometer and thereby detect δ. When the dwell time is constant, shifts in detuning alter the angle of precession during T, thereby creating a sinusoidal variation in transition probability—an interferogram—shown in Fig. 2-5. Near resonance, the transition probability P is related to Φ_{Ramsey} by the equation

$$P = \frac{1}{2} + \frac{A}{2} \cos \Phi_{\text{Ramsey}} + B, \tag{2.23}$$

where A is the peak-to-trough amplitude, or contrast, and B is the background. Sensitive detuning measurements can be made by operating the Ramsey interferometer near the middle of a sinusoidal fringe, where the change in population due to detuning is largest.

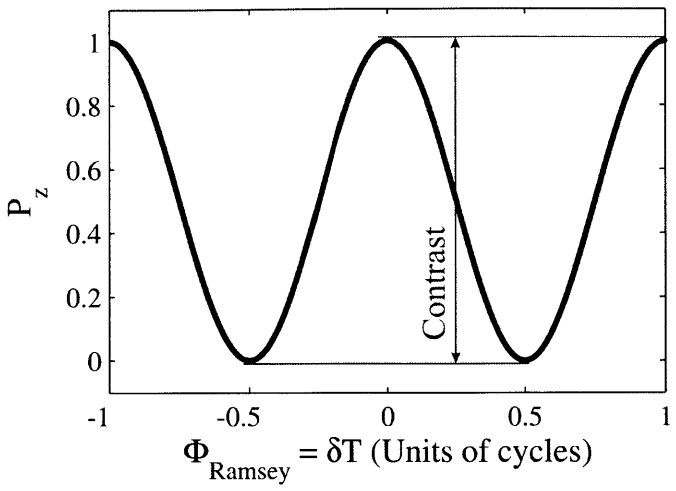

Figure 2-5: Interferogram for a Raman atom interferometer. Phase shifts modulate the population sinusoidally. Contrast is a measure of the peak-to-trough amplitude of an interference fringe. Sensitive phase measurements are made by operating the interferometer near the middle of a fringe, where the slope is steepest.

In a clock, Ramsey measurements of δ serves as an error signal for a feedback loop that corrects the crystal oscillator sourcing the Raman RF difference frequency. The frequency from the disciplined crystal then provides a timing reference with excellent long-term stability. Alternatively, a Ramsey sequence can be configured to sense changes in environmental magnetic fields due to the Zeeman effect.

2.2.2 Scattering amplitude model

In Sec. 2.1, we found an analytic expression for the action of a Raman beamsplitter or mirror (i.e., $\pi/2$ or π pulses) with constant frequency and intensity parameters. That expression (see Eq. (2.15)) can be rewritten in a more suggestive form:

$$\mathbf{b}(t) = \begin{cases} C^*(t)|e\rangle - iS(t)|g\rangle, & \text{for } \mathbf{b}(0) = |e\rangle \\ -iS^*(t)|e\rangle + C(t)|g\rangle, & \text{for } \mathbf{b}(0) = |g\rangle \end{cases}. \tag{2.24}$$

The explicit time dependence indicated in the scattering amplitude captures the difference between a Raman $\pi/2$ and π pulse. The scattering diagram in Fig. 2-6 represents Eq. (2.24) pictorially. Horizontal arrows represent $|g\rangle$ trajectories while tilted

lines represent $|e\rangle$ trajectories. The vertical line marks when a Raman transition occurs, and the node represents the point where scattering (S) and continuing (C) wavepackets diffract. A subsequent Raman pulse would spawn two new pairs of S and C wavepackets, with each pair emanating, for example, from the S_1^* and C_1 wavepackets seen on the left side of Fig. 2-6.

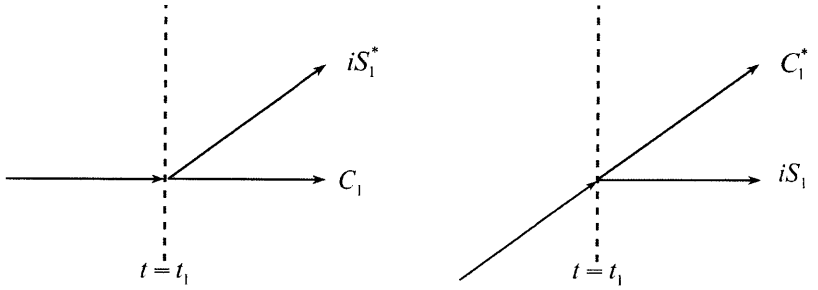

Figure 2-6: Scattering diagram for a Raman pulse (Credit: [81]). Scattered (deflected) wavepackets carry an amplitude S, while continuing (undeflected) wavepackets have an amplitude C.

As detailed in [81], these amplitudes must be related to the atomic state $\mathbf{\Psi}$ in the non-rotating frame using the unitary transformation in Eq. (2.6). More specifically, a model of $\mathbf{\Psi}$ undergoing a Raman transition during time t_p to $t_p + \tau_p$ would first transform $\mathbf{\Psi}(t_p)$ into state $\mathbf{b}(t_p)$ in the rotating frame, then apply the appropriate scattering amplitudes, and finally transform back to the state $\mathbf{\Psi}(t_p + \tau_p)$ in the non-rotating frame.

The scattering diagram for an interferometer must also account for the effects of a dwell time T. Since the laser fields are off during this time, the off-diagonal terms in Eq. (2.5) are zero and only the internal energies of the atom remain. Solving this uncoupled system of equations shows that during the dwell time, the amplitude for state $|e\rangle$ acquires a phase factor $e^{i\omega_{HFS}T/2}$, while the amplitude for state $|g\rangle$ acquires the complex conjugate of this phase factor. In an interferometer model, these dwell-dependent phase factors are applied after a transformation out of the rotating frame (from the previous Raman pulse) and before a transformation into the rotating frame (for the next Raman pulse). Combining the transformation and dwell-dependent phase factors reveals that the phase evolution between the j^{th} and $j + 1^{\text{th}}$

interferometer pulses is $e^{\frac{i}{2}\Phi_{j\to j+1}}$ for $|e\rangle$ and $e^{-\frac{i}{2}\Phi_{j\to j+1}}$ for $|g\rangle$, where

$$\Phi_{j\to j+1} \equiv \int_0^{t_{j+1}} \delta_{j+1}(t)dt - \int_0^{t_j+\tau_j} \delta_j(t)dt. \tag{2.25}$$

Examples of scattering diagrams for two-pulse Ramsey sequences and three-pulse Mach-Zehnder sequences are shown in Fig. 2-7. The column of amplitudes immediately following $t = t_2$ corresponds to the Ramsey sequence output; the final column corresponds to the Mach-Zehnder sequence. The output populations of an interferometer are determined by calculating the squared norm of the sum of amplitudes associated with $|e\rangle$ and then repeating this calculation for amplitudes associated with $|g\rangle$. For the Ramsey sequence, the output populations are

$$|\Psi_{e,\text{Ramsey}}|^2 = |C_1|^2|S_2|^2 + |S_1|^2|C_2|^2 + 2\text{Re}\left(C_1^* S_1^* C_2^* S_2 e^{i\Phi_{1\to 2}}\right) \tag{2.26}$$

$$|\Psi_{g,\text{Ramsey}}|^2 = |C_1|^2|C_2|^2 + |S_1|^2|S_2|^2 - 2\text{Re}\left(C_1^* S_1^* C_2^* S_2 e^{i\Phi_{1\to 2}}\right), \tag{2.27}$$

whereas for the Mach-Zehnder interferometer we have

$$\begin{aligned}
|\Psi_{e,\text{MZ}}|^2 =& |S_1|^2|S_2|^2|S_3|^2 + |C_1|^2|S_2|^2|C_3|^2 + |S_1|^2|C_2|^2|C_3|^2 \\
&+ |C_1|^2|C_2|^2|S_3|^2 - \left[C_1 S_1 (S_2^*)^2 C_3^* S_3 e^{i\Phi_{int}} + c.c.\right] \\
&+ C_1^* S_1^* (C_2^*)^2 C_3^* S_3 e^{i\Phi_{loss}} + c.c. \\
&+ C_1 S_1 C_2 S_2^* \left(|C_3|^2 - |S_3|^2\right) e^{\frac{i}{2}(\Phi_{int}-\Phi_{loss})} + c.c. \\
&+ C_2^* S_2^* C_3^* S_3 \left(|C_1|^2 - |S_1|^2\right) e^{\frac{i}{2}(\Phi_{int}+\Phi_{loss})} + c.c. \qquad (2.28) \\
|\Psi_{g,\text{MZ}}|^2 =& |C_1|^2|S_2|^2|S_3|^2 + |S_1|^2|S_2|^2|C_3|^2 + |S_1|^2|C_2|^2|S_3|^2 \\
&+ |C_1|^2|C_2|^2|C_3|^2 + C_1 S_1 (S_2^*)^2 C_3^* S_3 e^{i\Phi_{int}} + c.c. \\
&- \left[C_1^* S_1^* (C_2^*)^2 C_3^* S_3 e^{i\Phi_{loss}} + c.c.\right] \\
&- \left[C_1 S_1 C_2 S_2^* \left(|C_3|^2 - |S_3|^2\right) e^{\frac{i}{2}(\Phi_{int}-\Phi_{loss})} + c.c.\right] \\
&- \left[C_2^* S_2^* C_3^* S_3 \left(|C_1|^2 - |S_1|^2\right) e^{\frac{i}{2}(\Phi_{int}+\Phi_{loss})} + c.c.\right], \qquad (2.29)
\end{aligned}$$

with $\Phi_{int} \equiv \Phi_{2\to 3} - \Phi_{1\to 2}$ and $\Phi_{loss} \equiv \Phi_{2\to 3} + \Phi_{1\to 2}$.

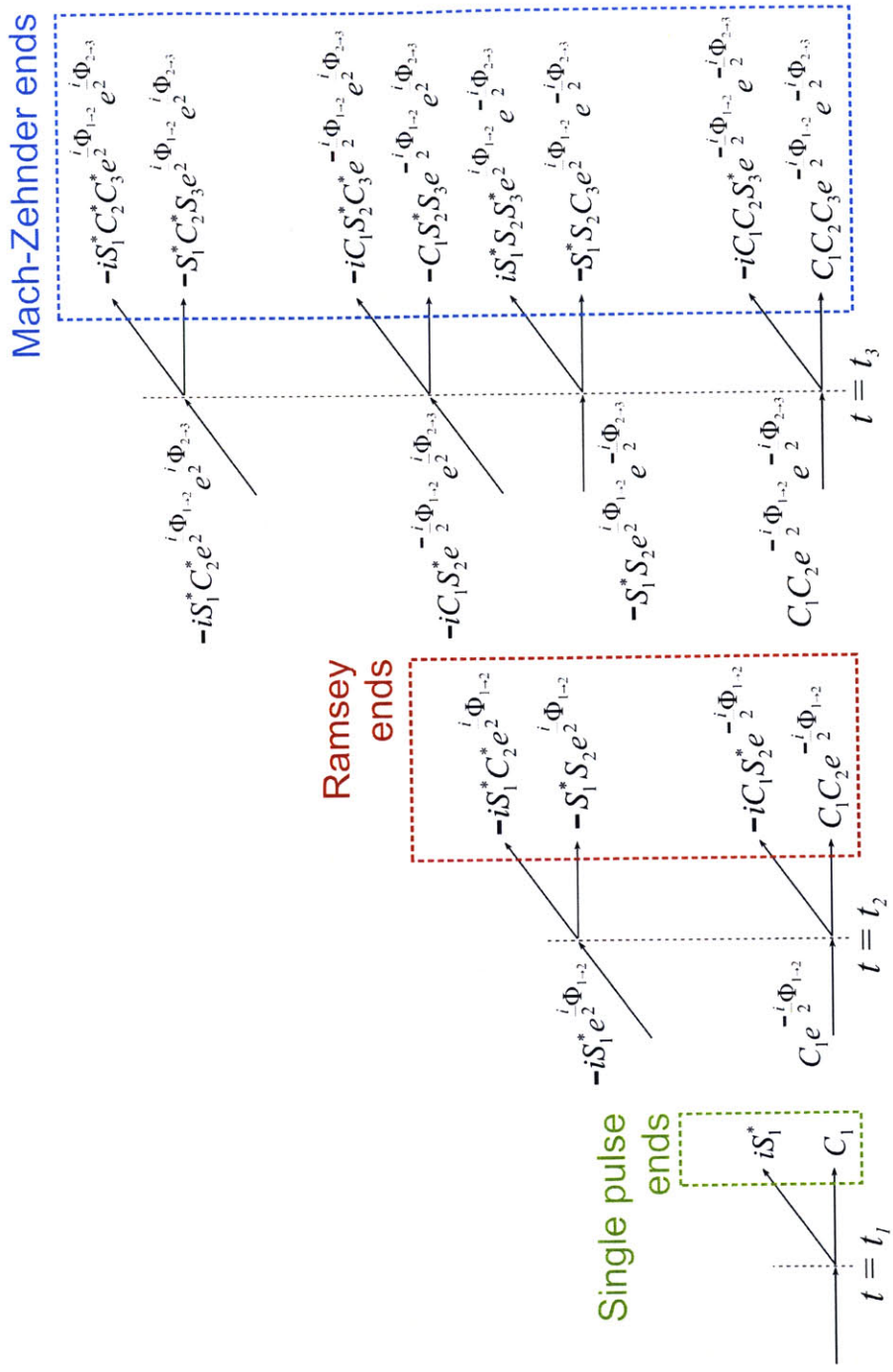

Figure 2-7: Scattering diagram for Raman atom interferometers [81]. Boxed amplitudes are produced by single pulse (green), Ramsey (red), and Mach-Zehnder (blue) sequences. In each case, the amplitudes of a particular internal state are coherently summed and then normed to determine the population difference of the output. The diagram assumes either co- or counter-propagating Raman frequencies were used for a particular sequence. Wavepacket deflections in a Ramsey sequence with co-propagating Raman frequencies are significantly smaller than the deflections produced by counter-propagating frequencies in a typical Mach-Zehnder interferometer.

To further evaluate these general results, we note that each measurement is acquired from an ensemble of atoms with an associated velocity distribution. The Doppler shift $\mathbf{k}_{\text{eff}} \cdot \dot{\mathbf{z}}(t)$ clearly incorporates this distribution and affects interferometer phase factors like Φ_{loss}, which depend on the Doppler shift. Depending on the magnitude of $\mathbf{k}_{\text{eff}}$ and the average velocity of the atoms, these phase factors can be suppressed to zero after averaging over the velocity distribution. Co-propagating Raman frequencies result in $k_{\text{eff, Co}} = 1.93 \times 10^2$ rad/m, whereas counter-propagation produces $k_{\text{eff, Count}} = 1.47 \times 10^7$ rad/m. Furthermore, a typical ensemble of laser-cooled ^{133}Cs atoms has an RMS velocity of $\sim$1 cm/s. The resulting uncertainty in interferometer phase over a 10-ms dwell time is then $k_{\text{eff}} \left[\frac{\text{rad}}{\text{m}}\right] \times 1 \left[\frac{\text{cm}}{\text{s}}\right] \times 10\,[\text{ms}]$, which is >1000 rad for $k_{\text{eff, Count}}$ and about 10 mrad for $k_{\text{eff, Co}}$. Therefore, when using counter-propagating (i.e., Doppler sensitive) Raman frequencies, all phase factors other than $e^{i\Phi_{\text{int}}}$ average to zero. The survival of Φ_{int} results from a spin echo: a cancellation of the fixed Doppler shift of each atom when differencing $\Phi_{2\to3}$ and $\Phi_{1\to2}$.[3] Co-propagating (i.e., Doppler insensitive) frequencies, on the other hand, allow for contributions from all phase terms.

A Ramsey sequence with Doppler insensitive frequencies can detect the detuning information found in $\Phi_{1\to2}$. If the sequence uses two $\pi/2$ pulses with the same field intensity and small detuning δ, the Ramsey phase sensitivity is

$$\Phi_{\text{Ramsey}} = \Phi_{1\to2} = \delta T, \tag{2.30}$$

where we have neglected higher order terms. In a Mach-Zehnder interferometer, Doppler sensitive Raman transitions eliminate Φ_{loss} terms in Eqs. (2.28) and (2.29). The phase response to acceleration, neglecting higher order terms, is given by

$$\Phi_{\text{MZ}} = \Phi_{int} = -\mathbf{k}_{\text{eff}} \cdot \mathbf{a}T^2. \tag{2.31}$$

Since the phase response to acceleration is proportional to $\mathbf{k}_{\text{eff}}$, the interferometer

[3]This spin echo is only useful when the two dwell times of the Mach-Zehnder interferometer are matched to within a few microseconds.

sensitivity is $\sim 10^5$ larger with $k_{\text{eff, Count}}$ as compared to $k_{\text{eff, Co}}$.

2.2.3 Path integral treatment for accelerometry

For an intuitive understanding of the inertial sensitivity of a Mach-Zehnder interferometer, consider a falling object. The acceleration $-a$ of the object is measured by tracking its position z_j at three points in time and using the kinematic equation

$$-a = \frac{z_1 - 2z_2 + z_3}{T^2}, \tag{2.32}$$

where we have assumed the position measurements were temporally separated by time T. To relate this equation to the interferometer, recall that the phase of the Raman laser beam, $\tilde{\varphi}_j = k_{\text{eff}} z_j + (\omega_1 - \omega_2)t + \varphi$, contains a spatial dependence proportional to z_j. Note that, unlike in Sec. 2.1, this laser phase is defined in the laboratory frame. As shown in Fig. 2-8(a), the spatial laser phase can act like a finely-ticked ruler for displacement measurements, since the effective Raman wavelength is 426 nm. Rewriting Eq. (2.32) in terms of $\tilde{\varphi}_j$, we find

$$a = \frac{\tilde{\varphi}_1 - 2\tilde{\varphi}_2 + \tilde{\varphi}_3}{k_{\text{eff}} T^2}, \tag{2.33}$$

where $\tilde{\varphi}_1 - 2\tilde{\varphi}_2 + \tilde{\varphi}_3$ is equivalent to Φ_{MZ} from Eq. (2.31). Phase factors carrying laser phases $\tilde{\varphi}_j$, defined with respect to the atom wavepacket center of mass, premultiply the wavefunction when a Raman transition occurs. Interferometry is used to extract this phase information. To create the interferometer shown in Fig. 2-8(b), a $\pi/2$ beamsplitter pulse divides the atom wavepacket in two, and the upper arm acquires $\hbar k_{\text{eff}}$ worth of momentum. Since the Raman frequencies are counter-propagating, the wavepacket separation exceeds its spatial extent over the millisecond timescales of the interferometer. A subsequent π pulse deflects the wavepackets back toward each other, and a final $\pi/2$ pulse combines the wavepackets to create interference. The imprinted Raman laser phases are indicated in Fig. 2-8(b). Note that laser phase is imprinted with a state-dependent sign and only when an internal state transition

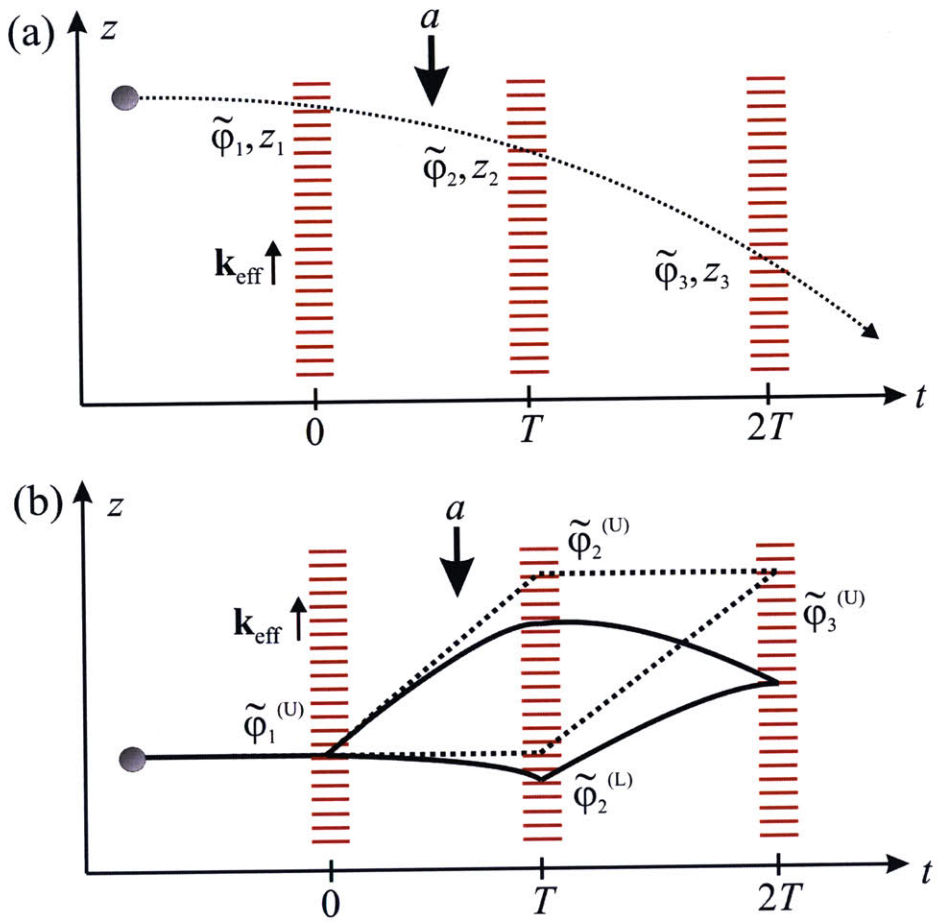

Figure 2-8: Classical view of an atom interferometric accelerometer. (a) A falling atom samples the phase of an incident laser beam at three locations. The position-dependent phase acts like a finely-ticked ruler for displacement measurements. The phase information must be retrieved through atom interferometry. (b) A Mach-Zehnder atom interferometer, with (solid lines) and without (dotted lines) acceleration, senses differential phase shifts between the two interferometer arms. This phase is proportional to acceleration and modulates the transition probability at the interferometer output ports.

occurs. Following these two rules, and assuming the Raman frequencies are constant, we sum the laser phases along both interferometer arms and then difference the sums to obtain the phase sensitivity shown in Eq. (2.31).

Calculation of interferometer phase shifts using classical wavepacket trajectories is justified by the path integral formulation of quantum mechanics [84]. In this formulation, a quantum state originating at point x_A evolves into a state at point x_B according to the equation

$$\psi_b = \int dx_a K_{ab} \psi_a, \tag{2.34}$$

where

$$K_{ab} \propto \sum_{\Gamma} e^{iS^{\Gamma}_{\mathrm{Act}}/\hbar} \tag{2.35}$$

is the state propagator defined in terms of the action

$$S^{\Gamma}_{\mathrm{Act}} = \int_{t_A}^{t_B} L\left[x(t), \dot{x}(t)\right] dt \tag{2.36}$$

over a path Γ, and with Lagrangian $L\left[x(t), \dot{x}(t)\right]$. The definition of K_{ab} implies that a wavepacket is equally likely to traverse all possible paths connecting points x_A and x_B. However, paths far away from the classical trajectory result in $S^{\Gamma}_{\mathrm{Act}} \gg \hbar$, which causes the phase factor $e^{iS^{\Gamma}_{\mathrm{Act}}/\hbar}$ to oscillate rapidly. Neighboring paths thereby destructively interfere, and significant amplitudes only come from the classical trajectory [85].

The path integral formulation also reveals that phase shifts arise during free propagation of the quantum state. The quadratic Lagrangian for a classical trajectory in a gravitational field, $L = mv^2/2 - mgx$, can be shown to contribute path-dependent phase factors $e^{iS^{\Gamma}\mathrm{Act}/\hbar}$ to the upper and lower interferometer arms when the atoms are modeled as plane wave states [84]. These phases cancel in a uniform gravitational field. When gravity gradients break this equality, the path integral analysis offers a useful method for calculation of expected phase shifts. In this work, the <600-μm separations between interferometer arms result in negligible phase shifts due to gravity gradients.

Finally, phase shifts also arise when the classical trajectories do not perfectly

overlap for the final beamsplitter pulse. Rotations and gravity gradients are common sources of non-overlap and are not a primary concern in this work. Nevertheless, a separation of $\mathbf{z}_{\text{sep}}$ between the classical paths during the final pulse introduces a shift in relative phase between atomic plane waves of $\Phi_{\text{sep}} = \mathbf{k}_{dB} \cdot \mathbf{z}_{\text{sep}}$, where $\mathbf{k}_{dB}$ is the wave vector corresponding to the de Broglie wavelength λ_{dB}. As in an optical interferometer, Φ_{sep} is determined by the ratio of the path length difference to λ_{dB}.

2.3 Raman adiabatic rapid passage

Our discussion of atom optics and interferometry has focused on Raman transitions with constant detuning, phase, and Rabi rate, such as π and $\pi/2$ pulses. These atom optics, however, are susceptible to detuning and field intensity errors. In Fig. 2-3, for example, the detuned $\pi/2$ pulse adds a systematic shift to the azimuthal angle between the Bloch vector and the x axis that ultimately affects the Ramsey phase. Additionally, optical intensity variation causes π and $\pi/2$ Raman pulses to over or undershoot the desired pulse area, which reduces contrast. Analogous problems in NMR are mitigated using frequency-swept ARP, whose effect on a two-level system can be visualized on the Bloch sphere in Fig. 2-9. When the drive field is applied, $\hat{\mathbf{p}}$ precesses about $\mathbf{\Omega}_{\text{gen}}$ at the generalized Rabi frequency Ω_{gen}. If the drive field is then rotated without violating the adiabatic condition

$$\dot{\theta}(t) \ll \Omega_{\text{gen}}(t), \tag{2.37}$$

$\hat{\mathbf{p}}$ encircles $\mathbf{\Omega}_{\text{gen}}$ before θ can change appreciably. In effect, rapid precession causes $\hat{\mathbf{p}}$ to adiabatically follow $\mathbf{\Omega}_{\text{gen}}$. The projection of $\hat{\mathbf{p}}$ onto the drive field, which we define as $\mathbf{p}_{\parallel}$, can thus be dragged anywhere on the sphere. For an atom prepared in $|g\rangle$ or $|e\rangle$, the Bloch vector and drive field are initially parallel in the limit of infinite detuning. The transfer efficiency in the adiabatic limit is optimal in this case. As shown in Fig. 2-10(a), finite detunings with $\delta \gg \Omega_{\text{eff}}$ create a small angle $\Omega_{\text{eff}}/\delta$ between the Bloch vector and drive field, indicating that a combination of large

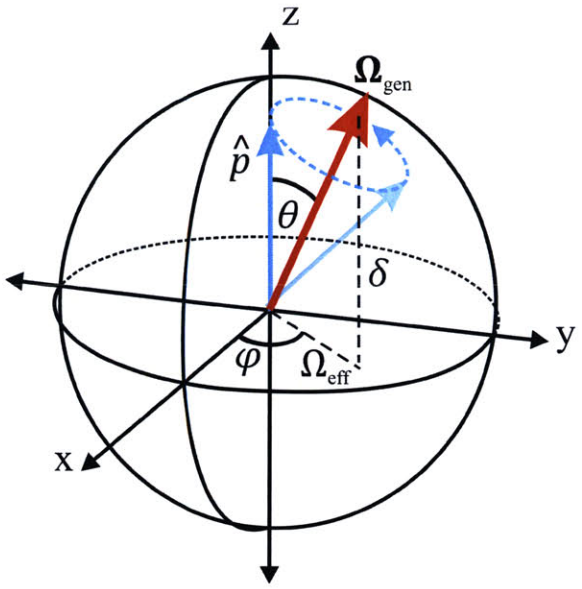

Figure 2-9: Bloch sphere depiction of Raman adiabatic rapid passage. The Bloch vector $\hat{\mathbf{p}}$ adiabatically follows $\mathbf{\Omega}_{gen}$ when $\dot{\theta} \ll \Omega_{gen}$. Here, Ω_{gen} sets the rate of precession of $\hat{\mathbf{p}}$ about $\mathbf{\Omega}_{gen}$. The projection of $\hat{\mathbf{p}}$ onto the drive field can be dragged anywhere on the sphere.

detuning and small Rabi rate gives near ideal alignment. The initial detuning should also significantly exceed the detuning inhomogeneity of the atom ensemble so that the drive field is simultaneously aligned with the Bloch vectors representing the initial states of each atom. In Fig. 2-10(a), an ARP π pulse begins with a large negative detuning, sweeps through resonance, and ends with a large positive detuning. The same sweep is stopped on resonance to achieve an ARP beamsplitter ($\pi/2$) pulse. When the ARP beamsplitter acts on a superposition state, as is the case during the second pulse of a Ramsey sequence, the pulse begins on resonance and sweeps to a large detuning, effectively carrying out the second half of a π sweep. The initial angle between the Bloch vector and the drive field, namely the Ramsey phase, is fixed in the adiabtic limit and converted into a detectable population difference. Experimentally, we control θ by sweeping δ over a frequency range that is large with respect to Ω_{eff}, while also modulating the optical intensity.

ARP is generally advantageous when inversion is performed with a spatially inhomogeneous drive field [59, 60]. Since the Rabi rate in this case is position dependent,

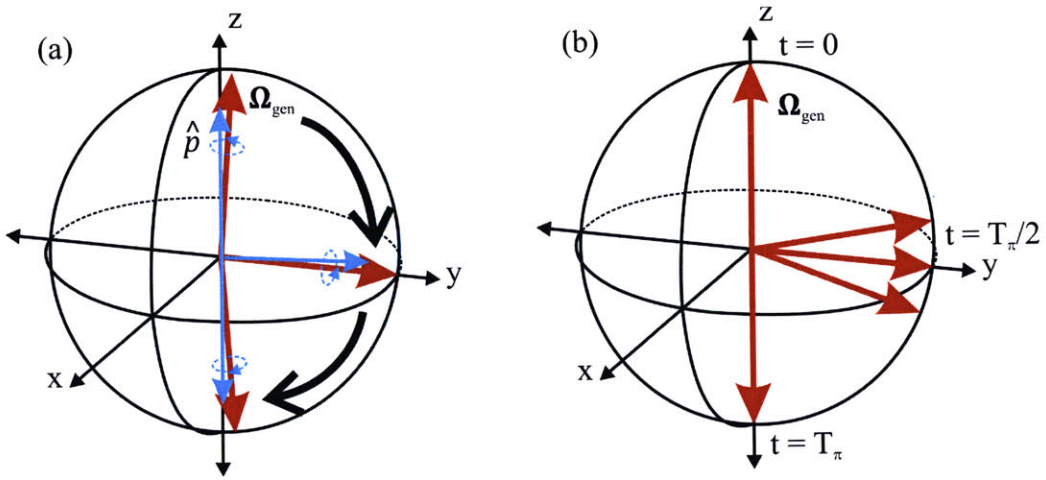

Figure 2-10: Raman adiabatic rapid passage π and $\pi/2$ pulses. (a) The far-detuned drive is nearly parallel with the Bloch vector of an atom initially in $|e\rangle$. In the adiabatic limit, precession allows for the Bloch vector be dragged to the equatorial plane for a beamsplitter pulse, or to the opposite pole for a mirror pulse. (b) When the detuning inhomogeneity of the sample is $\sim\Omega_{\text{eff}}$, yet small compared to the maximum ARP detuning, the behavior at the beginning and end of the sweep is the same as in (a). However, when $t = T_\pi/2$ near the middle of the sweep, the drive fields for atoms with different detunings have varying polar angles that reduce the transfer efficiency of ARP beamsplitters.

precise control of spin precession cannot be achieved for the entire ensemble of atoms. With an ARP sweep, however, transfer efficiency in the adiabatic limit ultimately depends on the projection of $\hat{\mathbf{p}}$ onto $\mathbf{\Omega}_{\text{gen}}$, namely $\mathbf{p}_{\|}$, which is independent of precession. As long as the adiabatic condition is satisfied over all regions of the drive field sampled by the atoms, an ARP π pulse will invert population with high fidelity. Many ARP sweeps also tolerate larger detuning offsets δ_0 than ordinary π pulses. The detuning offset effectively shifts the center frequency of an ARP sweep away from resonance and affects how well the adiabatic condition is satisfied at different times. If the initial ARP detuning is large with respect to the detuning offset, inversion for *multiple* atoms in the adiabatic limit would behave as shown in Fig. 2-10(b) on the Bloch sphere. The Bloch vectors are assumed to be parallel to the drive field for simplicity. The drive field initially aligns with the z axis, because it is far detuned from all the atomic resonances. At $t = T_\pi/2$, when the ARP sweep should be resonant, the different atomic detunings cause the drive field for a particular atom to tilt out of the equatorial plane with a polar angle $\tan\theta = -\Omega_{\text{eff}}/\delta_0$. If adiabaticity is maintained, an ARP π pulse continues to rotate the Bloch vector to the $-z$ axis regardless of δ_0. However, the transfer efficiency of an ARP $\pi/2$ beamsplitter is sensitive to detuning offsets, since the pulse ends when the Bloch vectors are spread about the y axis. Phase shifts due to ARP atom optics are also important for interferometry applications and will be discussed in Sec. 2.3.1.

In the standard approach to ARP, the Raman detuning is linearly chirped through resonance. For a constant chirp rate r, constant Ω_{eff}, and detuning offset δ_0, the adiabatic condition from Eq. (2.37) takes the form $(\Omega_{\text{eff}}/r)^2 \left[(|r|/\Omega_{\text{eff}}^2)^{2/3} - 1\right] \ll (t + \delta_0/r)^2$, if we assume the frequency sweep is centered at $t = 0$. The condition is satisfied for $r < \Omega_{\text{eff}} \approx 100$ kHz, which implies prohibitively long pulses since the sweep must cover MHz-scale detunings. This wide sweep range is particularly important for accelerometry applications, in which Doppler shifts in the atom ensemble create a detuning inhomogeneity that spans over ± 100 kHz. For this work, we instead chose nonlinear frequency sweeps that rapidly changed the polar angle θ at the beginning and end of the adiabatic passage, when the adiabatic condition was well-satisfied

because of large δ. A short sweep helps minimize dephasing due to spontaneous emission and quickly covers a broad frequency range. The primary frequency sweep of interest in this work is described by the equation

$$\delta(t) = \Omega_{arp} \tan\left[\alpha\left(\frac{2t}{T_\pi} - 1\right)\right], t \in \{0, T_\pi\} \tag{2.38}$$

where T_π sets the total sweep duration, Ω_{arp} changes the sweep rate without perturbing its duration or range, and $\alpha = \arctan(\delta_{max}/\Omega_{arp})$, where δ_{max} is the maximum detuning. This frequency sweep is coupled with an intensity modulation $I(t)$ of the form

$$I(t) = I_0 \tanh\left[\beta\left(1 - \left|\frac{2t}{T_\pi} - 1\right|\right)\right], \tag{2.39}$$

where I_0 is the maximum intensity, and the unitless parameter β (typically 7.5) determines the extent to which the modulation deviates from a square shape. These frequency and intensity modulations are plotted in Fig. 2-11. Since $I(0) = I(T_\pi) = 0$, the drive field at the beginning and end of the sweep is essentially parallel with the z-axis of the Bloch sphere. Variants of this so-called Tan/Tanh pulse have been proposed and implemented in [65, 67, 86]. To quantify the adiabaticity of a particular

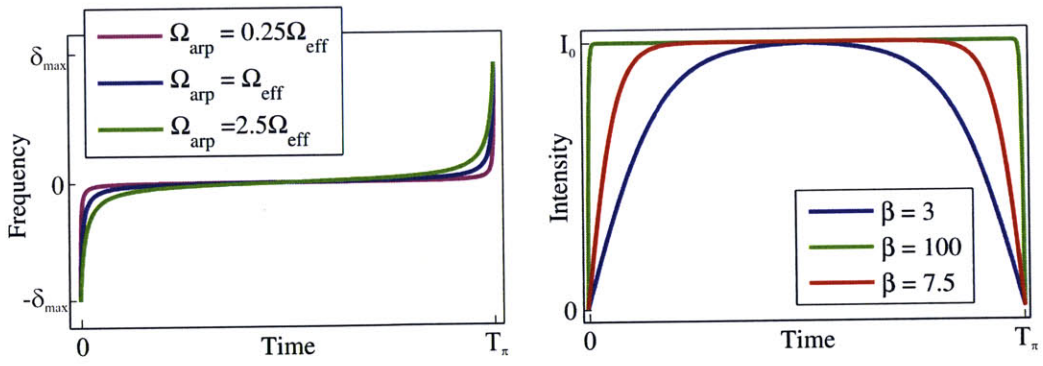

Figure 2-11: Tan/Tanh ARP frequency sweep and intensity modulation. The rapid frequency changes (left) near the beginning and end of the pulse satisfy the time-dependent adiabatic condition and cover a wide frequency span in a short time. Short pulse durations are important for minimizing spontaneous emission. Low optical intensities (right) coincide with large detunings so that the drive field is nearly parallel with the Bloch vector at the beginning of the pulse.

sweep, we define the unitless parameter $Q(t) = \Omega_{gen}/|\dot{\theta}|$. Near resonance, and when

$\delta_{max} \gg \Omega_{eff} = \Omega_{arp}$, we find that $Q = n$ when $T_\pi = nt_\pi$, where t_π is the duration of a Raman π pulse. Our experimental demonstrations, along with previous work [65], have shown that $Q \geq 5$ provides sufficient adiabaticity for robust population transfer.

The evolution of a two-level system during a Raman ARP sweep does not have a general analytic solution, because the Hamiltonian in Eq. (2.10) is time-dependent. Analogues to the resonant Raman scattering amplitudes C and S (see Eqs. (2.16) and (2.17)) must therefore be calculated numerically for ARP. Solutions can be obtained using the Schrodinger formalism for an effective two-level system, as well as the Bloch sphere equation of motion from Eq. (2.22).

2.3.1 Dressed state picture of Raman ARP

In the adiabatic limit, it is useful to consider the action of a Raman ARP pulse in the dressed state picture, which is related to the "bare" state picture of Eq. (2.10) by a unitary transformation. The dressed basis states are parallel and antiparallel with respect to the drive field, while the "bare" basis states are $|e\rangle$ and $|g\rangle$. The bare state $\mathbf{b}(t)$ is represented in the dressed basis as

$$\begin{bmatrix} d_+ \\ d_- \end{bmatrix} = \begin{bmatrix} \cos\frac{\theta(t)}{2} & \sin\frac{\theta(t)}{2}e^{-i\varphi} \\ -\sin\frac{\theta(t)}{2}e^{i\varphi} & \cos\frac{\theta(t)}{2} \end{bmatrix} \begin{bmatrix} b_e \\ b_g \end{bmatrix}, \tag{2.40}$$

where θ is given by Eq. 2.20. The equation of motion for the two-level system from Eq. (2.10) then takes the form

$$\begin{bmatrix} \dot{d}_+ \\ \dot{d}_- \end{bmatrix} = -\frac{i}{2} \begin{bmatrix} \Omega_{\text{gen}}(t) & -i\dot{\theta}(t)e^{-i\varphi} \\ i\dot{\theta}(t)e^{i\varphi} & -\Omega_{\text{gen}}(t) \end{bmatrix} \begin{bmatrix} d_+ \\ d_- \end{bmatrix}. \tag{2.41}$$

In the adiabatic limit, $\dot{\theta}(t) \to 0$ and the dressed state amplitudes evolve according to $d_\pm(t) = e^{\mp i\gamma} d_\pm(0)$, where $\gamma = \int_0^t dt' \Omega_{gen}(t')/2$ is a dynamic phase [63]. To understand an ARP inversion in this picture, recall that the drive field is parallel to the $\pm z$ axis at the beginning and end of an inversion. Since $|e\rangle$ and $|g\rangle$ at these times are equivalent to the dressed states, one simply notes that if the parallel dressed state is $|e\rangle$ at the

beginning of the ARP inversion, then it must be $e^{-i\gamma}|g\rangle$ at the end. Therefore, an ARP drive field that is initially aligned with a bare state will invert population while adding a dynamic phase factor.

Dynamic phases are an important source of dephasing for interferometers in which the ARP drive field and Bloch vector are necessarily non-parallel [63]. In the dressed state picture, the atomic state is now a superposition of parallel and antiparallel basis states, which acquire differential phases $\pm\gamma$ during the ARP pulse. Inspection of the dressed state transformation in Eq. (2.40) reveals that, since $\theta(0) = 0$ and $\theta(T_\pi) = \pi$, the differential dynamic phases propagate with the bare states after the ARP pulse. Subsequent interferometer pulses generally map these phases into detectable population amplitudes. Since the dynamic phase depends on optical intensity, laser beams with poor spatial quality can dephase the atom ensemble and reduce contrast. Dynamic phase, however, cancels after application of two consecutive, identical ARP inversion pulses in the adiabatic limit, as can be shown using Eqs. (2.40) and (2.41). This cancellation is important for interferometers involving more than two Raman ARP pulses, as will be shown in Chapter 5.

Interestingly, the two-pulse Ramsey sequence is insensitive to dynamic phase in the adiabatic limit. During the first Ramsey ARP beamsplitter, the alignment of the drive field with the Bloch vector results in an overall dynamic phase γ_1, which is undetectable. The second ARP beamsplitter acts on a superposition of dressed eigenstates (i.e., non-parallel Bloch vector and drive field), thus introducing a relative dynamic phase γ_2 between the bare states. Importantly, the readout sequence is insensitive to γ_2, since it has not been mapped into population. In reality though, the dynamic phase cannot be completely suppressed, due to the finite adiabaticity of any practical ARP implementation. Phase noise in ARP Ramsey sequences will be discussed further in Secs. 4.4.3, 4.4.4, and 4.5.

2.4 Laser cooling

As mentioned in Sec. 1.3.2, we produce cold atom ensembles in this work using a magneto-optical trap (MOT). A MOT cools atoms using radiation pressure from three orthogonal pairs of counter-propagating laser beams. Furthermore, the beams are circularly polarized and overlapped in an ultrahigh vacuum environment containing a vapor of alkali-metal atoms. Finally, the laser frequencies are red-detuned with respect to an atomic transition. If an atom in the overlap region moves toward a particular beam, the Doppler shift brings that beam closer to resonance. The atom then preferentially absorbs photons from this beam and receives momentum kicks that tend to counteract its velocity. Randomly-oriented spontaneous emissions produce no net momentum transfer over many scattering events. As a result, the laser beam generates a velocity-dependent damping force that slows the atom [43]. A stable trap requires position and velocity-dependent restoring forces. To produce a position-dependent force, a quadrupole magnetic field can be added to the laser-cooling beams. Through the Zeeman effect, this field introduces position-dependent shifts in the atomic resonance that induce preferential scattering of photons toward the zero of the magnetic field.

Laser-cooled atoms enable long interrogation times for improved sensitivity in atom interferometers. For the longest interrogations, cold atoms are launched upward in a fountain-like trajectory. Kasevich and Chu demonstrated the first atomic fountain and used it to interferometrically resolve the ^{133}Cs hyperfine splitting frequency to within 2 Hz in a single measurement [87]. The atoms were launched by tuning the MOT frequencies to provide cooling in a moving reference frame. Atomic fountains have since been employed in high precision inertial and timekeeping measurements, such as the NIST-F1 atomic time standard [88]. A laser-cooled cloud also serves as a nearly ideal proof mass for accelerometry, given that the atoms are physically isolated from external forces. Additionally, since the atoms are slow-moving, they naturally occupy a small volume and afford compactness. Even colder atom temperatures ($\leq$ 100 nK) have been achieved through evaporative cooling, or "boiling

off," of energetic atoms. The simultaneous increase in sample density results in Bose-Einstein condensation (BEC) [89, 90], in which constituent particles are described by a macroscopic wavefunction. At present, evaporative cooling places prohibitive limits on data-rates [91] for dynamic sensing, while also reducing atom number by a factor of $\sim$100. The loss of atoms reduces the atom shot-noise-limited signal-to-noise ratio (SNR) by roughly a factor of 10.

A simplified MOT, diagrammed in 2-12, is based on one laser beam and a pyramidal or conical retroreflector [92], and has proven useful for generating laser-cooled atom clouds in compact systems. Demonstration of a cold atom gravimeter with this laser-cooling approach has already achieved a sensitivity of 170 ng$/\sqrt{\text{Hz}}$ [93]. A useful simplification for traditional six-beam MOTs involves replacing collimated beams with diverging beams emanating from an optical fiber tip. This approach eliminates optics, yet still allows for cold atom recapture and atom launching [48]. A striking example of the progress to date is the demonstration of a MOT for diatomic molecules [94], which extends the technique to a system with highly complex internal structure, including a multitude of rotational and vibrational resonances.

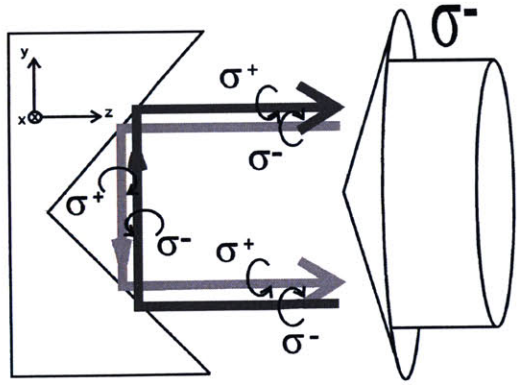

Figure 2-12: Single-beam magneto-optical trap. Atoms are trapped at the center of a conical or pyramidal retroreflector, which reflects one circularly-polarized laser beam. The necessary optical polarizations are achieved through reflection off the metal-coated reflector.

Chapter 3

Apparatus and methods

This chapter describes the apparatus used for demonstrations of atom interferometry with Raman adiabatic rapid passage (ARP). Details pertaining to our compact, ultra-high vacuum cell and methods for atom trapping, state preparation, and state detection are presented. We also discuss how Raman frequencies are generated in timekeeping and accelerometry experiments and conclude with an evaluation of the inertial stability of the apparatus.

3.1 Vacuum chamber

Atom interferometers generally require coherence over ~1-1000 ms to achieve high sensitivity. To reach such long coherence times, collisions with non-interfering background atoms must be suppressed by operating the atom interferometers in ultra-high vacuum. In this work, ultra-high vacuum was established in an octagonal, 80-cm^3 glass cell (Precision Glassblowing) pictured in Fig. 3-1. The cell was based on a machined quartz frame, with 1" and 2.3"-diameter optical flats serving as windows. The optical flats were fused to the frame at relatively low temperatures using quartz frits. Because of these low temperatures, the optical flats were minimally distorted during the bonding process ($<\lambda/10$). The cell maintained a background vapor pressure of 3×10^{-9} Torr, which was achieved by evacuating it with a turbomolecular pump and baking the system at 150° C. After the bakeout, vacuum was maintained with a 200

L/s getter pump (SAES CapaciTorr, St 185 Ti-V alloy) and a 2 L/s ion pump. These pumps were attached to the cell via the metal flange diagrammed in Fig. 3-1.

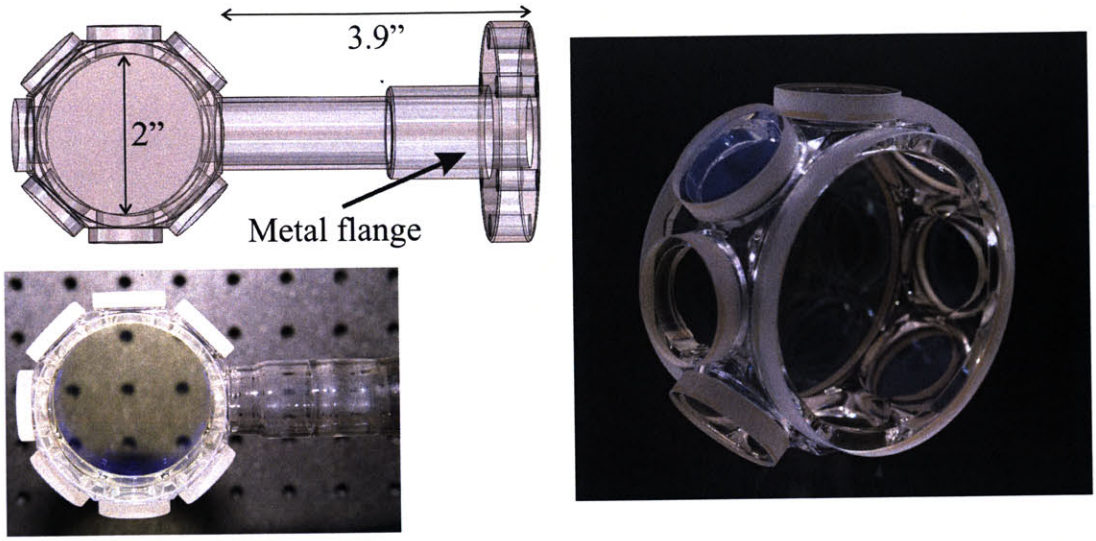

Figure 3-1: Octagonal, all-glass, 80 cm^3 ultra-high vacuum cell. Optical flats ($\lambda/10$) were fused to a machined quartz frame using quartz frits, and a glass-to-metal seal at the neck enabled use with conventional vacuum hardware.

The octagonal, all-glass design allowed for excellent optical access, accommodating three orthogonal beam pairs for laser cooling, as well as beams for state preparation, read out, and Raman atom optics. A diagram of the beam configuration and the overall apparatus is shown in Fig. 3-2. The large windows enabled fluorescence detection optics to be placed in close proximity to the atoms. Both sides of the windows reflected 4% of the 852-nm light used in our experiments. A second cell with an appropriate anti-reflection coating reduced back-reflections to <1%. The glass design also eliminated eddy currents that would have arisen with a traditional metal chamber positioned between pairs of magnetic coils. Eddy currents near the atoms are problematic, as they degrade the temporal and spatial uniformity of magnetic environments.

Cesium atoms in the vacuum chamber were sourced by a current-driven alkali metal dispenser (SAES, 5.2 mg). During bakeout, the dispenser was heated (via operation at 3 A) to expel trapped hydrogen and prevent adsorption of water molecules. We positioned the dispenser in the neck of the cell so that cesium atoms were emitted

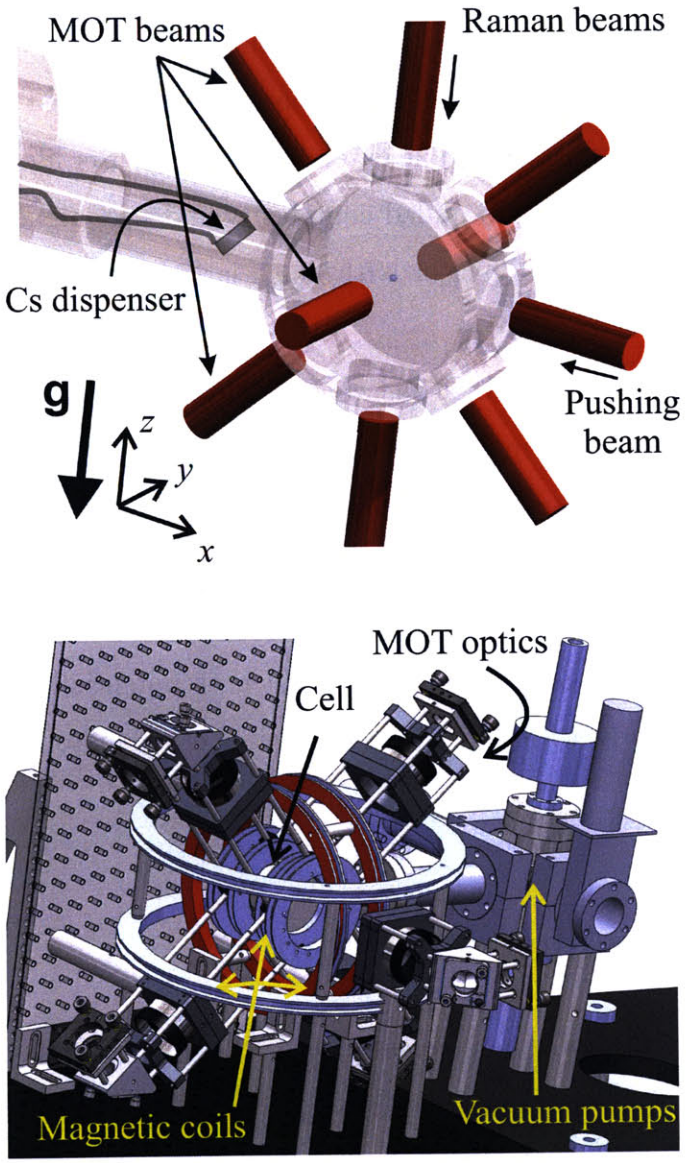

Figure 3-2: Configuration of laser beams and vacuum hardware for atom trapping and interferometry. A conventional six-beam MOT was used to trap and cool atoms.

with a flux directed toward the atom trapping region. The flux and background cesium vapor were controlled using the dispenser current. At a fixed dispenser current setting of 3 A, atoms were loaded into the magneto-optical trap (MOT) at a rate of 0.7 s^{-1}. The steady state atom number was $\sim 1 \times 10^6$. In other applications, the dispenser is typically operated at 4.5-7.5 A, and the resulting evaporation rate depletes the cesium supply in about 20 min. Operation at 3 A provided both a cesium flux and background vapor pressure, while extending the dispenser lifetime to over 3 years with daily usage. At the cost of added complexity and size, higher loading rates can be achieved with a 2D MOT [95] or with much larger 3D MOT beams and optical powers [96].

Achieving zero-power ultra-high vacuum remains an important challenge for many atomic sensors intended for multi-year operation. Unsaturated getter pumps require no power and efficiently trap many abundant gases (e.g., N_2, H_2O, CO_2, H_2) for extended periods of time in ultra-high vacuum. Removal of noble gasses, however, requires an ion pump. Helium is a particularly troublesome noble gas, because of its ability to diffuse through glass. This problem is potentially solved through use of a titanium cell body with sapphire windows or other materials with low helium permeability.

3.2 Atom cooling and trapping

Cold atom samples in this work were produced by trapping cesium atoms in a MOT and cooling them further in an optical molasses. Our MOT used six laser beams, with the geometry shown in Fig. 3-2, to trap $\sim 3 \times 10^5$ atoms in 500 ms at the start of each measurement cycle. The loading time was shortened by roughly a factor of 4 in some experiments to increase the data-rate. Cooling light drove the $F = 4 \rightarrow F' = 5$ cycling transition in cesium (F' denotes an excited hyperfine level on the D2 line). A repump beam, resonant with the $F = 3 \rightarrow F' = 4$ transition, prevented accumulation of atoms in the $F = 3$ hyperfine ground state due to off-resonant cooling excitations. Following trapping, the MOT quadrupole field was shut

off and the cooling light was attenuated and detuned by $8\Gamma = 40$ MHz for 2 ms to reduce the cloud temperature to 9 μK. Prior to reaching the atoms, the MOT beams were collimated to a $1/e^2$ intensity diameter of 1 cm and circularly polarized after passing through polarizing beamsplitter cubes and quarter wave plates. Each beam delivered $6I_{sat}$ of optical intensity[1] to the atoms. After the cell, the each beam passed through a second quarter wave plate and was retroreflected to create the opposing MOT beams. The three beam pairs were orthogonally oriented and overlapped near the center of the vacuum chamber, and the retroreflections were adjusted slightly to optimize cooling and atom number. Switching to the second cell, with anti-reflection coated windows, did not noticeably increase the number of trapped atoms or reduce the atom temperature, suggesting that backreflections from the original cell windows did not measurably impact the MOT.

The cooling and repump frequencies were generated by two 852-nm Toptica TA 100 laser systems, each of which comprised an external cavity diode laser seeding a tapered diode amplifier (TA). The amplified outputs were fiber coupled such that the cooling (repump) laser generated 250 mW (150 mW) of optical power at the fiber output. We used saturated absorption spectroscopy [97] to frequency lock both lasers, with the repump laser locking to the $F = 3 \rightarrow F' = 3/4$ crossover feature, and the cooling laser locking to the $F = 4 \rightarrow F' = 4/5$ crossover feature. As shown in the optics diagram in Fig. 3-3, the cooling laser output was passed through a series of two acousto-optic modulators (AOMs) (Isomet), which provided MHz-scale frequency control and optical beam switching with 100-ns transients. The first AOM was double-passed to enable fine changes in frequency without a corresponding change in optical intensity; the second AOM was single-passed to act primarily as a switch and fixed frequency shifter. Following the AOMs, the cooling light was amplified by a second TA[2] and divided into three paths to generate the MOT beams. The three separated beams were then coupled into polarization-maintaining fibers and delivered to the MOT beam collimators near the vacuum cell. Light from the

[1] $I_{sat} = 1.1$ mW/cm^2 for ^{133}Cs.

[2] All TAs outside the Toptica TA 100 laser systems were built in-house. A detailed description of the design is provided in [46].

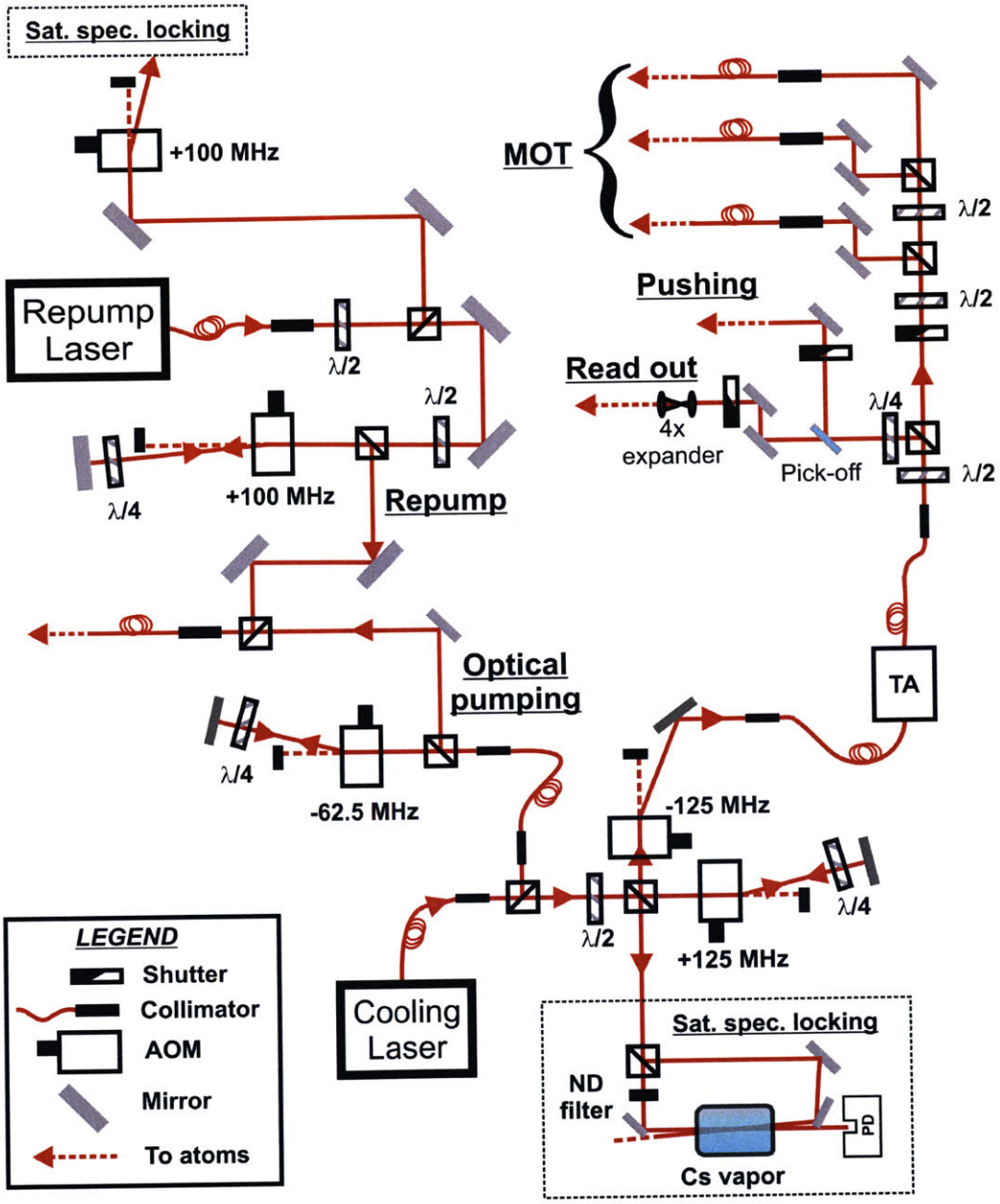

Figure 3-3: Diagram of electo-optics used for atom trapping and state preparation.

repump laser was initially divided into two beam paths: one for frequency locking with saturated absorption spectroscopy and the other for atom manipulations. A single-passed AOM frequency-shifted the first beam by +100 MHz, so that locking to the prominent $F = 3 \rightarrow F' = 3/4$ crossover feature meant the laser was operating at the $F = 3 \rightarrow F' = 3$ transition. Light from the second beam path was double-passed through another AOM to reach the $F = 3 \rightarrow F' = 4$ resonance. This light was fiber coupled, directed to the cell, and collimated to a $1/e^2$ intensity diameter of 5 mm.

The quadrupole magnetic field for the MOT was provided by two 80-mm magnetic coils in an anti-Helmholtz configuration. Each coil encircled a large window on the vacuum cell. Running 2.3 A of current through the coils produced a 10-G/cm field gradient. A solid state relay enabled rapid switch-on of the current. Zener diodes connected in parallel dissipated the back-EMF when the relayed closed, thus shortening the switch-off time to about 100 μs. Environmental magnetic fields were canceled by three orthogonal pairs of coils in an approximate Helmholtz arrangement. Magnetic shielding was not compulsory for this work, because the cold atoms traversed ~1-mm distances during interferometry. However, temporal variations in the environmental magnetic field did ultimately limit the stability of our atomic frequency reference, as discussed in Sec. 4.5. Demonstration of good long-term clock stability will require the addition of magnetic shields.

The experimental sequence was programmed in LabVIEW and executed using a National Instruments PXI-1042Q real-time embedded controller. This controller was responsible for data acquisition, frequency tuning and timing of AOMs, and timing of mechanical shutters and magnetic fields. Raman pulses were controlled by an arbitrary waveform generator, which accepted a trigger from the PXI controller signaling the start of interferometry.

3.3 State preparation

Prior to interferometry, cold atoms from the MOT were prepared in the magnetically-insensitive $|F = 3, m_F = 0\rangle$ ground state, where m_F identifies the Zeeman sublevel.

The second-order magnetic sensitivity of this state is crucial for precision sensing, as it heavily suppresses noise contributions from environmental electromagnetic fields. State preparation began with the application of a vertical bias field that lifted the degeneracy between various Zeeman sublevels. The bias field was produced by the vertically oriented set of Helmholtz nulling coils with 12" diameters. With the bias field present, atoms were optically pumped for 100 μs on the $F = 4 \rightarrow F' = 4$ transition, with light polarized linearly and parallel to the field, until $>90\%$ of the sample was in the $|F = 4, m_F = 0\rangle$ dark state. Repump light simultaneously removed atoms that decayed to the $F = 3$ ground state. The optical pumping efficiency was verified by probing for transitions between magnetically sensitive states once pumping was complete. Measurements of transition probability as a function of microwave π pulse detuning, shown in Fig. 3-4(a), indicated that over 90% of the atoms were in the desired state. To finish state preparation, a resonant, 90-μs microwave π pulse transferred atoms in $|F = 4, m_F = 0\rangle$ to $|F = 3, m_F = 0\rangle$, and a subsequent pulse of cooling light pushed lingering atoms in $F = 4$ out of the interaction region. Efficiency of the entire state preparation sequence was checked with another microwave detuning scan. The >97% peak transfer seen in Fig. 3-4(b) indicated that at least this percentage of the remaining atoms were in $|F = 3, m_F = 0\rangle$.

The optical pumping beam used a small fraction of optical power from the Toptica TA 100 cooling laser, as illustrated in Fig. 3-3. This light was diverted from the cooling beam path and switched by a double-passed AOM. Double-passing also down-shifted the frequency by 125 MHz to make the beam resonant with the $F = 4 \rightarrow F' = 4$ transition. The beam was then overlapped with repump light, and both frequencies were directed at the atoms with the same fiber-coupled collimator. The optical pumping and repump beams were linearly polarized by a Glan-Thompson polarizer. For state preparation, the pushing pulse used cooling light from a dedicated beam shown in Fig. 3-3. An RF signal generator (Aeroflex 2042) supplied the microwave signal used for state preparation. Specifically, a 4.6-GHz signal was frequency-doubled, amplified (Microwave Power LO809-35), and transmitted through a low-loss coaxial cable to a microwave horn. A high-frequency RF switch (Mini-Circuits ZASWA-2-50DR+)

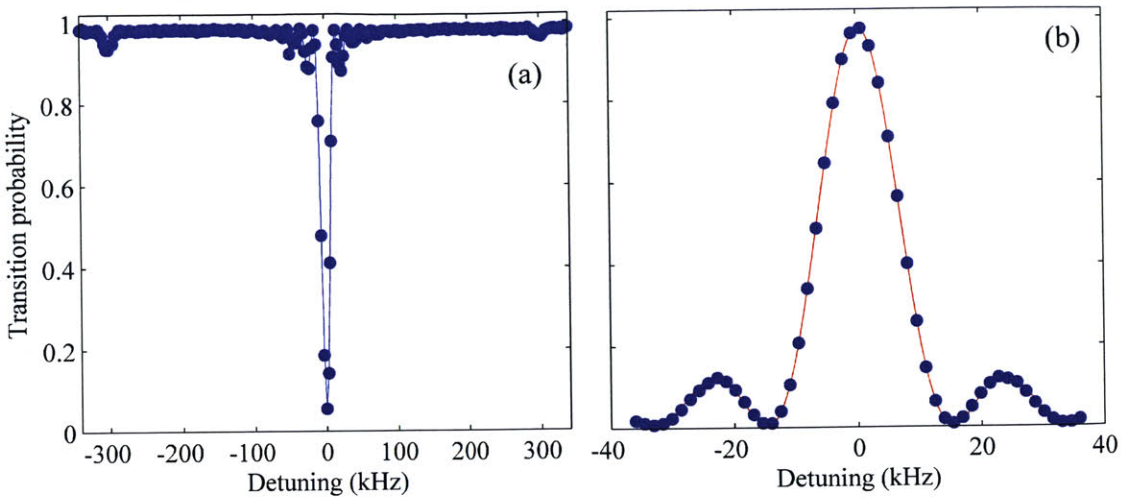

Figure 3-4: Efficiency of optical pumping and state preparation. (a) Optical pumping on the $F = 4 \rightarrow F' = 4$ transition put >90% of atoms in the desired state. (b) After applying a pusher pulse to remove atoms in undesired states, over 97% of the remaining atoms were in the correct state.

provided 70 dB of attenuation and control over microwave pulse duration and timing.

3.4 State detection with laser-induced fluorescence

State preparation was usually followed by the atom interferometer. Atoms exiting the interferometer were in superpositions of the $F = 3$ and $F = 4$ ground states, with weightings that depended on the interferometer phase. To read out this phase, we measured the normalized population difference between the hyperfine ground states using atom fluorescence induced by two laser pulses. The readout sequence began with a 500 μs pulse of cooling light; the resulting fluorescence was associated with atom wavefunctions that had collapsed to $F = 4$. A second pulse of the same light then pushed these atoms out of the interaction region. Remaining atoms in $F = 3$ were pumped to $F = 4$ with 100 μs of repump light and then fluoresced using another pulse of cooling light. The two fluorescence signals f_3, f_4 were proportional to the population in each ground state. We assessed the interferometer phase by calculating the normalized $F = 4$ population $f_4/(f_3 + f_4)$.

Fluorescence was measured using a high-gain photodetector (6×10^8 V/A transimpedance gain; 1.5-kHz bandwidth). A typical fluorescence trace is shown in Fig. 3-5(a), in which 70% of the atoms were in $F = 4$; shapes of the peaks were bandwidth-limited by the photodetector. A 2f imaging system was used to capture the fluorescence. The photodetector was placed 25–35 mm behind a system of plano-convex lenses with an effective focal length of f = 16 mm, and the lens system was positioned 2f away from the atoms. The overall collection efficiency was ~1%. The fluorescence-inducing pulses were red-detuned by 1 MHz and retroflected to balance scattering forces, thus providing $2.5I_{sat}$ of optical intensity. The pulses traveled nearly vertically through the cell, at a small angle with respect to the quantization axis. This orientation eliminated one source of readout sensitivity to cloud position, since the falling atoms remained inside the laser beam over varying measurement intervals.

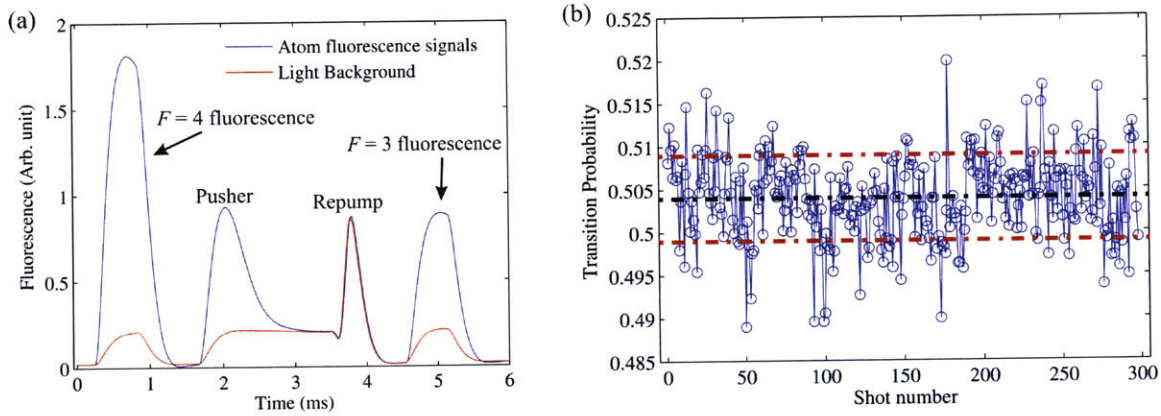

Figure 3-5: Performance of state detection based on laser-induced atomic fluorescence. (a) Experimental trace of measured fluorescence and light background. The photodetector witnessed pusher and repump laser pulses due to scattered light from the vacuum cell. (b) Evaluation of readout-limited SNR using a Raman Ramsey clock with $T = 500$ μs. The limit on phase SNR was $\sigma_\Phi^{-1} = A \times 100$, where A is interferometer contrast.

Fluorescence measurements typically contained backgrounds that were about 10% of the total signal $f_3 + f_4$, due to scattered light from the vacuum cell. This light background, also shown in Fig. 3-5(a), was subtracted from every experimental shot using the following procedure: the ratio of the light background signal to readout optical power was calibrated at the beginning of each experiment by capturing several

shots with the MOT shut off, while also sampling the readout pulse intensity. For the remainder of the experiment, this ratio was used with additional measurements of readout power to predict and subtract the light background on a per-shot basis.

Detection noise creates instabilities in transition probability measurements that can contribute to perceived interferometer phase noise. Recall that interferometers infer phase deviations from transition probability measurements made near the mid-point of a fringe. Since the transition probability P is related to phase Φ by the equation $P = 0.5 \pm 0.5A\cos(\Phi) + B$, propagation of uncertainties dictates that if $\Phi \approx \pi/2$, the uncertainty in Φ is

$$\sigma_\Phi = \frac{2}{A}\sigma_P, \tag{3.1}$$

where σ_P is the uncertainty in transition probability. Therefore, when detection noise dominates σ_P, it also registers as a phase instability. We assessed the detection signal-to-noise ratio (SNR) σ_Φ^{-1} using a Ramsey sequence with two Raman $\pi/2$ pulses and a 500-μs dwell time. A short dwell time was chosen to suppress the frequency sensitivity of the interferometer. The Ramsey sequence was operated near the fringe mid-point for several experimental shots, resulting in a standard deviation for the measured transition probabilities of $\sigma_P = 0.005$ (see Fig. 3-5(b)). The detection SNR was then $\sigma_\Phi^{-1} = A \times 100$, implying that the per-shot phase resolution was limited by detection noise to $\sigma_\Phi = 10$ mrad in an interferometer with contrast $A = 1$.

A normalized readout eliminated sensitivity to shot-to-shot fluctuations in atom number, as well as laser intensity and frequency. Normalization, however, did not prevent measurement errors due to laser parameter variation between the first and second readout pulses of a given shot. Measurement errors due to intensity fluctuation were suppressed by applying readout pulses with intensities higher than I_{sat}. Laser frequency uncertainty due to the ~100-kHz linewidth was more problematic. To evaluate the contribution of laser linewidth to the measurement uncertainty, we

rewrite the transition probability as

$$P = \frac{\gamma_{p,4} N_4}{\gamma_{p,3} N_3 + \gamma_{p,4} N_4}, \tag{3.2}$$

where $\gamma_{p,3,4}$ and $N_{3,4}$ are, respectively, the photon scattering rate and atom number for each fluorescence pulse. Assuming the atom population is evenly divided ($N_3 = N_4$), and that the scattering rates and their uncertainties are the same for both pulses, it can be shown that $\sigma_P = \sqrt{2}\sigma_{\gamma_p}/(4\gamma_p)$. Sensitivity of γ_p to laser detuning Δ is characterized by the equation

$$\gamma_p = \frac{\Gamma}{2} \frac{I/I_{sat}}{1 + (I/I_{sat}) + (2\Delta/\Gamma)^2}, \tag{3.3}$$

where Γ^{-1} is the excited state lifetime and I is the optical intensity [43]. Propagating the uncertainty in Δ (~100 kHz) reveals that $\sigma_{\gamma_p}/\gamma_p \approx 1\%$ when $\Delta = 1$ MHz and $I = 2.5 I_{sat}$. Thus, variations in cooling laser frequency limited the readout resolution to $\sigma_P \approx 0.004$, which accounts for over half the detection SNR limit. The limit can be improved upon by increasing the laser pulse intensity, though this increase also brightens the light background. Readout frequency and amplitude sensitivity is eliminated in systems that detect both hyperfine states simultaneously with a single detection pulse. This approach unfortunately requires either large spatial separation between atoms in $F = 3$ and $F = 4$ [53] or absorption imaging with two frequencies (e.g., $F = 4 \rightarrow F' = 5$ and $F = 3 \rightarrow F' = 2$) generated by a common laser. Both solutions would be challenging to implement in a compact sensor operating in dynamic environments.

3.5 Raman frequency generation and optics

3.5.1 Doppler-insensitive Raman optics

The Raman optical frequencies were generated by a Toptica DL 100 external cavity diode laser. To reduce spontaneous emission, we red-detuned this master laser by

2 GHz with respect to the $F = 3 \rightarrow F' = 4$ transition. Frequency locking with a large detuning offset was accomplished using a combination of saturated absorption spectroscopy and phase modulation. As illustrated in Fig. 3-6(a), a small fraction of the laser output power was diverted to a fiber-coupled electro-optic modulator (EOM) that phase modulated the light at ~2 GHz. The resulting optical spectrum contained frequency sidebands spaced about the carrier by integer multiples of the microwave frequency driving the EOM. We used saturated absorption spectroscopy with the first-order positive sideband to lock the laser. Since this sideband was necessarily resonant, the laser carrier frequency ω_c was red-detuned by the EOM driving frequency (i.e., $\Delta \sim -2$ GHz).

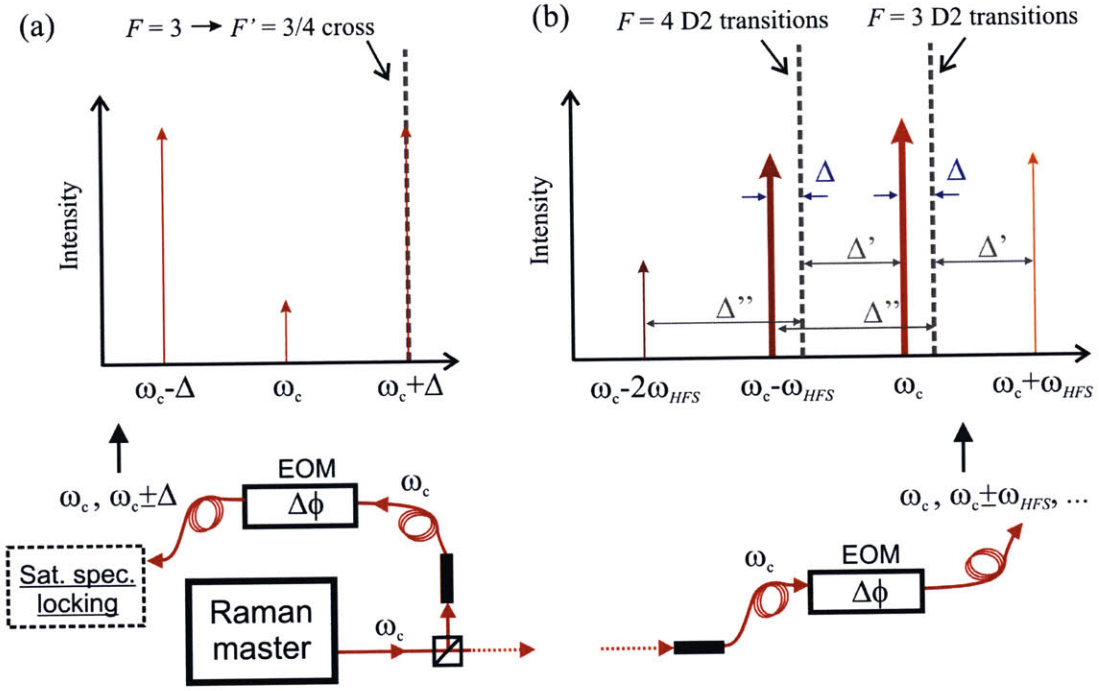

Figure 3-6: Raman master laser offset lock and phase modulation. (a) An EOM phase modulated the master laser output ω_c at frequency Δ, and the laser was locked using the positive first-order sideband. (b) Raman frequencies were generated by a second EOM driven near $\omega_{HFS}/(2\pi)$. Multiple Raman transitions were possible, with relative strengths determined by corresponding laser detunings. Bold arrows (red and maroon) represent frequency components that drove the dominant Raman transition.

The detuned (and unmodulated) output of the master laser provided one of the Raman optical frequencies. The second Raman frequency was generated by an ad-

ditional stage of phase modulation with an EOM. The driving frequency for the second EOM was generally set to the Zeeman-shifted hyperfine splitting frequency $\omega_{HFS}/(2\pi) = 9192631770 + 324$ Hz. As indicated by the thick red and maroon arrows in Fig. 3-6, the carrier and -1 sideband frequencies drove the dominant Raman transition. For timekeeping experiments, which used Doppler-insensitive, co-propagating Raman frequencies, the entire phase modulated spectrum was applied to the atoms. Other frequency pairs that satisfied the two-photon resonance condition drove much weaker Raman transitions due to their larger single-photon detunings, labeled Δ' and Δ'' in Fig. 3-6. The three-frequency Raman system, in which Raman transitions are driven by pairings of the carrier frequency with both first-order sidebands, has been studied analytically in [98]. Depending on the sign of Δ, the weaker Raman transition essentially adds or subtracts from the two-photon Rabi rate due to optical interference.

The Raman pulse detuning and phase were controlled using the microwave signal that drove the EOM. To obtain agile control over these experimental parameters, we used a single-sideband mixer (Polyphase SSB90110A) to combine the 30 MHz output of a 625 MS/s arbitrary waveform generator (Agilent N8241A) with a constant 9.163 GHz signal (Agilent E8257D). The phase, frequency, and power of the resulting RF signal were controlled through the waveform generator, enabling rapid frequency sweeps for Raman ARP. Figure 3-7 provides a simplified block diagram of the associated RF circuitry. As shown in the optics diagram in Fig. 3-8, an AOM placed

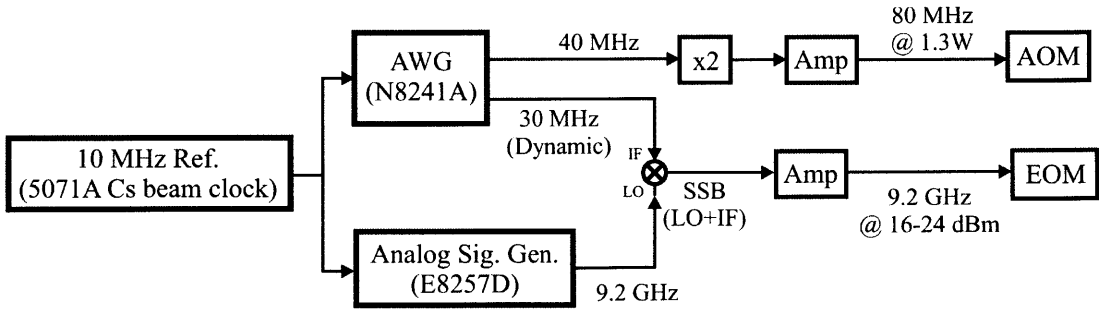

Figure 3-7: Microwave circuit block diagram for Raman frequency generation. Agile control over Raman frequency and phase was achieved using the dynamic 30-MHz signal from the arbitrary waveform generator (AWG).

before the second EOM switched the Raman light in 50 ns, and a tapered amplifier downstream of the EOM typically increased the total Raman optical power presented to the atoms to ~40 mW. The AOM acoustic wave velocity (3.6 mm/μs) produced a $\sim$ 1 μs delay in optical beam switching, relative to the EOM RF signal, that was corrected for by delaying the EOM signal using the arbitrary waveform generator. Such synchronization errors were problematic for ARP and composite pulses, because of their time-dependent frequencies, phases, and intensities. The optical spectrum of the tapered amplifier contained a 30 nm-wide pedestal carrying a small amount of resonant light. To reduce spontaneous emission during the interferometer, we filtered the resonant light from the pedestal by passing the output of the tapered amplifier through a Cs reference vapor cell. The Raman beam was vertically oriented, circularly polarized, and delivered to the cell using a fiber-coupled collimator with 7.1 mm $1/e^2$ intensity diameter and wavefront aberrations of $< \lambda/10$ (Silicon Lightwave Technologies LB10). At a -2-GHz master laser detuning, the differential AC Stark shift was canceled when the optical power was ~10% larger in the carrier frequency than in each first-order sideband. Additionally, the Doppler-insensitive Raman resonance had a residual Doppler sensitivity that shifted resonance by 30.7 Hz/(m/s), or 0.3 Hz/ms in a 1 g environment.

To generate an interferogram, we often measured the transition probability while shifting the Raman phase offset φ. This phase was scanned over several values, typically in steps of $\pi/4$ rad, and the transition probability at each phase was measured multiple times (consecutively) to enable averaging. With a per-shot data-rate of 1.5-5 Hz, a full interferogram was usually acquired in under 1 min.

3.5.2 Doppler-sensitive Raman optics

For inertially sensitive interferometry with ARP, additional lasers and optics were required for Raman frequency generation. The Raman frequencies in this case were produced by two injection-locked Fabry-Perot slave lasers (Blue Sky VPSLO850-150X9B). As the diagram in Fig. 3-9 shows, both lasers were seeded by the Raman master laser, which was red-detuned from the $F = 3 \rightarrow F' = 4$ transition by

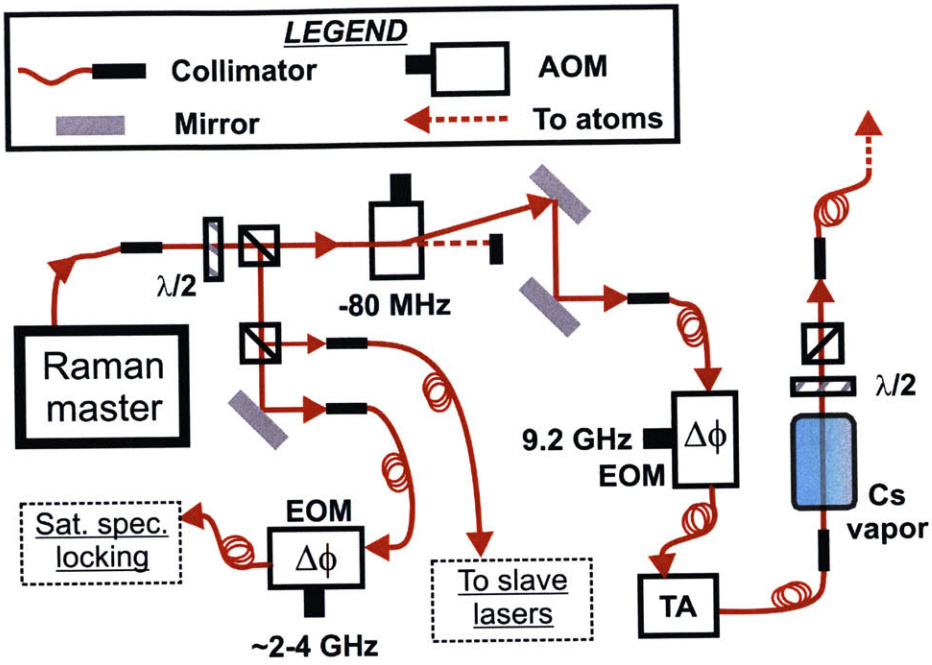

Figure 3-8: Diagram of electro-optics for Doppler insensitive (co-propagating) Raman frequency generation.

$\Delta = -3.9$ GHz to reduce spontaneous emission. The master laser was phase modulated to create frequency sidebands spaced by ~9-GHz intervals. Each slave laser was seeded with roughly 100 μW of optical power from the phase modulated beam and tuned to predominantly amplify either the carrier or the negative first-order frequency sideband. In this manner, two physically separated Raman frequencies were created, and the RF signal driving the EOM still controlled the Raman detuning and phase. Residual amplification of neighboring sidebands by each slave laser produced undesired frequency content with $1 - 5\%$ of the optical power in the primary frequency component. If the EOM drive frequency had been set to $\omega_{HFS}/(2\pi)$, coupling between the residual and primary frequencies in each slave laser would have driven Doppler-insensitive transitions. Therefore, a double-passed AOM frequency-shifted the seed for slave laser 1, which primarily amplified the -1 frequency sideband, by 160 MHz. The EOM phase modulation was then set to $\omega_{HFS}/(2\pi) + 160$ MHz so that the slave laser difference frequency matched the Raman resonance condition. In turn, Doppler-insensitive transitions were detuned by 160 MHz (i.e., ~1000 linewdiths).

During an interferometer sequence, the Raman frequency difference was chirped at ± 23 kHz/ms to continually match the Doppler-shifted Raman resonance in a 1-g environment. The sign of the chirp rate was determined by the orientation of the effective Raman wave vector $\mathbf{k}_{\text{eff}}$.

The two Raman beams were delivered to the atoms in a counter-propagating, vertical orientation via two polarization maintaining fibers. As indicated in Fig. 3-2, the downward (upward) beam entered the vacuum cell through the top (bottom) window. The beams were linearly cross-polarized by polarizing beamsplitter cubes and collimated to a 7.1-mm $1/e^2$ intensity diameter by commercial fiber-coupler collimators. Each beam delivered one Raman frequency at any given time. Relative alignment of the Raman beams was verified by coupling light from one beam into the fiber collimator of the other beam. Each Raman collimator was mounted to enable adjustment of its Euler pitch and yaw angles, as well as linear translations in the plane orthogonal to the beam axis. This method aligned the beam axes to within $\sim$1 mrad of each other. The beams were then centered on the atom cloud by driving Doppler-insensitive Rabi oscillations and translating the collimators to minimize the oscillation decay rate.

A combination of two AOMs and polarization-selective optics, shown in the lower lefthand side of Fig. 3-9, enabled rapid optical switching ($\sim$50 ns) of the beams and reversal of $\mathbf{k}_{\text{eff}}$. Specifically, the outputs of the slave lasers were orthogonally polarized, overlapped on a polarizing beamsplitter cube, and directed through a switchyard of two AOMs. The outputs of each AOM, represented by the blue and green beam paths, carried both cross-polarized Raman frequencies and were never switched on simultaneously. Since each beam entered the downstream polarizing beamsplitter cube through a different input port, the AOMs determined the output port from which a particular Raman frequency exited the beamsplitter. The beams were then coupled into optical fibers that routed light to the atoms. Depending on which AOM was switched on, the Raman frequencies could take either optics path downsteam of the polarizing beamsplitter cube, thereby reversing the directions of $\mathbf{k}_1$ and $\mathbf{k}_2$, and consequently $\mathbf{k}_{\text{eff}}$. We boosted the optical power in each Raman beam to $\sim$100 mW

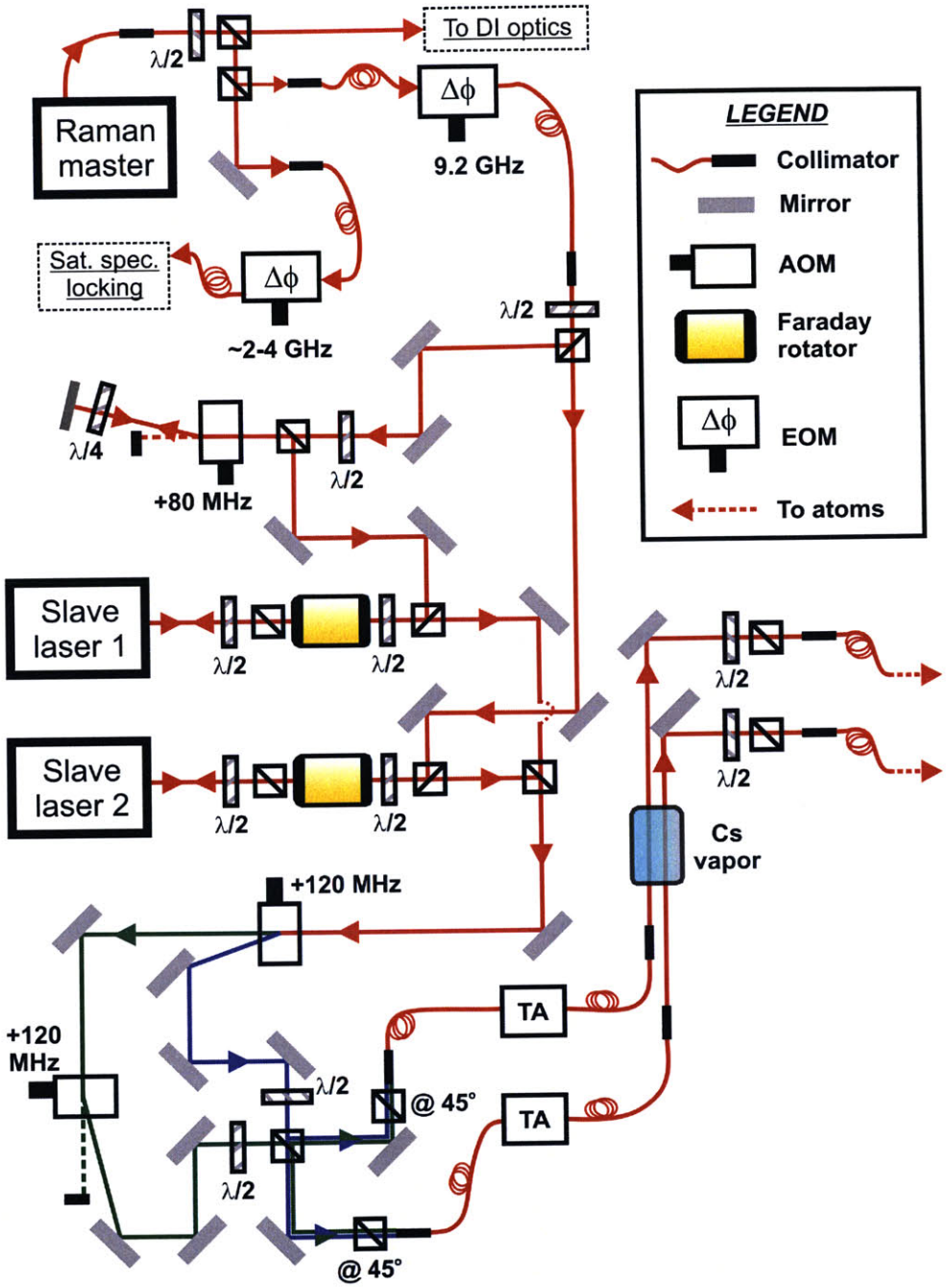

Figure 3-9: Diagram of electro-optics from generation of separated Raman frequencies, used for Doppler sensitive (counter-propagating) Raman transitions.

with two TAs. The TA drive currents were also tuned relatively to obtain a ratio of optical powers that canceled the differential AC Stark shift of the clock states.

3.6 Inertial stability assessment

In a simpler method for inertially sensitive atom interferometry, counter-propagation of the Raman frequencies was achieved by retroreflecting the full spectrum of frequency sidebands pictured in Fig. 3-6(b). The two primary Raman frequencies thus traveled upward and downward through the vacuum cell, and pairings of these frequencies produced two Raman processes—one with $\mathbf{k}_{\text{eff}} = \mathbf{k}_1 - \mathbf{k}_2$, and the other with $\mathbf{k}_{\text{eff}} = \mathbf{k}_2 - \mathbf{k}_1$ [99]. The anti-parallel orientation of these vectors changed the sign of the Doppler shift in the Raman resonance condition. As a result, the appropriate choice of Raman detuning made it possible to drive each Raman transition selectively. In a vertical orientation, for example, the atom cloud gained velocity during free fall, resulting in a Doppler-induced separation of the resonances at a rate of $2k_{\text{eff}}g/(2\pi) = 2 \times 23$ kHz/ms. Without this Raman resonance splitting, both transitions would have occurred simultaneously [100]. An atom beam splitter would then have produced more than two momentum states, thus breaking the symmetry of the Mach-Zehnder interferometer.

Retroreflected Raman pulses offer important practical benefits for atom interferometric gravimetry. Sourcing both Raman frequencies from one laser reduces phase noise, since variations in laser phase are common to both frequency components. Additionally, variations in Raman beam path length are less problematic: the only portion of the path not common to both Raman frequencies is the segment between the atoms and the retroreflecting mirror. Motion of other optical elements in the path equally shifts both Raman laser phases ϕ_1 and ϕ_2, resulting in a fixed effective Raman phase $\varphi = \phi_1 - \phi_2$. If the Raman frequencies are physically separated, as in the approach described in Sec. 3.5.2, variations in path length are no longer common-mode and result in added phase noise. In the present approach, interferometer sensitivity to acceleration results from motion of the atom cloud with respect to

the retroreflector. As a result, vibration of this mirror can also lead to noise in φ. Phase perturbations during a three-pulse Mach-Zehnder interferometer combine to shift the phase by $\delta\varphi_1 - 2\delta\varphi_2 + \delta\varphi_3$, where subscripts denote the pulse number. If the mirror is stationary during the interferometer, its contribution to the phase cancels.

We used a retroreflected Raman beam to test the inertial stability of the apparatus. To stably reflect the beam, a corner cube reflector was mounted on a passive vibration isolation stage (Minus K 10BM-10) placed above the vacuum cell on a rigid aluminum platform. Compared to flat mirrors, corner cubes improve pointing stability, since the direction of the reflected beam is independent of reflector orientation. Importantly, the Raman beam collimator was rigidly mounted to the floated optical table on which the apparatus was built. Local gravity was measured using a Mach-Zehnder atom interferometer, with a π pulse time of 10 μs ($\Delta = -1$ GHz) and contrast of 0.5. Measurements were acquired for 30 min with a data-rate of 3.6 Hz and a dwell time of $T = 3.5$ ms, while operating the interferometer with a $\varphi = \pi/2$ phase offset (i.e., near the middle of a fringe). Allan deviations of these phase measurements, shown in Fig. 3-10, reveal a short-term stability 30 $\mu g/\sqrt{\text{Hz}}$ and a bias stability of 3 μg at $\tau = 150$ s. The long-term stability may have been limited by milliradian tilts of the floated optical table with respect to vertical. The local value of gravity was found to be 9.80362 ± 0.00003 m/s^2, which deviated from the National Geodetic Survey prediction of local gravity at the 10-ppm level. This discrepancy was largely due to mrad-scale misalignment of the Raman beam with respect to vertical, since an accurate gravity measurement was not a primary focus.

A previous assessment of inertial stability, made without passive vibration isolation, produced a short-term stability of 120 $\mu g/\sqrt{\text{Hz}}$ [46], indicating that environmental vibration was the dominant noise source. This limitation was expected, given that our laboratory is located on the 6$^{\text{th}}$ story of a building in an urban setting and in close proximity to the subway. While vibration-driven noise was heavily suppressed in the more recent measurement, the stability was still roughly 5 times worse than the limit imposed by detection SNR, namely 6 $\mu g/\sqrt{\text{Hz}}$. To monitor residual vibrations of the isolation platform, a seismometer (Endevco 86) measured the acceleration noise

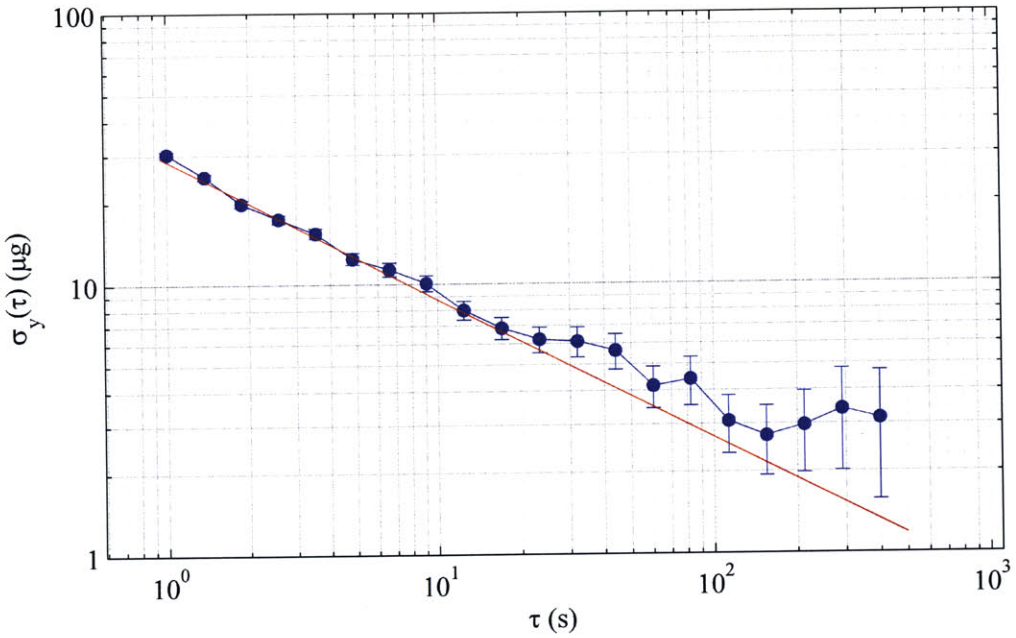

Figure 3-10: Allan deviations characterizing the inertial stability of the testbed. The Doppler-sensitive Mach-Zehnder interferometer had a short-term stability of 30 $\mu g/\sqrt{\text{Hz}}$ and a bias stability of $\sim$3 μg at $\tau = 150$ s. The dwell time and data-rate were $T = 3.5$ ms and 3.6 Hz, respectively, and measurements were acquired for 30 min. The interferometer used a retroreflected Raman laser beam, with the reflector mounted on a passive vibration isolation platform. Milliradian-scale tilts of the floated optical table over several minutes may have limited the bias stability.

experienced by the corner cube reflector. An acceleration noise spectrum, shown in Fig. 3-11(a), was acquired from these measurements and used to estimate its contribution to short-term interferometer instability. The phase uncertainty σ_Φ of the atom interferometer is related to the single-sided acceleration power spectral density $S_a(\omega)$ by the equation

$$\sigma_\Phi^2 = k_{\text{eff}}^2 \int_0^\infty d\omega \, |H(\omega)|^2 \, S_a(\omega), \tag{3.4}$$

where $H(\omega)$ is the frequency response of the Mach-Zehnder sequence [99]:

$$|H(\omega)|^2 = \frac{16}{\omega^4} \sin^4(\omega T/2) \tag{3.5}$$

A plot of $|H(\omega)|^2$ in Fig. 3-11(b) exhibits two interesting behaviors. First, the notches at integer multiples of $\omega = 1/T$ reflect the insensitivity of the accelerometer to mirror motion at these frequencies. The insensitivity results from the mirror returning to the same position for all three Raman pulses, despite moving during the dwell times. Second, the frequency response of $|H(\omega)|^2$ rolls off as $\sim 1/\omega^4$ for $\omega > 1/T$, indicating that the atom interferometer behaves like a second-order low-pass filter.

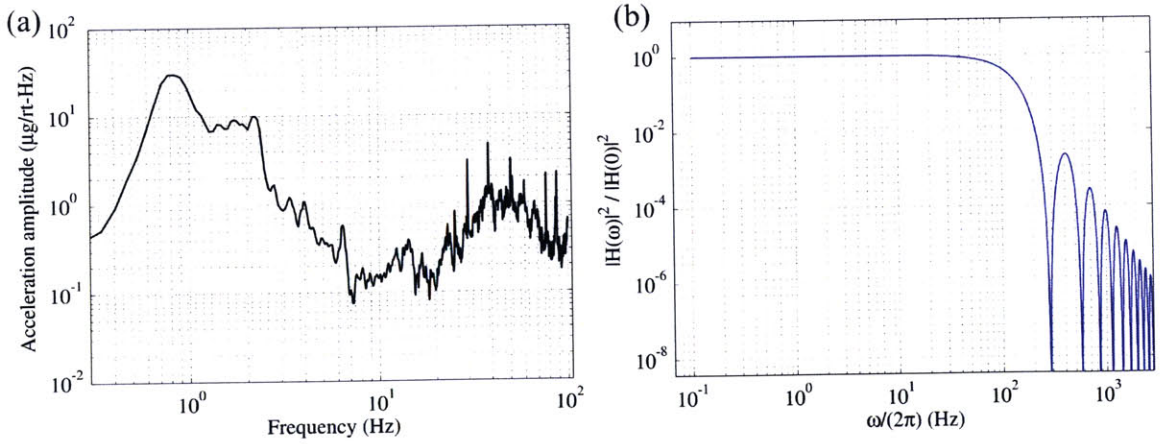

Figure 3-11: Acceleration amplitude spectrum and frequency response of the Mach-Zehnder interferometer. (a) The acceleration amplitude spectrum was measured with a seismometer. (b) The frequency response notch filters inertial inputs at integer multiples of $\omega = 1/T$ and low-pass filters frequencies above $\sim 1/T$.

Applying this frequency response function to the power spectral density, we found from Eq. (3.4) that vibrations added 35 mrad of phase noise per shot. The measured short-term stability, however, corresponded to a per-shot phase noise of 100 mrad, suggesting that the measured acceleration spectral density excluded important high frequency noise content. The spectrum between 100-200 Hz, for example, may have contained resonances and was only partially suppressed by $|H(\omega)|$ (see Fig. 3-11(b)). Furthermore, a separate stability assessment for a Mach-Zehnder interferometer with Doppler insensitive Raman transitions—which are immune to vibration—achieved a per-shot phase noise of 20 mrad (contrast of 0.8). Therefore, it seems likely that residual accelerations, transmitted through the vibration isolation stage, limited the short-term stability of our accelerometer. Raman pulse intensity noise at the $\sim$0.5% level (not actively controlled) was not a major driver of instability. Other noise sources related to microwave frequency generation, the differential AC Stark shift, and inertial effects such as gravity gradients and rotations did not limit the measurement. The interested reader may consult references [99, 46] for additional details on measurement noise and systematic effects.

In this thesis, other inertially sensitive experiments used the Raman beam configuration described in Sec. 3.5.2, in which the Raman frequencies were physically separated by slave lasers. While the retroreflection approach is convenient for gravimetry with resonant Raman pulses, it restricts the useable velocity acceptance of typically wideband ARP atom optics. Wideband atom optics are problematic for retroreflection, because they simultaneously drive both, oppositely-directed Raman transitions and create parasitic double diffraction [100, 101]. Wider velocity acceptances, however, are necessary for our approach to large area atom interferometry, which is presented in Chapter 5. Furthermore, since retroreflection applies twice as much light to the atoms, relative to our separated frequency approach, it effectively doubles the spontaneous emission rate. Separating the Raman frequencies thus reduces the per-pulse spontaneous emission, which is particularly useful for long Raman ARP pulses.

Chapter 4

Robust atomic timekeeping with Raman adiabatic rapid passage

This chapter presents a method for atomic timekeeping that employs atom optics based on Raman adiabatic rapid passage (ARP) [102]. Our demonstration of Ramsey interferometry with Raman ARP suppresses important systematic effects that limit stable clock operation in uncontrolled environments or under dynamics. We also show that perturbations to parameters defining the ARP frequency sweeps do not introduce resolvable shifts in the phase of the Ramsey interferometer. Finally, we investigate the comparative short-term stability of Ramsey sequences based on Raman ARP, resonant Raman, and microwave pulses in our system.

4.1 Motivation

Atomic clocks are vital to modern technologies ranging from the Global Positioning System and distributed networks to communication systems and laboratory instruments. Primary atomic timing references, however, are presently limited to operation in benign environments, large volumes, and mild external dynamics. State-of-the-art atomic fountain clocks, for example, use laboratory-scale systems to realize fractional frequency uncertainties of 3×10^{-16} [19]. These clocks achieve high sensitivity at the expense of size and data-rate, by launching laser cooled alkali atoms over $\sim$1

m distances [87] and implementing long interrogation times with microwave Ramsey sequences [103, 88]. On the other hand, *secondary* frequency references have made tremendous progress toward size and power reduction with the advent of chip-scale atomic clocks (CSACs), which occupy a 17 cm^3 package and consume just 120 mW of electrical power [23, 24]. However, due to the limited long-term stability of CSAC, there remains an unfulfilled need for primary atomic references that operate in a compact and portable package.

One approach to developing a robust, compact primary reference involves interrogating atoms in the trapping region of the vacuum cell and applying Ramsey sequences with short dwell times [30, 31, 104, 105]. This approach trades the high sensitivity of atomic fountain clocks for reduced size and higher data-rate. Importantly, these modifications still allow for significant improvements in long-term stability when compared to what is currently achievable with CSAC. In dynamic environments, a short Ramsey time provides the added benefit of reducing displacements of the atom cloud relative to the Raman beam. If, for example, measurements are completed on a 10-ms time scale, a cold atom cloud experiencing 1-10 g accelerations is displaced from the trap site by <5 mm, enabling interferometry under dynamics, recapture of cold atoms, and fast data-rates with small-diameter laser beams [47, 33].

The traditional method of applying microwave pulses to the atoms in a Ramsey interrogation requires well-engineered cavities or waveguides, which constrain minimum size and may be adversely affected by thermal environments or vibration [106]. An alternative approach that circumvents the cavity employs Raman transitions with optical photons [107]. Optical interrogation, however, introduces challenges distinct from those of microwave interrogation. Variations in laser beam intensity drive spurious phase shifts via the AC Stark effect [82]. Furthermore, the Gaussian intensity profile of the beam creates spatially-dependent Rabi rates that, in some techniques, link Ramsey fringe contrast to radial motion of the cloud. In this work, we experimentally demonstrate that these important systematic effects can be suppressed through use of Ramsey sequences with Raman ARP atom optics.

4.2 Raman adiabatic rapid passage pulses

ARP is particularly useful when inversion is required in the presence of an inhomogeneous drive field [59, 60], as discussed in Sec. 2.3. We implemented ARP with stimulated Raman transitions by sweeping the two-photon detuning and modulating the Raman beam intensity. We reiterate that frequency-swept Raman ARP fundamentally differs from Stimulated Raman Adiabatic Passage (STIRAP), which drives adiabatic transfer in a three-level system using time-delayed intensity modulation of two optical fields satisfying the two- and one-photon resonance conditions. The presence of multiple excited levels in alkali atoms reintroduces residual Stark shifts to STIRAP, with dependencies on pulse duration, optical intensity, and single-photon laser detuning [108]. These shifts are ultimately detrimental to clock stability, but can be suppressed with frequency-swept ARP.

In nuclear magnetic resonance (NMR), many combinations of intensity and frequency modulation provide efficient adiabatic transfer, and should apply equally well to stimulated Raman processes. The simplest approach is to slowly chirp the detuning through resonance while maintaining a constant field intensity. More complex ARPs use nonlinear modulations of intensity and frequency to achieve population inversion that, in some cases, is rapid and wideband or highly-selective. Our interest lies in rapid ARPs, since shorter pulses help minimize spontaneous emission, dephasing from atom motion in a non-uniform laser field, and higher-order interferometer phase shifts due to finite pulse durations. To that end, we focus primarily on the frequency sweep described by the equation [65, 86]

$$\delta(t) = \Omega_{arp} \tan\left[\alpha\left(\frac{2t}{T_\pi} - 1\right)\right], t \in \{0, T_\pi\} \tag{4.1}$$

where T_π sets the total sweep duration, Ω_{arp} controls the sweep rate without perturbing its duration or range, and $\alpha = \arctan(\delta_{max}/\Omega_{arp})$, where δ_{max} is the maximum detuning. Hwang et al. proposed coupling this frequency sweep with an intensity

modulation $I(t)$ of the form [67]

$$I(t) = I_0 \tanh\left[\beta\left(1 - \left|\frac{2t}{T_\pi} - 1\right|\right)\right], \tag{4.2}$$

where I_0 is the maximum intensity, and the unitless parameter β is typically 7.5. Since $I(0) = I(T_\pi) = 0$, the drive field at the beginning and end of the sweep is parallel with the z-axis of the Bloch sphere. This alignment helps maximize transfer efficiency when atoms are prepared in one of the so-called clock states (i.e., $|F = 3; m_F = 0\rangle$ and $|F = 4; m_F = 0\rangle$). For this ARP, the adiabaticity $Q(t) = \Omega_{\text{gen}}(t)/|\dot{\theta}(t)|$ is equivalent to T_π in units of Raman π pulses when the sweep nears resonance and $\Omega_{arp} = \Omega_{\text{eff}}$; away from resonance, Q is orders of magnitude larger.

Figure 4-1 shows simulations (described below) of population inversion for this Tan/Tanh [frequency/intensity] ARP, as well as a variety of other ARPs, as a function of Raman detuning with respect to the center frequency of the frequency sweep. Corresponding frequency and intensity modulations are detailed in Tab. 4.1, along with simulation parameters. Other pulses may be found in [66]. Comparison of the

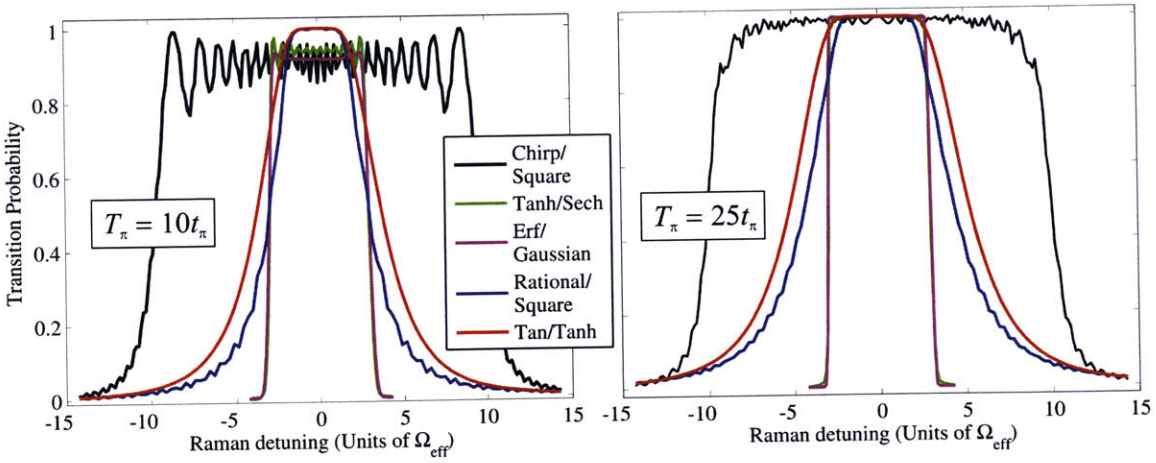

Figure 4-1: Simulations of Raman ARP inversions for different detuning offsets. Shortening the pulse duration from $T_\pi = 25t_\pi$ to $T_\pi = 10t_\pi$ does not degrade the peak transfer efficiency of the Tan/Tanh and Rational/Square ARPs. For suitably long pulses, Tanh/Sech and Erf/Gauss functions provide highly selective inversion bands with sharp edges.

plots in Fig. 4-1 highlights the effects of pulse duration on peak ARP transfer effi-

Pulse	Frequency	Intensity	δ_{max}	Ω_{arp}	β
Tan/Tanh [67]	$\Omega_{arp}\tan[\alpha(2t/T_\pi - 1)]$	$\tanh[\beta(1 - \lvert 2t/T_\pi - 1\rvert)]$	214	1	7.5
Rational/Square [60]	$\Omega_{arp}(2t - T_\pi)/\sqrt{(\xi T_\pi)^2 - (2t - T_\pi)^2}$	1	214	1	—
Tanh/Sech [69]	$\delta_{max}\tanh[\beta(2t/T_\pi - 1)]$	$\mathrm{sech}[\beta(2t/T_\pi - 1)]$	3	—	3
Erf/Gauss [69]	$\delta_{max}\mathrm{erf}[\beta(2t/T_\pi - 1)]$	$\exp[-\beta^2(2t/T_\pi - 1)^2/2]$	3	—	3
Chirp/Square	$\delta_{max}(2t/T_\pi - 1)$	1	10	—	—

Table 4.1: ARP intensity and frequency modulation functions. $t \in \{0, T_\pi\}$, δ_{max} and Ω_{arp} are in units of the maximum Ω_{eff}, and all intensities are scaled by I_0. Note that for intensity-modulated pulses, $\Omega_{\text{eff}}(t = 0 \text{ and } T_\pi)$ is less than the maximum Ω_{eff}. Also, $\alpha \equiv \arctan(\delta_{max}/\Omega_{arp})$ and $\xi \equiv \sqrt{1 + (\Omega_{arp}/\delta_{max})^2}$.

ciency. In particular, only the Tan/Tanh pulse and Rational[1]/Square pulse maintain perfect transfer efficiency near resonance as the duration is shortened from $T_\pi = 25t_\pi$ to $T_\pi = 10t_\pi$ (t_π is the Raman π pulse duration). Interestingly, the frequency modulations of these two ARPs differ markedly from those of the other pulses, as the detunings in these cases accelerate away from resonance near the beginning and end of each pulse (see Fig. 2-11). This feature allows the Tan/Tanh and Rational/Square ARPs to sweep across a wide frequency range without violating the adiabatic condition (i.e., $|\dot{\theta}(t)| \ll \Omega_{\text{gen}}(t)$), since a large detuning also enlarges Ω_{gen}. We note that the Tanh/Sech and Erf/Gauss pulses provide a "top-hat" transfer profile that selects a well-defined subset of the atom sample (e.g., for velocity selection). Additionally, the Chirp/Square pulse displays ripples in the transfer efficiency that result from low adiabaticity during the resonance crossing.

Focusing our attention on the rapid Tan/Tanh ARP, Fig. 4-2(a) shows the experimental, ensemble-averaged time evolution of the transition probability during this pulse. The sweep parameters were $T_\pi = 10.3t_\pi$, $\delta_{max}/(2\pi) = 15$ MHz, and $\Omega_{arp}/(2\pi) = \Omega_{\text{eff}}/(2\pi) = 86$ kHz. For $\Omega_{\text{eff}} = \Omega_{arp}$, the measured transition probabilities follow the sinusoid predicted by our model (described below). Measurements of transition probability as a function of the center frequency of the sweep, shown in

[1]Technically, the square of this detuning sweep is a rational function.

Fig. 4-2(b), reveal a full width at half maximum of $8\Omega_{\text{eff}}$, which is about five times broader than the corresponding bandwidth of a Raman π pulse. Near resonance, the coherent transfer efficiency is limited to 93% by spontaneous emission. Agreement between the measurements and model helped validate our hardware implementation of Raman ARP.

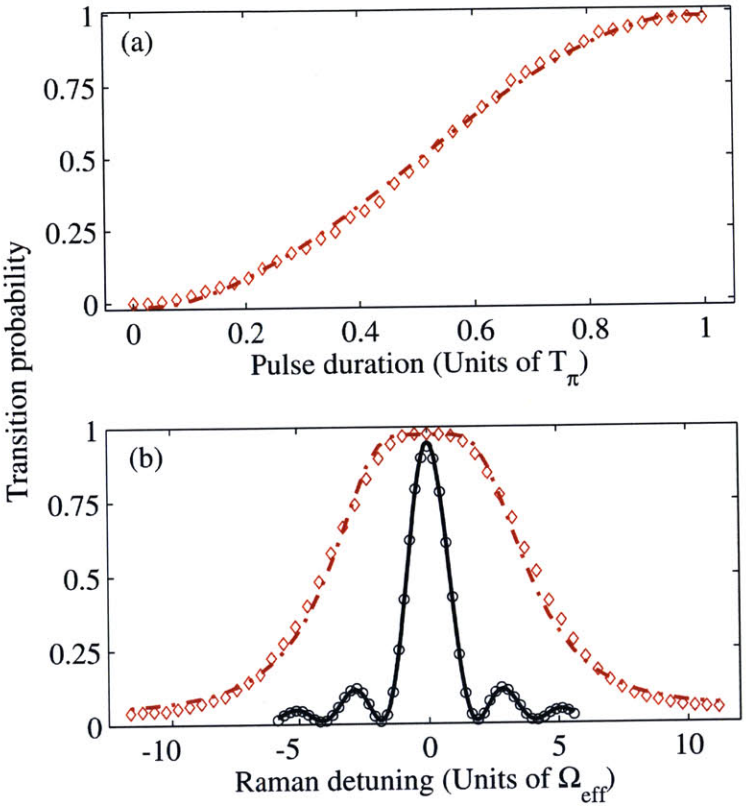

Figure 4-2: Population inversion with the Tan/Tanh ARP pulse. (a) Time evolution of the transition probability during the pulse. The end of the pulse corresponds to $T_\pi = 10.3t_\pi$. (b) With the same T_π value, scanning the Raman ARP (red diamonds) center frequency produces a Raman resonance with linewidth five times broader than that of a Raman π pulse (black circles). Lines are predictions for a two-level system that were scaled and offset to fit the data.

The predictions plotted in Fig. 4-2 were based on a model of a two-level atom. Recall that the dynamics of this system on the Bloch sphere are given by the equation

$$\frac{d\hat{\mathbf{p}}}{dt} = \mathbf{\Omega}_{\text{gen}} \times \hat{\mathbf{p}}. \tag{4.3}$$

With a set of initial conditions for the drive field and the pseudo-spin polarization, the model numerically integrates Eq. (4.3). Numerical integration is necessary because Raman ARP frequency sweeps introduce time-dependencies to $\mathbf{\Omega}_{\text{gen}}$ that generally preclude analytic solutions. The framework can be extended to model interferometer sequences by incorporating a period of free precession about the z-axis of the Bloch sphere during the time between two pulses. Following a pulse sequence, the model reports the atom transition probability in response to a varied parameter (e.g., Raman detuning or phase). The model is also capable of accounting for atom ensemble effects by repeating the calculation for many atoms with randomly assigned positions and velocities, making Ω_{eff} a Gaussian function of position, and averaging over the resulting transition probabilities. In this chapter, predictions from the model do not include ensemble averaging effects.

4.3 Ramsey interferometry with Raman ARP

In addition to inverting population, Raman ARP also serves as an effective beamsplitter in a Ramsey sequence when the sweep is stopped midway, at Raman resonance [63]. Figure 4-3 depicts a Raman ARP Ramsey sequence on the Bloch sphere. The first beamsplitter pulse begins with $\mathbf{\Omega}_{\text{gen}}$ and $\hat{\mathbf{p}}$ initially parallel, as shown in Fig. 4-3(a). The drive field then slowly drags the Bloch vector into the x-y plane (Fig. 4-3(b)), creating a coherent superposition of the clock states. After an interrogation time T, a second beamsplitter starts nearly on resonance to complete the Ramsey sequence. At the beginning of this pulse, $\mathbf{\Omega}_{\text{gen}}$ and $\hat{\mathbf{p}}$ are generally nonparallel, because of discrepancies between the oscillator and atomic resonance frequencies—which the atomic reference is intended to correct. The misalignent leads to the precession shown in Fig. 4-3(c). The drive field then drags $\mathbf{p}_{\|}$to the z-axis (Fig. 4-3(d)), thereby converting the interferometer phase into population difference.

Figure 4-4 shows examples of Ramsey fringes based on Raman $\pi/2$ pulses and Tan/Tanh ARP beamsplitters with $T_\pi = 10t_\pi$ and $26t_\pi$. Two different ARP pulse durations were considered in order to study the benefits of higher adiabaticity. The

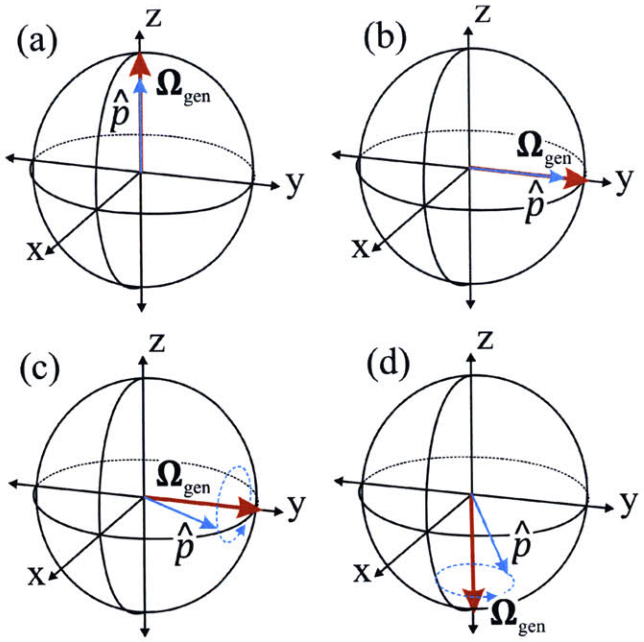

Figure 4-3: Raman ARP Ramsey sequence on the Bloch sphere. (a) Initialized ARP drive field and Bloch vector. (b) Action of the first ARP beamsplitter. (c) State of the system after the dwell time and prior to the second ARP beamsplitter. (d) Action of the second ARP beamsplitter maps the Ramsey phase into population difference.

interrogation time was set to a realistic operating point of $T = 10$ ms. The magnitude of the two-photon Rabi rate was $\Omega_{\text{eff}}/(2\pi) = 73$ kHz, and the Tan/Tanh sweep parameters were $\delta_{max}/(2\pi) = 15$ MHz and $\Omega_{arp}/(2\pi) = 73$ kHz. To reduce discrepancies arising from oscillator drifts and environmental magnetic fields, the three pulse-types were applied sequentially at a given detuning, and measurements were collected at 1.6 Hz over 10 minutes. The measurements were fit to the sinusoidal function for a near-resonant interferogram $P = 1/2 + (A/2)\cos[(\delta - \delta_0)T] + B$, where P was the measured transition probability, and free parameters such as contrast A, background offset B, and Raman detuning offset δ_0, were determined through minimization of the sum of squares of the residuals. For both the Raman $\pi/2$ and $T_\pi = 26t_\pi$ cases, the fit uncertainty in $\delta_0/(2\pi)$ was ± 0.24 Hz, indicating similar short-term stability.

For a device operating in dynamic environments, a short dwell time ensures that an atom cloud experiencing large transverse acceleration remains within the Raman laser beam during the Ramsey interrogation. While the short dwell time reduces per-

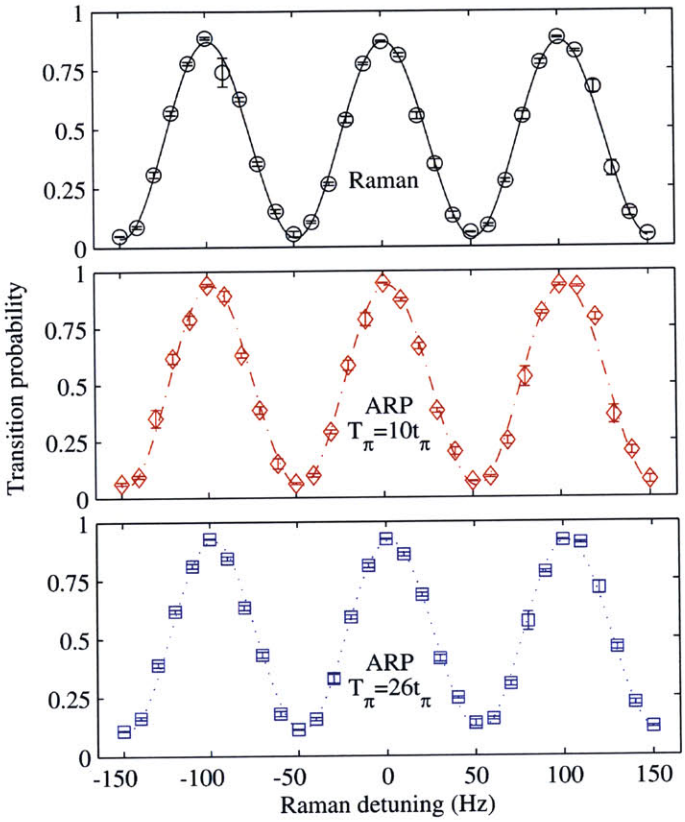

Figure 4-4: Ramsey fringes with an interrogation time of $T = 10$ ms. Lines are best-fit cosine functions, points are measured values, and error bars represent standard error. The condition $\delta = 0$ includes a Zeeman shift of 324 Hz.

shot sensitivity, the fractional frequency of a clock in this configuration still achieves excellent short-term stability. For example, an interrogation time of $T = 10$ ms, coupled with a sampling rate of $f_s = 80$ Hz and a phase signal-to-noise ratio of $\sigma_\Phi^{-1} = 200$, results in a fractional frequency stability of

$$\frac{\sigma_\Phi^{-1}}{\omega_{HFS} T \sqrt{f_s}} \approx 1 \times 10^{-12} \tag{4.4}$$

for an averaging time of 1 s. Moreover, the cloud remains within the $1/e^2$ intensity radius of the Raman beam for transverse accelerations up to 5 g.

4.4 Systematic effects

A cold atom frequency standard based on Ramsey sequences is likely to experience parameter fluctuations during operation outside the laboratory. In dynamic environments, variations in optical power, RF power, and atom cloud position are expected to systematically affect Ramsey interferograms. In this section, we demonstrate how Raman ARP beamsplitters in a Ramsey sequence suppress some of these systematic effects.

4.4.1 Light shifts during a Raman pulse

A Ramsey sequence based on Raman ARP affords an important advantage over Raman $\pi/2$ pulses: light shifts during a pulse leave the interferometer phase unperturbed. Recall that the Ramsey phase is governed by the azimuthal angle between the Bloch vector and drive field prior to the second beamsplitter pulse. The presence of the light shift during ARP moves the center frequency of the sweep off resonance, causing an error in drive field polar angle that leaves the beamsplitter in Fig. 4-3(b) outside the x-y plane. The parallel Bloch vector $\hat{\mathbf{p}}$ also carries this error in polar angle, but the Ramsey phase (i.e., azimuthal angle) remains unperturbed. Polar angle errors, however, do affect interferometer contrast. When the second beamsplitter is initially π rad out of phase with $\hat{\mathbf{p}}$, the light shift reduces the transfer efficiency, causing the

troughs of the interferogram to rise up. For the small light shifts relevant to a practical device, the resulting variations in contrast and background offset have a minor impact on sensitivity, as we will soon show.

To experimentally verify the suppression of light shifts, we tested the sensitivity of three types of Ramsey sequences to δ_{AC}. In particular, we compared Raman $\pi/2$ pulse sequences to Tan/Tanh ARP sequences with T_π durations of $10t_\pi$ and $26t_\pi$, recording contrast A, background offset B, and systematic phase offset Φ for each interferogram. The transition probability P is related to these quantities by the equation $P = 1/2 + (A/2)\cos[\Phi + \varphi] + B$, where φ is the programmed Raman phase shift between the two Ramsey pulses and the Raman detuning is assumed to be 0. We extracted entire interferograms to determine A, B, and Φ simultaneously, which suppressed undesirable cross-coupling effects in the measurement of P. This technique differs from a simpler one in which each measurement of phase is related to a single measurement of transition probability made with $\varphi = \pi/2$ and $\Phi \approx 0$. In that approach, phase measurements are susceptible to variations in A and B since the transition probability varies with these parameters.

For each δ_{AC} setting, the three types of interferometers were measured sequentially, three times over 8 minutes. The δ_{AC} settings were tested in a pseudo-random order. To extract an interferogram, φ was scanned over two fringes in steps of $\pi/4$ rad (to enable averaging, each phase condition was repeated five times, consecutively). We controlled δ_{AC} with the modulation depth of the EOM in the Raman beam path, which adjusted the ratio of the optical powers in each Raman frequency. At each setting of the modulation depth, the overall optical power was adjusted with the tapered amplifier to maintain $\Omega_{\text{eff}}/2\pi = 73$ kHz to within $\pm 2\%$. The light shift was assumed to be the Raman detuning at which population transfer with a standard Raman π pulse was maximized. Following these calibration steps, the oscillator frequency was set to the Zeeman-shifted clock resonance before interferometry commenced. At this frequency, the oscillator was detuned by the light shift during application of the pulse, but resonant with the atoms during the Ramsey dwell period. The short dwell time of $T = 1$ ms suppressed sensitivity to oscillator frequency instabilities and helped

isolate phase shifts associated with pulse dynamics.

Clock phase shifts

Figure 4-5(a) shows the systematic phase offset Φ of each interferometer as a function of δ_{AC}. The Raman-pulse measurements show good agreement with the predictions from our model. Linear fits to the predictions and measurements give a light shift sensitivity of 26 mrad/kHz. The Tan/Tanh ARP interferometers strongly suppress this sensitivity. A closer view of the Raman ARP data, shown in Fig. 4-5(b), reveals an overall linear trend of 0.34 mrad/kHz with localized curvature, neither of which our model predicts. The predictions for $T_\pi = 10t_\pi$ (red dash-dot curve) are restricted to detunings where the sweep is adiabatic enough for the model to produce controlled phase shifts. That the corresponding measured phases at $\delta_{AC}/2\pi = \pm 100$ kHz are not completely randomized may result from ensemble averaging effects.

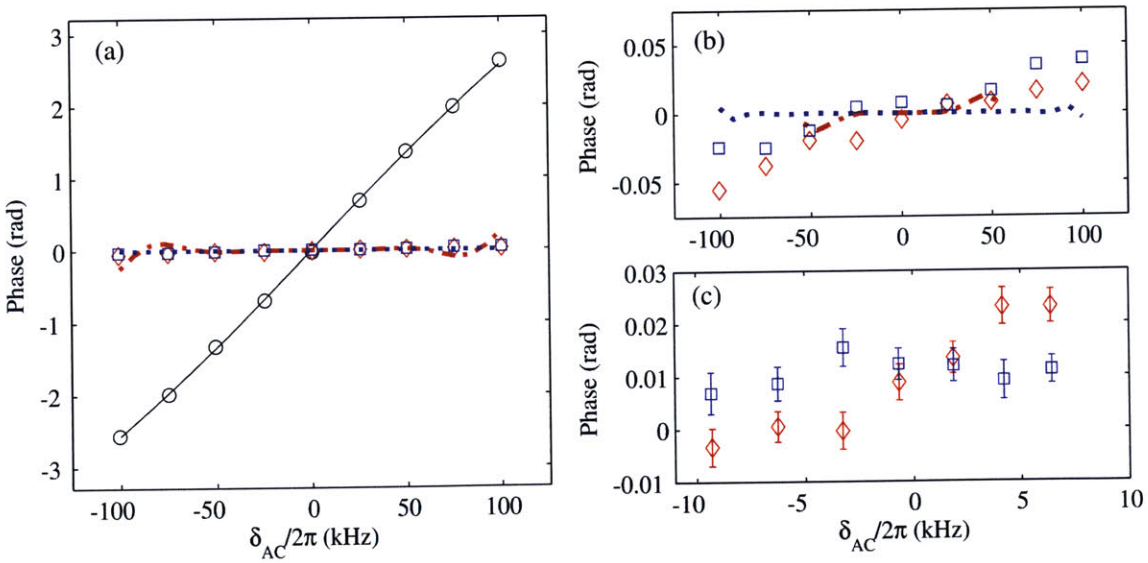

Figure 4-5: Sensitivity of Ramsey phase to differential AC Stark shifts. (a) The Raman pulse case (black circles) was about 75 times more sensitive to δ_{AC} than Tan/Tanh ARP interrogations with $T_\pi = 10t_\pi$ (red diamonds) and $T_\pi = 26t_\pi$ (blue squares). (b) Residual Raman ARP phase variations not predicted by our model. (c) Over a narrower range of δ_{AC} values, standard Raman pulses were roughly 100 times more sensitive to δ_{AC} than Raman ARP with $T_\pi = 26t_\pi$. Error bars represent standard error. All lines are based on an unmodified model for a two-level system.

In practice, the differential Stark shift, with $\Delta \approx -2$ GHz, could reasonably be restricted to $\pm 0.02\Omega_{\text{eff}}$ due to $\sim$1% power fluctuations in the RF signal modulating the EOM; below this bound, the measurement and stabilization of RF power is challenging. We therefore repeated the previous experiment over a narrower detuning range near $\delta_{AC} = 0$. In this version of the experiment, Ω_{eff} was not calibrated from one condition to the next, because the measured variation was just $\pm 2\%$ of the nominal setting. The light shift was calibrated to the modulation depth of the EOM, which was then tracked via real-time RF power measurements. In this manner, the entire experiment was automated and completed in under one hour. The δ_{AC} values were tested in a pseudo-random order and three times over for averaging. Linear fits to the Raman ARP phase offsets (shown in Fig. 4-5(c)) and the Raman phase offsets (not shown) were compared to determine the *relative* sensitivity to δ_{AC}. The ratios of the two ARP slopes to the Raman slope were 0.063 ± 0.008 for the $T_\pi = 10t_\pi$ case and 0.005 ± 0.008 for the $T_\pi = 26t_\pi$ case. Since drifts in δ_{AC} on the order of $\pm 0.02\Omega_{\text{eff}}$ are expected in a practical device, the measured sensitivity of the Raman $\pi/2$ sequence to δ_{AC} implies that the phase will vary by 26 mrad. To put this result into context, consider the case where δ_{AC} is a white noise process. The fractional frequency stability for the example presented in Eq. (4.4) then becomes 5×10^{-12} after 1 s of averaging, because the phase signal-to-noise ratio drops to $\sigma_\Phi^{-1} = 40$. By comparison, the Tan/Tanh ARP interferometer, with $T_\pi = 26t_\pi$, would suppress the light shift to a level where atom shot-noise would be a larger noise source (assuming 1×10^6 atoms).

Contrast and background variation

The extraction of full interferograms also enabled the study of contrast and background offset variations in response to the light shift. These variations are particularly important when phase shifts are estimated from single measurements of transition probability, made near $\varphi = \pi/2$. In this case, variations in background offset can lead to large apparent phase shifts. Small changes in contrast, however, are inherently tolerable near $\varphi = \pi/2$, since they merely scale existing errors in transition

probability. Figure 4-6(a) shows the contrast response to δ_{AC} for the three pulses considered above. In each case, the maximum measured contrast serves to normalize the associated predictions. This normalization qualitatively accounts for spontaneous emission losses during Tan/Tanh sweeps and yields good agreement with measurements when the sweep is adiabatic. For Raman pulses, normalization approximately accounts for dephasing due to inhomogeneities in Ω_{eff} and δ_{AC} (spontaneous emission makes a minor contribution). Since these inhomogeneities scale with Ω_{eff} and δ_{AC} and are coupled, it is reasonable that the model overestimates the contrast away from resonance. For small differential Stark shifts of $\pm 0.02\Omega_{\text{eff}}$ (within the bounds of reasonable RF power control), the contrast is expected to vary by about 0.13% and should scale phase deviations from $\varphi = \pm\pi/2$ by this fraction.

Variations in background offsets follow the unmodified predictions of our model, as shown in Fig. 4-6(b). The rise in Raman ARP offsets in response to detuning indicates that the troughs of the interferograms are pulled up due to impaired transfer during the second Ramsey pulse. For Stark shifts of $\pm 0.02\Omega_{\text{eff}}$, the offset is expected to vary by about 0.07%, leading to <2 mrad error in phase and a fractional frequency stability at 1 s of 3×10^{-13}—a minor contribution to frequency instability (see Eq. (4.4)). Sensitivity to background offsets can be further suppressed by sequentially measuring transition probability near $\varphi = \pm\pi/2$ and estimating the phase error from the difference of consecutive measurements. Slow background variations are then immaterial since they produce the same differential phase.

4.4.2 Laser beam intensity profile

Raman ARP also achieves a high degree of robustness against optical intensity variations. Since $\vec{\mathbf{p}}_{\parallel}$ is unaffected by Ω_{eff} in the adiabatic limit, Ramsey sequences based on Raman ARP maintain high contrast despite fluctuations in optical power or poor beam quality. An important cause of power variation, particularly on dynamic and mobile platforms, is motion of the atom cloud along the beam radius. During a $T = 10$-ms interrogation, for instance, a cloud accelerating transverse to the beam axis at 3.5 g traverses the 1σ radius of a Gaussian beam with a 3.5-mm $1/e^2$ intensity

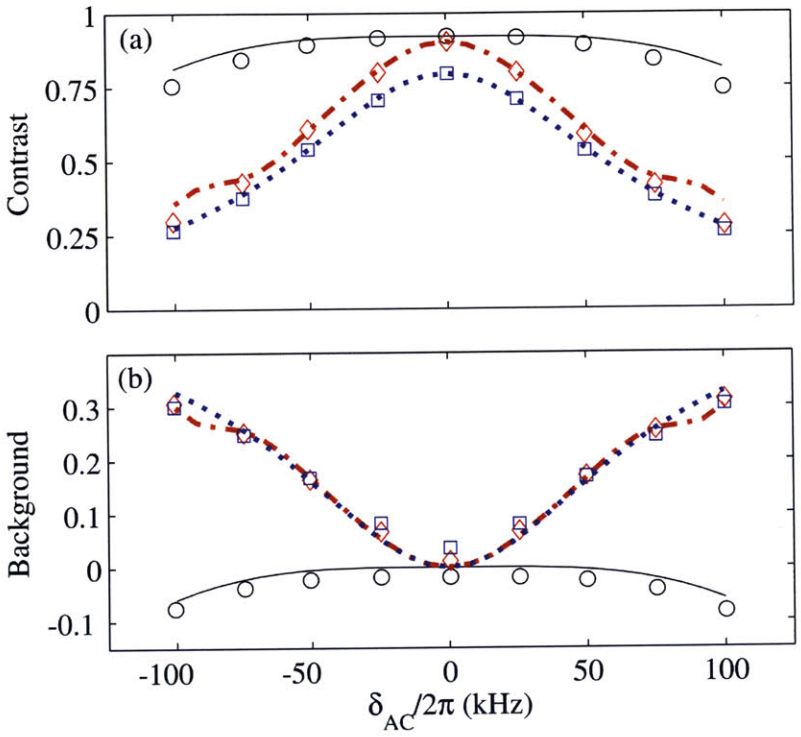

Figure 4-6: Sensitivity of (a) contrast and (b) background offset to differential AC Stark shifts for Ramsey sequences based on Raman (black circles), Tan/Tanh ARP with $T_\pi = 10t_\pi$ (red diamonds), and Tan/Tanh ARP with $T_\pi = 26t_\pi$ (blue squares) beamsplitter pulses. Lines represent predictions from a model.

radius. Over this distance, the beam profile introduces substantial position-dependent changes to the gradient and average of the optical intensity experienced by the cloud. A practical timing reference might measure such accelerations using an inertial sensor. With a $T = 10$ ms interrogation time, a low-performance accelerometer with 10 mg resolution can determine the radial position of the cloud to within 5 μm. Such accurate position information, along with knowledge of the beam profile, enables compensation for changes in the average intensity via modification of optical power or pulse duration.

Optical intensity gradients, however, are more challenging to correct in real-time. An alternative approach is to provide uniform intensity with a "flat-top" beam. Unfortunately, uniform intensity only occurs in a small region along the propagation axis of this beam, and the resulting optical wavefronts are distorted. Being limited to use of a Gaussian beam, we tested the effect of the intensity gradient on interferometer contrast by displacing the Raman beam relative to the atom cloud and using pulse duration to compensate for changes in the average intensity. Specifically, we corrected pulse durations so that at each position $t_\pi = \pi/\Omega_{\text{eff}}$. During real transverse accelerations, the first Ramsey pulse occurs with the cloud near beam center, while the second occurs with the cloud closer to the beam edge, where the gradients are larger. In our experiments, conditions were more adverse: the Raman beam position was kept constant for a given experimental condition, meaning both pulses imposed deleterious intensity gradients.

To control the radial position of the cloud within the beam, the Raman beam collimator was mounted to a linear translation stage. Prior to the experiment, the beam was centered on the cloud by maximizing Ω_{eff} with a fixed optical intensity, and then minimizing decoherence during Rabi flopping experiments. Ω_{eff} and δ_{AC} were extracted at each position from measurements of the Raman π pulse resonance as a function of detuning (e.g., Fig. 4-2(b)), and the differential AC Stark shift was reduced to $|\delta_{AC}| \leq 0.02\Omega_{\text{eff}}$. The Tan/Tanh sweeps were adjusted to maintain $\Omega_{arp} = \Omega_{\text{eff}}$ so that in units of t_π, the frequency profile remained the same. Interferometry was then carried out using Raman $\pi/2$ pulses and ARP pulses with $T_\pi = 10t_\pi$ and $T_\pi =$

$26t_\pi$. A realistic interrogation time of $T = 10$ ms captured contrast loss associated with cloud expansion.

Figure 4-7 shows that over a 1σ range of the beam radius (2σ corresponds to the $1/e^2$ radius), the fractional variation in contrast is 15 times smaller for ARP sweeps with $T_\pi = 26t_\pi$ than for resonant Raman pulses. While the contrast of the $T_\pi = 10t_\pi$ ARP interferometer still trends with beam position, the more adiabatic $T_\pi = 26t_\pi$ interferometer exhibits just a 1.5% contrast variation out to half the $1/e^2$ intensity radius. This robustness should improve the stability of clock interferometers operating in dynamic environments without the need for larger beam diameters and higher optical power. Also problematic is the motion of an atom cloud along the beam axis, because it introduces Doppler shifts that create frequency instability. Methods for overcoming the Doppler instability are proposed in Sec. 4.5.

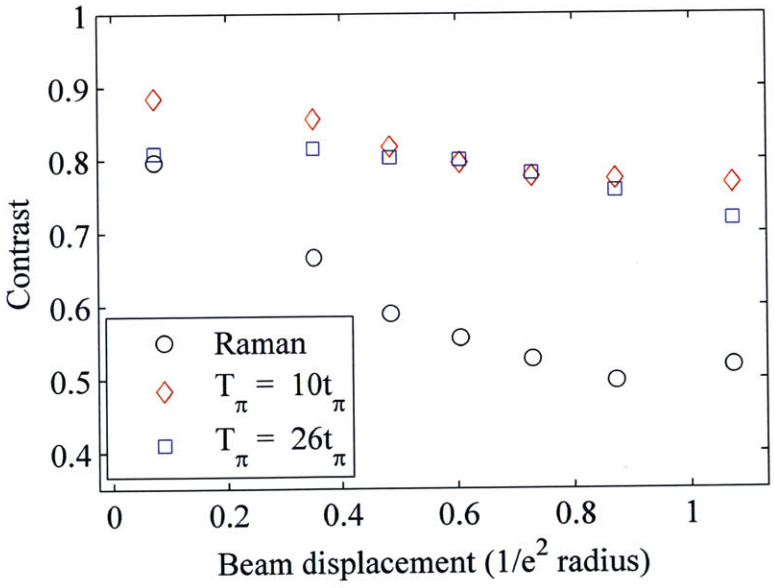

Figure 4-7: Ramsey contrast variation due to laser beam intensity gradients. Beamsplitters were based on Raman pulses (black circles), Tan/Tanh ARP with $T_\pi = 10t_\pi$ (red diamonds), and Tan/Tanh ARP with $T_\pi = 26t_\pi$ (blue squares). Over the 1σ, or $e^{-1/2}$, intensity radius, the fractional variation in contrast was 15 times larger for Raman $\pi/2$ pulses than for Tan/Tanh ARP with $T_\pi = 26t_\pi$.

4.4.3 Coupling of light shifts and intensity variation

Sensitivity of the Ramsey phase to optical intensity, coupled with differential AC Stark shifts, was studied using Bloch sphere simulations. The intensity was the same for both Ramsey pulses and was related to atom displacement by assuming a Gaussian spatial intensity profile for the laser beam. Tan/Tanh and Rational/Square ARP beamsplitters were considered, along with standard Raman $\pi/2$ pulses. As shown in Fig. 4-8(a), the Tan/Tanh pulse provides the strongest suppression of systematic Ramsey phase shifts (<1 mrad) for cloud displacements covering 1σ of the Raman beam $1/e^2$ intensity radius, coupled with differential AC Stark shifts approaching 10% of the two-photon Rabi rate. For consistency, the ARP parameters were matched to those used experimentally: $T_\pi = 26t_\pi$, $\delta_{max} = 2\pi \times 15$ MHz, $\Omega_{\text{eff}} = \Omega_{arp} = 2\pi \times 71$ kHz, and $\beta = 7.5$. Pulse durations were constant throughout the simulation, and t_π was defined with respect to the two-photon Rabi rate at peak intensity.

The superior performance of Tan/Tanh as compared to Rational/Square is surprising given the general similarities between these frequency sweeps. Upon closer examination, however, the Tan/Tanh pulse displays distinguishing qualities that deserve mention. First, a tangent frequency sweep *without intensity modulation* produces a Bloch vector trajectory that follows a great circle on the Bloch sphere, as originally shown by Baum, Tycko, and Pines [65]. These authors further showed that tangent sweeps with *finite* adiabaticity also generate Bloch vector trajectories along a great circle when T_π and Ω_{arp} are appropriately modified. An ARP beamsplitter benefits from this great circle trajectory, since it results in a well-defined Ramsey phase. The addition of a hyperbolic tangent intensity modulation allows the Tan/Tanh ARP to mimic the behavior of the infinitely adiabatic tangent sweep from [65], but without infinite detuning or pulse duration. Conversely, an ARP beamsplitter that causes the Bloch vector to trace tiny precession rings creates intensity- and detuning-dependent shifts in the Ramsey phase. The smooth curves in Fig. 4-8(b) provide examples of Bloch sphere trajectories of a Bloch vector subjected to a Tan/Tanh sweep (i.e., with intensity modulation). Importantly, a detuning error results in minor phase variation

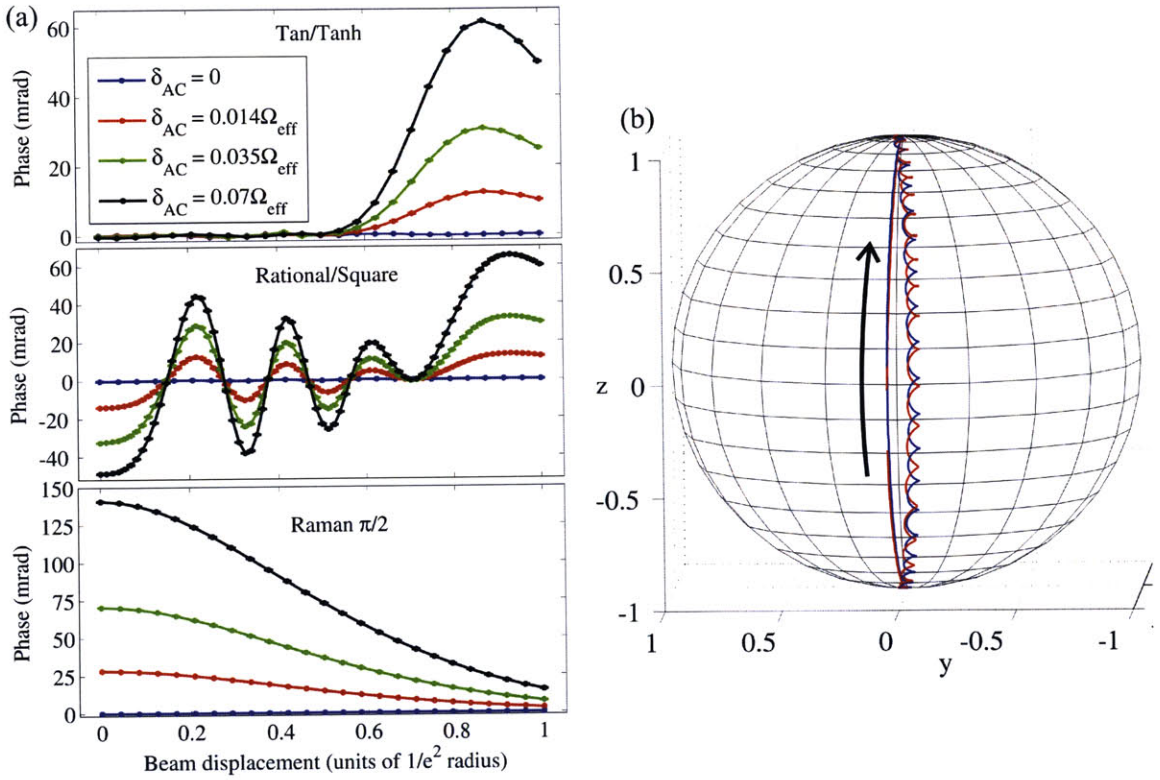

Figure 4-8: (a) Simulation of Ramsey phase variation due to coupling of Stark shifts and displacement of a Gaussian laser beam. The Tan/Tanh pulse suppresses phase shifts to <1 mrad for atom cloud displacements exceeding 1σ of the Gaussian beam intensity radius, and for AC Stark shifts up to $\delta_{AC} = 0.07\Omega_{\text{eff}}$. These simulations neglect ensemble averaging effects. (b) Bloch sphere trajectories of a Bloch vector subjected to Tan/Tanh (smooth curves) and Rational/Square (rotary curves) pulses. Examples include resonant (blue) and $\delta_{AC} = 0.2\Omega_{\text{eff}}$ (red) cases. Since the trajectories for Tan/Tanh beamsplitters nearly follow a great circle, they produce a well-defined Ramsey phase.

($\delta_{AC} = 0.2\Omega_{\text{eff}}$ in this example), especially when compared to the variations produced by the Rational/Square ARP (see rotary curves). One would expect other ARPs, including Rational/Square, to perform better with longer pulse durations and correspondingly higher adiabaticity. For reasons mentioned in Sec. 4.2, we prefer the shortest possible ARP.

4.4.4 Sweep parameters

Parameter fluctuations in practical frequency sweeps will introduce instabilities to a Raman ARP-based clock. Variations in Ω_{eff} typically arise from drifts in optical power, polarization, and RF power, whereas perturbations to the sweep parameters T_π, Ω_{arp}, and δ_{max} may result from reproducibility-issues associated with broad frequency sweeps in RF systems. To provide a robust timing reference, a Raman ARP Ramsey sequence must withstand reasonable variations in these parameters. Our model predicted phase deviations of <1 mrad and contrast variations consistent with zero in response to $\pm 10\%$ changes in the parameters listed above. We experimentally tested the sensitivity by extracting ARP interferograms with T = 1-ms interrogation times, while deliberately adjusting the sweep parameters over $\pm 10\%$ of a nominal value. For each parameter, we acquired Tan/Tanh ARP interferograms with $T_\pi = 10t_\pi$ and $T_\pi = 26t_\pi$. The phase responses plotted in Fig. 4-9 represent weighted averages, while error bars signify standard errors. Nominal settings were $T_\pi = 10t_\pi$ (red diamonds) or $T_\pi = 26t_\pi$ (blue squares), $\delta_{max}/(2\pi) = 15$ MHz, $\Omega_{arp}/(2\pi) = 73$ kHz, and $\Omega_{\text{eff}}/(2\pi) = 73$ kHz. Over the ~1000 s averaging times relevant to these experiments, second-order Zeeman shifts resulting from the large 870 mG bias field limited the long-term stability. At about 4×10^{-11}, the fractional frequency uncertainty of our open-loop clock was consistent with the <3 mrad phase uncertainty seen in this experiment, given an interrogation time of $T = 1$ ms. In the next section, we discuss improvements in stability resulting from a reduction in bias field strength.

Due to spontaneous emission, the contrast responded linearly to changes in T_π and Ω_{eff}. The $T_\pi = 26t_\pi$ and $10t_\pi$ cases exhibited maximum contrast deviations of 3.8% and 1.8%, respectively. The maximum respective deviations in background

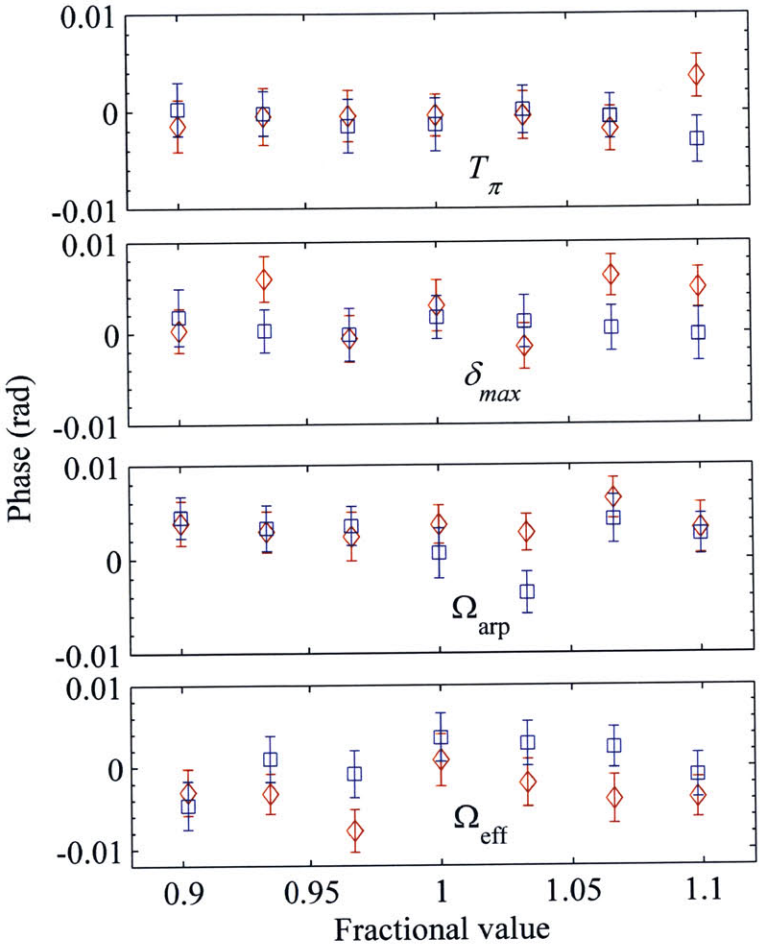

Figure 4-9: Phase sensitivity of Tan/Tanh ARP Ramsey sequence to 10% variations in parameters defining the ARP frequency sweep. Nominal settings: $T_\pi = 10t_\pi$ (red diamonds) or $T_\pi = 26t_\pi$ (blue squares), $\delta_{max}/(2\pi) = 15$ MHz, $\Omega_{arp}/(2\pi) = 73$ kHz, and $\Omega_{\text{eff}}/(2\pi) = 73$ kHz. The residual instability in these measurements was driven largely by magnetic field fluctuation.

offset were 0.7% and 0.4%. This sensitivity is unlikely to limit a deployed sensor, in which T_π and Ω_{eff} will be controlled to 1% or better. With this stricter bound on pulse parameters, the resulting 0.07% instability in offset yields a fractional frequency stability at 1 s of 3×10^{-13}. These effects will be further suppressed by averaging of sequential phase measurements at $\varphi = \pm\pi/2$.

By varying the single-photon Raman laser detuning, we confirmed that spontaneous emission reached a broad minimum between -2 and -3.5 GHz. The magnitude of the detuning was bounded by the hyperfine splitting frequency to enable the cancellation of light shifts through correct choice of optical intensity ratio between the Raman frequency components.

4.5 Stability assessment

To assess the stability of our atomic reference, we computed the Allan deviations of Ramsey frequency measurements based on Tan/Tanh ARP pulses with $T_\pi = 26t_\pi$, as well as Raman $\pi/2$ pulses and microwave $\pi/2$ pulses. For these measurements, the bias field was reduced to 87 mG to suppress contributions from environmental magnetic fields. Since the clock state Zeeman shift has a quadratic dependence on field strength, small drifts in the magnetic environment, acting in conjunction with a weak bias field, produce smaller systematic phase shifts (i.e., $\Delta f \propto B\Delta B$). Phase deviations were related to frequency shifts through precise knowledge of the interrogation time, which was set to $T = 16.667$ ms to sychronize with (and thereby suppress) environmental electromagnetic noise at 60 Hz. Contrast values for the ARP and microwave interferometers were not noticeably changed by the increase in interrogation time from 10 ms to 16.667 ms. The three pulse-types were applied sequentially with a data-rate of 1.6 Hz. However, the effective data-rate for a particular pulse-type was 0.13 Hz, because frequency measurements were based on interferogram fits. Interferograms were extracted from four consecutive measurements with phase shifts of $\varphi = \{-3\pi/4, -\pi/4, \pi/4, 3\pi/4\}$. This scheme allowed simultaneous measurements of interferometer contrast and background offset. The RF signal generator,

provided with a 10 MHz reference from a separate Cs beam clock (Symmetricom 5071A), produced a stable signal that enabled examination of the long-term stability of our atomic reference. The fractional frequency stability of the Cs beam reference is $\leq 5 \times 10^{-12}/\sqrt{\tau}$.

The Allan deviations, plotted in Fig. 4-10(a), indicate that the fractional frequency uncertainty for all interferometers was limited to $\sim 3.5 \times 10^{-12}$ around 2500 s. The similarities in Allan deviations across all pulse-types suggest that light shifts were not a limiting factor in this experiment. Subsequent Ramsey spectroscopy with

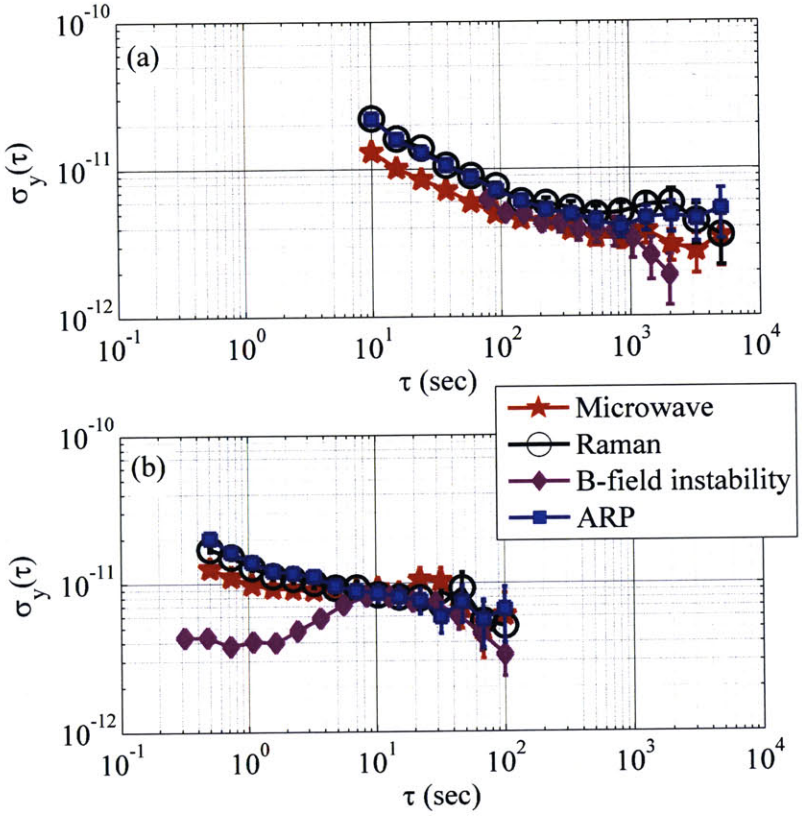

Figure 4-10: Allan deviations of fractional frequency measurements characterizing the stability of the three Ramsey sequences. (a) Frequency measurements were acquired with three interleaved pulse-types. Light shifts were not the dominant systematic effect. Magnetic field instability limited the fractional frequency uncertainty to $\sim 3.5 \times 10^{-12}$. (b) A stability measurement with higher data-rate (5 Hz) improved the short-term stability of all pulse-types to $\sim 1.5 \times 10^{-11}$ for an averaging time $\tau = 1$ s. Magnetic fields remained the limiting source of instability for $\tau > 5$ s.

$m_F = 1$ states, which carry a first-order sensitivity to the Zeeman shift of 700 kHz/G,

revealed magnetic field instability to be the dominant noise source. In that measurement, Ramsey phase jitter was attributed to magnetic field fluctuations, which were then used to predict the instability in the clock resonance (see purple diamonds in Fig. 4-10(a)). At short averaging times from $\tau = 10$ to 100 s, the slopes of the Allan deviations indicate a white noise process driven largely by the low effective data-rate. As shown in Fig. 4-10(b), frequency measurements acquired at 5 Hz—a 38-fold increase in data-rate—improved the short-term stability to $\sim 1.5 \times 10^{-11}$ at $\tau = 1$ s, though white noise was no longer the limiting process. Beyond $\tau = 5$ s, magnetic field instability once again became the limiting systematic effect. We note that frequency measurements at the higher data-rate were based on single shots acquired near quadrature phase and that the pulse-types were not interleaved. These results are comparable to a recent timekeeping demonstration using CPT with optical fields, which achieved a fractional frequency uncertainty (also limited by magnetic field instabilities) of 2×10^{-12} at 1000 s [33].

An important source of frequency instability not addressed in this work is atom motion along the Raman beam axis, which Doppler shifts the clock resonance. The Doppler shift could ultimately be measured with a low-cost inertial sensor and compensated by adjusting the Raman detuning. An accelerometer with 10 mg resolution determines the Doppler-induced phase shift to within 1 mrad, limiting the short-term stability to 2×10^{-13} if one assumes an averaging time of 1 s, a sampling rate of 80 Hz, and a Ramsey interrogation time of 10 ms. Alternatively, one could discern Doppler shifts that are stable over consecutive measurements by cycling between forward- and backward-propagating Raman beams. This technique relies on the fact that reversal of beam propagation changes the sign of the Doppler shift but not the clock frequency.

4.6 Summary

We have presented frequency-swept Raman ARP as a tool for robust Ramsey interrogation. With a sufficiently adiabatic sweep, we have produced Raman ARP Ramsey fringes that agree well with those of corresponding sequences based on Raman $\pi/2$

pulses. Raman ARP Ramsey sequences strongly suppress phase sensitivity to light shifts during the pulse. For the small differential AC Stark shifts expected in a practical timing reference ($|\delta_{AC}| \leq 0.02\Omega_{\text{eff}}$), the phase sensitivity is reduced by about two orders of magnitude, effectively eliminating light shift contributions to short-term noise and improving the prospects for long-term stability with an optical Ramsey interrogation. Our approach also reduces the sensitivity of Ramsey fringe contrast to Gaussian laser beam intensity gradients, which is a critical attribute for cold atom clocks operating in dynamic environments. Potential phase sensitivity to the frequency sweep parameters, if present, is below the resolution limits of our system. Single pulse experiments indicate that the Tan/Tanh ARP characterized by Eq. (4.1) is faithfully reproduced by our RF electronics and electro-optics. Our results suggest that Ramsey interferometry based on Raman ARP provides a promising timekeeping method for primary references operating in dynamic environments. Future work will focus on increasing the data-rate while maintaining signal-to-noise ratio, adding magnetic shields to suppress ambient field fluctuations, and using our atomic reference to actively stabilize a 10 MHz oscillator.

Chapter 5

Large area interferometry with Raman adiabatic rapid passage

In this chapter, we present atom interferometry with large momentum transfer (LMT) atom optics based on frequency-swept adiabatic rapid passage (ARP). LMT is particularly useful for inertial sensing applications, since it increases the interferometer sensitivity without sacrificing bandwidth. In our demonstration of atom interferometry with LMT atom optics, we use Raman ARP to achieve high-contrast interferograms with interrogation times that are pertinent to fast data-rate operation. ARP atom optics are beneficial because they offer wide velocity acceptances, allowing one to work with the entire laser cooled cloud and forgo evaporative cooling or velocity selection steps that inherently lower atom number and data-rate. Interestingly, these atom optics have provided momentum separations of up to $30\hbar k$ between diffracting wavepackets in an acceleration-sensitive interferometer—a record for stimulated Raman transitions. We have verified scale factor enhancement and characterized decoherence as a function of momentum separation, interferometer dwell time, and ARP sweep parameters. We also demonstrate symmetric $4\hbar k$ beamsplitters and mirrors that may be useful for long baseline atom interferometry in space-based interferometers.

5.1 Motivation

Highly sensitive light pulse atom interferometry (LPAI) may be an enabling technology for next-generation inertial navigators [109, 51], gravitational wave detectors [110], and tests of the equivalence principle [111]. However, inertially sensitive LPAIs are presently limited by atom beamsplitters and mirrors that create small momentum separations (two photon recoil momenta) between diffracting wavepackets. The sensitivity of these interferometers typically increases with the effective area enclosed by the interfering wavepackets [84]. Since this area is proportional to the wavepacket momentum separation, sensitivity can be enhanced using atom optics that generate large momentum transfer (LMT). LMT has been demonstrated with multiphoton atomic transitions and sequential application of $2\hbar k$ atom optics. In particular, previous demonstrations of atom interferometry with LMT have used sequential application of stimulated Raman transitions [77, 112], Raman composite pulses [101], and stimulated Raman adiabatic rapid passage pulses [75], as well as application of multiphoton-Bragg transitions [78, 113], and Bloch oscillations in an optical lattice [79, 114].

In most of these demonstrations, cold atoms from a magneto-optical trap (MOT) were either evaporatively cooled or velocity selected—both of which typically discard >90% of the original atom sample. Reduced atom number is detrimental to atom shot-noise limited measurement uncertainty and to operation at fast data-rates. A slower data-rate results because, following every measurement cycle, the steady-state atom number in the MOT must be recovered primarily from room-temperature atoms. When cold atoms are recaptured, however, the number of atoms per interrogation that must be loaded from the room-temperature background vapor is reduced, and the data-rate can be increased to >100 Hz [47]. High data-rates are crucial for atom interferometric measurements of dynamic signals, such as rapidly varying accelerations and rotations of moving platforms, as well as strains from high frequency ($\sim$10 Hz) gravitational waves [110, 79]. The fastest data-rates with evaporative cooling have been limited to $\leq$1.3 Hz [91]; velocity selection at high data-rates requires the

added complexity of a 2D MOT to maintain atom number [95].

In this work, we demonstrate cold atom interferometers with high contrast and up to $30\hbar k$ beamsplitter pulses, while forgoing evaporative cooling and velocity selection. The atom beamsplitters are implemented in an acceleration-sensitive interferometer and use a combination of stimulated Raman transitions and frequency-swept adiabatic rapid passage (ARP). These atom optics will enable large area atom interferometry with improved counting statistics, fast data-rates, and reduced constraints on atom temperature. Our approach to ARP fundamentally and practically differs from the demonstration of STIRAP in reference [75], as will be discussed below.

To illustrate the utility of LMT atom interferometry with an entire laser-cooled atom cloud, consider that an atom shot-noise limited accelerometer, operating with 10^7 atoms, $T = 5$ ms, and efficient $22\hbar k$ beamsplitters, resolves $\sim$10-ng variations in acceleration per shot. At data-rates approaching 100 Hz, such a device would provide n$g/\sqrt{\text{Hz}}$ sensitivity while maintaining sufficient compactness and bandwidth for precision inertial sensing. By comparison, the nominal LPAI with $2\hbar k$ beamsplitters would need a longer dwell time of $T = 25$ ms to achieve the same sensitivity, resulting in a factor-of-5 reduction in data-rate and bandwidth. Combining LMT with higher atom number and data-rates may also prove useful in scientific applications. For example, increasing the dwell time in the previous example to $\sim$100 ms would produce sensitivities comparable to those achieved using Bose Einstein condensates (BECs) in large experimental systems with interrogation times of $\sim$1 s.

5.2 Atom interferometry with large momentum transfer atom optics

Our demonstration of LPAI with LMT atom optics is carried out in a Mach-Zehnder interferometer, depicted in Fig. 5-1. The interferometer is composed of a beamsplitter pulse sequence that coherently divides the atom wavepacket, a mirror sequence that brings the wavepackets back together, and a second beamsplitter sequence that

overlaps the wavepackets to create interference. The first ($\pi/2$), middle (π), and final ($\pi/2$) pulses drive Raman transitions that produce the nominal $2\hbar k$ interferometer discussed in Secs. 2.2.2 and 2.2.3. Achieving higher momentum separations requires "augmentation" pulses with effective wave vectors $\mathbf{k}_{\text{eff}}$ directed as shown by the vertical arrows in Fig. 5-1. These augmentation pulses must invert population while maintaining atomic coherence. In the absence of gravity gradients, the pulse sequence in Fig. 5-1 produces a relative phase between the interferometer arms given by the equation [77]

$$\Delta\phi = \mathbf{k}_{\text{eff}} \cdot \mathbf{a} \left[(2N+1)T^2 - 2N(N+1)T\tau_{lmt} \right], \tag{5.1}$$

where $\mathbf{a}$ is an acceleration, T is the dwell time, and augmentation pulses in the beamsplitter sequence are numbered 1 to N and separated by time τ_{lmt}. Relative to the nominal $2\hbar k$ interferometer, the phase shift per unit acceleration—or scale factor—is amplified by a factor of approximately $2N+1$ for a fixed T.

The LMT atom optics are created by sequentially driving stimulated Raman transitions with physically separated Raman frequencies (see Sec. 3.5.2 for implementation details). LMT beamsplitters, for example, apply a Raman $\pi/2$ pulse followed by N augmentation pulses, while the LMT mirror employs $2N$ augmentation pulses with a Raman π pulse situated in the middle. Each of the N augmentation pulse in the beamsplitter increases the momentum separation between wavepackets by $4\hbar k$, resulting in a maximum momentum splitting of $(4N+2)\hbar k$. This momentum splitting is achieved using LMT atom optics that reverse the effective wave vector from one Raman pulse to the next. In Fig. 5-2, the case of parallel $\mathbf{k}_{\text{eff}}$ shows two Raman π pulses, with the same wave vector orientation, acting sequentially on an initially unmoving atom in state $|3,0\rangle$, where the second state label denotes atomic momentum. The first pulse transfers the atom to $|4,\hbar\mathbf{k}_{\text{eff}}\rangle$, because an atom in $F=3$ absorbs ω_1 and is stimulated to emit ω_2 (see energy level diagram in Fig. 5-2). The second pulse returns the atom to $|3,0\rangle$ because a $F=4$ atom absorbs ω_2 and is stimulated to emit ω_1. If the orientation of the photons in the second pulse is flipped, as in the reversed

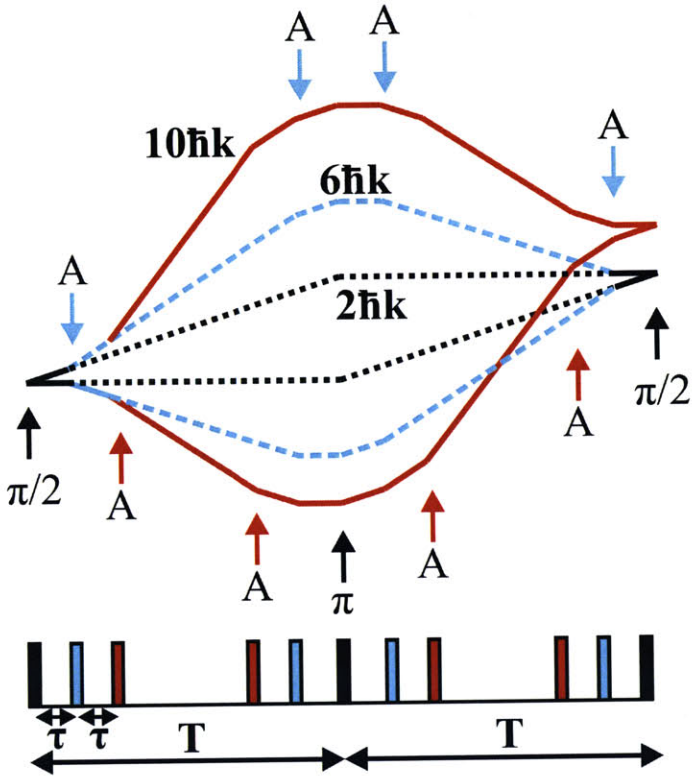

Figure 5-1: Diagram of pulse timings and wavepacket trajectories for Mach-Zehnder interferometers with $2\hbar k$, $6\hbar k$, and $10\hbar k$ atom optics. Augmentation pulses (A) increase the momentum separation between diffracting wavepackets and are either Raman π, ARP, or composite pulses in this work. The nominal $2\hbar k$ interferometer (black) is composed of a $\pi/2$-π-$\pi/2$ sequence of Raman pulses.

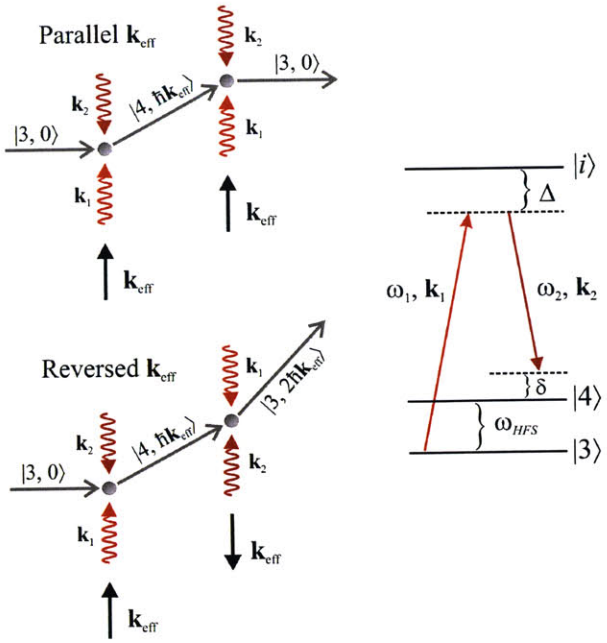

Figure 5-2: Raman effective wave vector reversal for large momentum transfer atom optics. When two atom optics with the same $\mathbf{k}_{\text{eff}}$ orientation are applied, momentum transfer from the first pulse is canceled by the second pulse. The photon recoil momenta add when the $\mathbf{k}_{\text{eff}}$ orientation is reversed for the second pulse.

$\mathbf{k}_{\text{eff}}$ case in Fig. 5-2, the second momentum kick increases the atomic velocity, resulting in an atom in state $|3, 2\hbar\mathbf{k}_{\text{eff}}\rangle$. This pulse sequence produces a $6\hbar k$ LMT atom optic in our interferometers and can be extended, as shown in Fig. 5-1, to achieve even higher wavepacket momentum separations. Importantly, the Raman resonance condition for the second pulse is Doppler-shifted in the case of reversed $\mathbf{k}_{\text{eff}}$, since the Raman transition occurs in an atom with a lower ground state velocity of $2\hbar\mathbf{k}_{\text{eff}}$. As a general consequence of these photon recoils, the resonance conditions for the upper and lower interferometer arms separate during the j^{th} beamsplitter augmentation pulse by $4j\omega_r$, where $\omega_r/(2\pi) = 8.26$ kHz is the ^{133}Cs two-photon recoil frequency shift. For a $10\hbar k$ (N=2) interferometer, for example, the upper and lower wavepacket resonances separate by up to 66 kHz. Simultaneously addressing both interferometer arms thus requires broadband atom optics that tolerate substantial detuning offsets.

5.3 Augmentation pulses

Since large area interferometers require a minimum of four additional laser pulses, they are susceptible to decoherence induced by spontaneous emission, transfer inefficiency, and phase dispersion—all of which lower contrast and hence signal-to-noise ratio (SNR). To improve coherence during an LMT interferometer, we use broadband Raman augmentation pulses based on frequency-swept ARP or composite pulses. In direct analogy to ARP methods from NMR, Raman ARP coherently inverts population in an effective two-level system by slowly sweeping the Raman detuning δ through resonance [59]. Composite pulses, on the other hand, often invert population using resonant, square pulses with discrete Raman phase shifts [58]. In Fig. 5-3, the simulated bandwidths of the ARPs and composite pulses we considered are compared to the significantly narrower bandwidth of a standard Raman π pulse. The sweep parameters were $\Omega_{\text{eff}}/(2\pi) = \Omega_{arp}/(2\pi) = 200$ kHz, $\delta_{max}/(2\pi) = 15$ MHz, and $\beta = 7.5$ Wider bandwidths allow these pulses to improve transfer efficiency with a hot atom

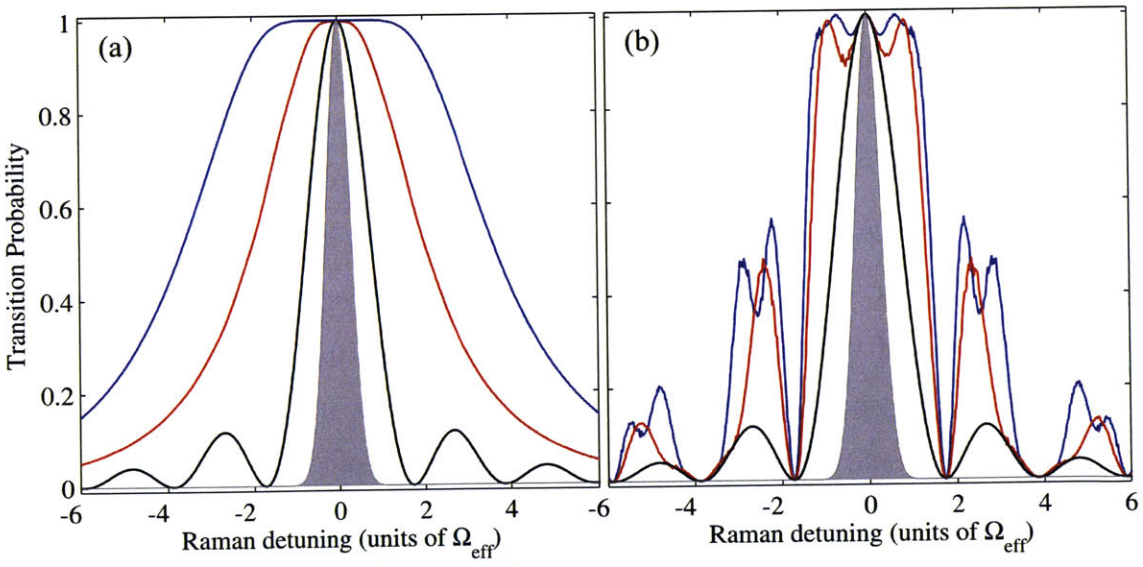

Figure 5-3: Velocity acceptances of ARP and composite Raman pulses. (a) Tan/Tanh transfer efficiency for a wide range of detuning offsets. $T_\pi = 10t_\pi$ (blue) and $T_\pi = 3t_\pi$ (red) cases are compared with Raman π pulses (black), as well as the velocity distribution of a 9-μK cloud (filled grey). (b) Transfer efficiency for WALTZ (blue) and MLEV (red) composite pulses (see Sec. 5.3.2 for details).

cloud (see atom velocity distribution (grey) in Fig. 5-3), though at the expense of increased spontaneous emission and, in some cases, additional dephasing. The rest of this section further discusses the use of composite and ARP Raman pulses in LMT atom interferometry.

5.3.1 ARP augmentation

A number of combined intensity and frequency modulations are known to provide efficient adiabatic population inversion. We selected fast ARPs in order to suppress decoherence and contributions to interferometer phase from finite pulse durations. In particular, we focused on the Tan/Tanh ARP described in Secs. 2.3 and 4.2, and in references [65, 67, 86]. We reiterate that the time-dependent detuning for this ARP is $\delta(t) = \Omega_{arp} \tan\left[\alpha\left(2t/T_\pi - 1\right)\right]$, where $t \in \{0, T_\pi\}$, T_π sets the total sweep duration, Ω_{arp} alters the sweep rate, and $\alpha = \arctan(\delta_{max}/\Omega_{arp})$, with δ_{max} being the maximum detuning. The optical intensity is proportional to $\tanh\left[7.5\left(1 - |2t/T_\pi - 1|\right)\right]$. In our apparatus, a Doppler-sensitive Tan/Tanh pulse with duration $T_\pi = 10t_\pi$ achieved ~96% transfer efficiency over a broad range of detuning offsets and was limited primarily by spontaneous emission. The benefits of this ARP have already been discussed in Secs. 2.3, 4.2, and 4.4.3. Here, we note that the minimum adiabaticity of the Tan/Tanh ARP is not significantly lowered by large detuning offsets, even for relatively short pulse durations such as $T_\pi = 3t_\pi$, as shown in Fig. 5-4. The simulated adiabaticities in Fig. 5-4 were obtained using the same sweep parameter values listed at the beginning of this section. The detuning offset of $0.25\Omega_{\text{eff}}$ is relevant to this work since it corresponds to the 1σ Doppler width of a 9-μK ensemble of cesium atoms. The Rational/Square ARP (see Sec. 4.2 for details) is also interesting for LMT applications due to its rapid sweep rate. The constant adiabaticity of this pulse is much lower than that of Tan/Tanh toward the beginning and end of the sweep, but larger by a factor of $\pi/2$ near resonance.

Compared to the two-pulse Ramsey sequences from Chapter 4, large area interferometers call for many additional laser pulses and are sensitive to Doppler detuning. The larger total pulse area increases spontaneous emission, and atom temperature

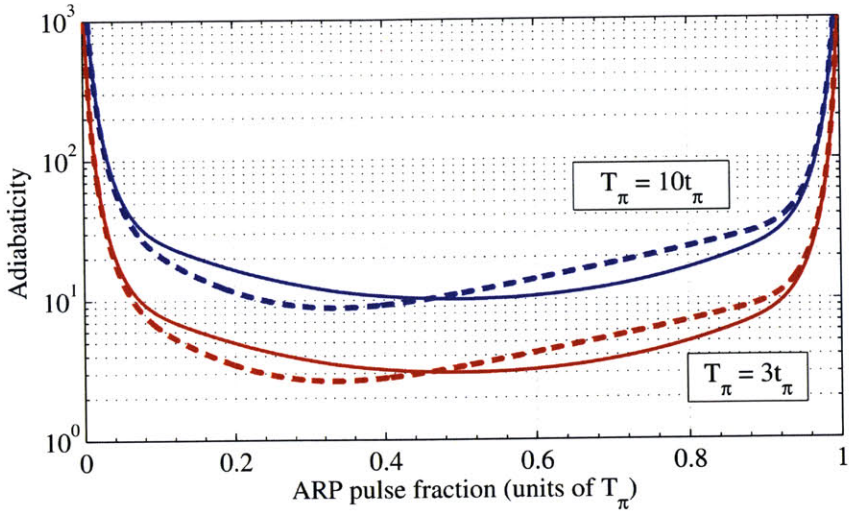

Figure 5-4: Adiabaticity of the Tan/Tanh ARP with $T_\pi = 10t_\pi$ (blue) and $T_\pi = 3t_\pi$ (red). Dashed lines indicate ARP center frequency detunings of $\delta = 0.25\Omega_{\text{eff}}$.

variation across the sample causes detuning inhomogeneity that, in turn, reduces population transfer efficiency. We address these issues in large interferometers by first using ARP pulse durations that are roughly 3 to 10 times shorter than the durations used for timekeeping (in units of t_π). Second, the two-photon Rabi rate in our large area interferometers is about 3 times larger, which improves the velocity acceptance of each augmentation pulse.

Since ARPs in an LMT atom interferometer act on coherences, they imprint a detectable dynamic phase

$$\gamma = \int_0^t dt' \Omega_{\text{gen}}(t')/2 \tag{5.2}$$

onto the atom wavefunction in the adiabatic limit [63, 85][1]. Of course, ARPs that produce minimum adiabaticity factors of $Q = 3$ to 10 only approximately satisfy the adiabatic condition throughout the pulse. Taking $Q = 10$ as our threshold for a coarse adiabatic approximation, we find that the dynamic phase accrued during the Tan/Tanh ARP considered above, with $T_\pi = 10t_\pi$, is $\gamma \sim 100$ rad. When $T_\pi = 3t_\pi$, the first and last 8% of the sweep—during which $Q(t) \geq 10$—produce a dynamic phase of ~20 rad. The magnitudes of these phases create ample opportunity for

[1]The source of this phase factor is apparent in the dressed state picture, which was reviewed in Sec. 2.3.1.

dephasing, since 1-10% variations in γ result in phase dispersion of $\sim$1 rad across the atom ensemble. However, pairs of identical ARP pulses cancel γ when the optical intensity profiles of both pulses are identical.[2] From these considerations, we gather that (1) dynamic phase is a potentially important driver of contrast loss in ARP LMT interferometers, and that (2) applying adiabatic pulses in rapid succession may help cancel this phase.

5.3.2 Composite pulse augmentation

A wide variety of NMR composite pulses efficiently invert population in the presence of detuning offsets and field intensity inhomogeneity. A survey of these pulses can be found in [70]. Composite pulses have also been proposed as efficient atom optics for Raman pulse atom interferometry [11, 64] and implemented as augmentation pulses for LMT atom interferometry [46, 101]. In this work, composite pulses provide an additional point of comparison for augmentation pulse performance. To build on our results reported in [101], we consider MLEV ($\pi/2_{0^\circ} - \pi_{90^\circ} - \pi/2_{0^\circ}$) and WALTZ ($\pi/2_{0^\circ} - \pi_{180^\circ} - 3\pi/2_{0^\circ}$) composite pulses, where subscripts in our notation denote "subpulse" phase and standard-script denotes subpulse area. The trajectory of a Bloch vector under the influence of these pulses is shown in Figs. 5-5(a) and 5-5(b), and experimentally acquired scans of the transfer efficiency as a function of detuning offset are shown in Fig. 5-5(c) for Doppler-insensitive Raman transitions. WALTZ is generally adept at maintaining high transfer efficiency despite detuning offsets, whereas MLEV is insensitive to intensity errors. WALTZ and MLEV are relatively short composite pulses and consequently produce a minimal amount of spontaneous emission. While in principle the phase steps happen instantaneously, in practice they need only occur within a time period that is short with respect to t_π. Our RF electronics limit phase transients to $\sim 0.01 t_\pi$ for Rabi rates of $\Omega_{\text{eff}}/(2\pi) = 200$ kHz. Finally, to differentiate composite pulse results presented here from those in [101], we note that the current results were acquired with separated Raman frequencies, higher

[2] This concept has been used in NMR to produce adiabatic $\pi/2$ pulses that are robust to intensity inhomogeneity [69].

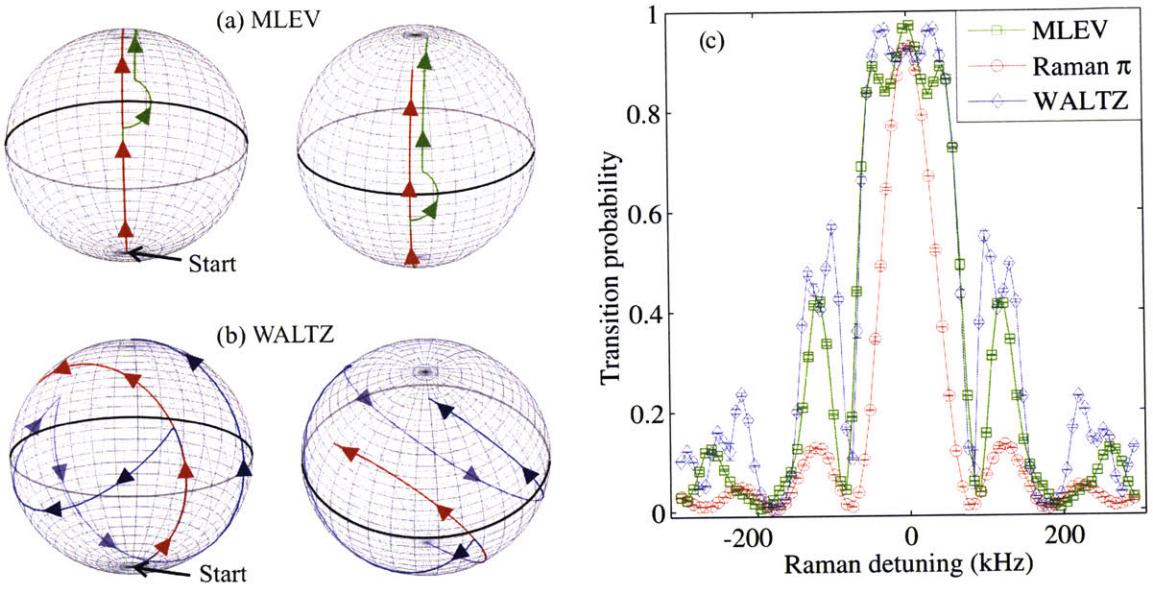

Figure 5-5: Action of (a) MLEV (green) and (b) WALTZ (blue) pulses on the Bloch vector, as compared to a Raman π pulse (red). MLEV is shown for the case of a 15% reduction from nominal intensity, and WALTZ is shown with a detuning error of $0.5\Omega_{\text{eff}}$. Perfect transfer corresponds to a Bloch vector reaching the positive z axis. (c) Experimental observation of broadband transfer efficiency with composite pulses using Doppler-insensitive atom optics. Lines are guides for the eye.

Rabi rates, and hotter atom clouds for reasons discussed in Secs. 3.6 and 5.1.

5.4 Demonstration of large area atom interferometry

5.4.1 Enhanced scalefactor

To experimentally verify the enhancement of phase shift per unit acceleration $\Delta\phi/a$, we produced interferograms by varying the chirp rate c_r of the Raman frequency difference $\omega_1 - \omega_2$. Changes to the chirp rate act as pseudo-accelerations $\delta a = c_r/k_{\text{eff}}$ that shift the interferometer phase according to Eq. (5.1). In response to chirp rate variation, interferograms with up to $30\hbar k$ beamsplitter pulses exhibited periods that decreased with higher LMT order and matched expected values, as shown in Fig. 5-6. A short dwell time of $T = 1$ ms was used to reduce phase noise from environmental vibration. Furthermore, chirp rate conditions were sampled in order from lowest to highest value, with each value tested 10 to 15 times for averaging. Other experimental parameters included $T_\pi = 3t_\pi$, $\Omega_{\text{eff}}/(2\pi) = \Omega_{arp}/(2\pi) = 200$ kHz, $\delta_{max}/(2\pi) = 15$ MHz, and $\tau_{lmt} = 41$ μs. Similar agreement was verified for up to $14\hbar k$ beamsplitters with other augmentation pulses, such as Raman π pulses, MLEV, WALTZ, and Tan/Tanh ARPs with $T_\pi = 5t_\pi$. Percent-level discrepancies between the measured and predicted scale factors may be due to finite pulse duration effects [81], which were not included in the predictions.

5.4.2 Contrast loss

While the LMT interferometers clearly enhanced the phase shift per unit acceleration, the contrast A of the interferograms in Fig. 5-6 was simultaneously degraded with increasing LMT order. Maintaining contrast is important because it scales the phase SNR and can thus reduce sensitivity despite the enhancement of scale factor. To avoid systematically underestimating contrast because of vibration-induced phase noise, we assessed contrast using histograms of transition probability measurements from each LMT interferometer. The arcsine probability density function characterizes

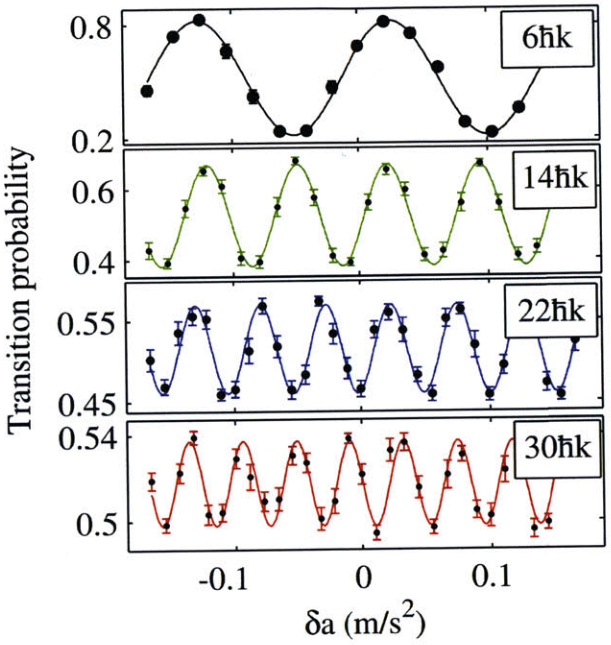

LMT order [$\hbar k$]	$\Delta\phi/a$ [rad s^2/m] Measured	Predicted
2	14.8(3)	14.9
6	41.5(3)	41.7
10	67.1(5)	65.7
14	88.3(3)	86.9
18	105.3(4)	105.1
22	122.3(7)	120.5
26	—	133.1
30	149.1(7)	146.9

Figure 5-6: Phase shift per unit acceleration $\Delta\phi/a$ for various LMT orders with Tan/Tanh augmentation pulses. Interferograms were acquired by perturbing the chirp rate of the Raman difference frequency, which produced a time-varying Doppler shift. δa represents the acceleration of the atoms, relative to the Raman beams, that produces the equivalent Doppler shift when the chirp rate is fixed. Points represent 10- or 15-shot averages, error bars indicate standard error, and lines are fitted sine waves. The table shows reasonable agreement between measured and predicted values ($26\hbar k$ was not measured).

the statistics of the interferometer transition probability in the limit of uniform random phase noise [78]. In our experiments, this limit was effectively realized through a combination of vibration-driven phase noise and deliberate variation of the interferometer phase [115], as seen in Fig. 5-7. We therefore fit the arcsine distribution to our histograms, while keeping A a free parameter. The resulting contrast estimates matched separate estimates of contrast based on the standard deviation of the transition probabilities: $A_\sigma = 2\sqrt{2}\sigma_P$.

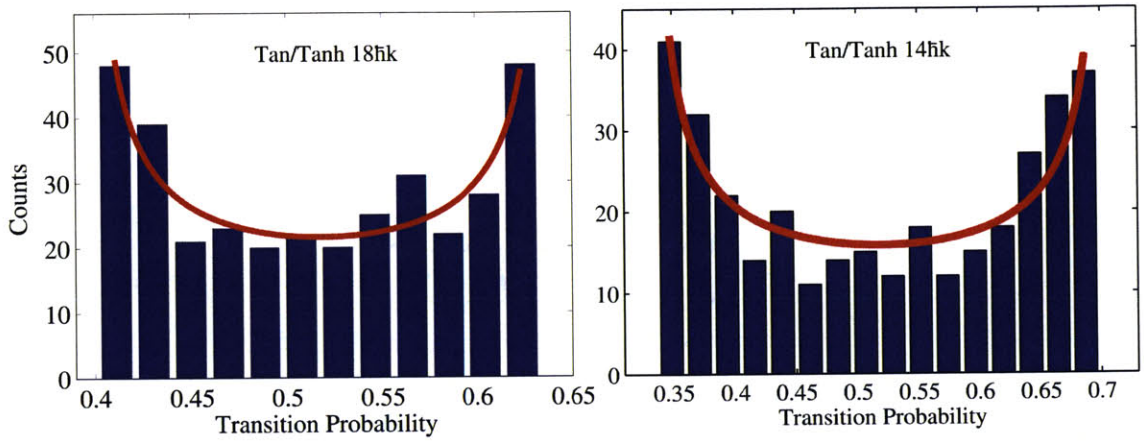

Figure 5-7: Histograms of transition probabilities from Tan/Tanh $14\hbar k$ and $18\hbar k$ interferometers with randomly varying phase and statistics governed by the arcsine distribution (red curves).

Changes in contrast with varying LMT order are driven by several factors: single-photon excitations; detuning offsets due to photon recoils; detuning inhomogeneity due to temperature-dependent Doppler shifts; and Rabi rate and spatial phase inhomogeneity due to a combination of wave front distortion and thermal motion of the atoms. To jointly study these effects, we used Monte Carlo interferometer simulations described in detail in Appendix B. Briefly, we note that simulations accounted for inhomogeneity effects listed above by using initial atom positions and velocities that were normally distributed and centered on the Raman beam axis. A CCD image of the spatial intensity profile of only one Raman laser beam was used to approximate the true variation in Ω_{eff} with position. Non-ideal spatial modes are an important source of contrast loss in ARP-based LMT interferometers, because they introduce

variations in the dynamic phase γ across the sample. We empirically determined that, due to spontaneous emission, the fractional loss of population per Raman π pulse was $R_{sc} = 0.004$. Therefore, we scaled the simulated contrast results by $(1 - R_{sc})^{4Nt_{aug}+2}$, where t_{aug} is the augmentation pulse duration in units of t_π, and the exponent quantifies the pulse duration for the entire interferometer. The Raman process was modeled as an effective two-level system [81], and we assumed uniform Raman wave fronts. To reduce computation times, probability amplitudes corresponding to population loss were not computed, as they do not contribute significantly to contrast.

Experimentally measured and simulated contrast values are shown in Fig. 5-8(a) for Tan/Tanh pulses and Fig. 5-8(b) for composite pulses. At all LMT orders,

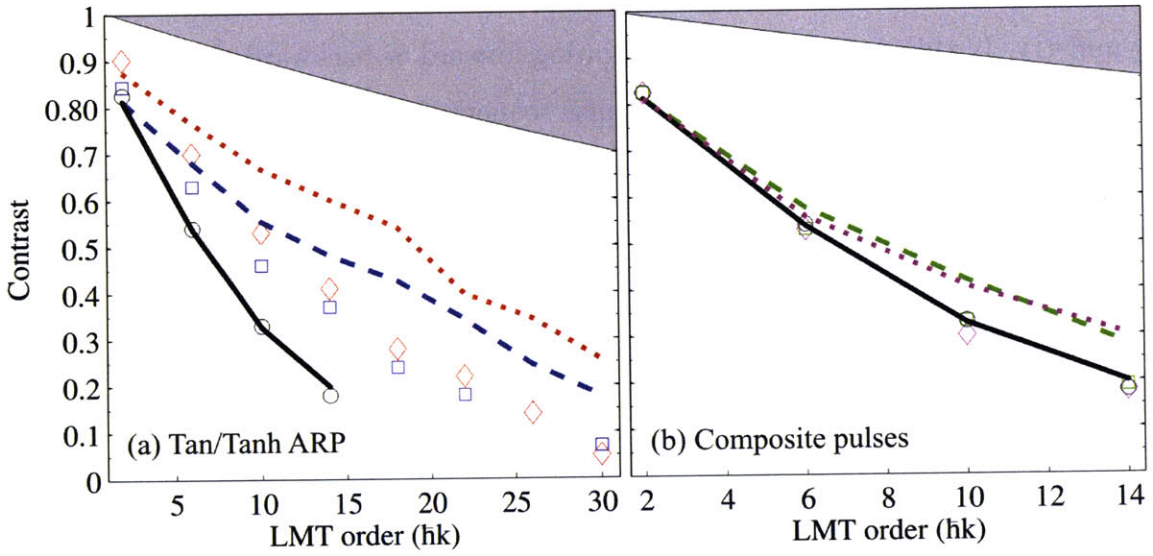

Figure 5-8: Contrast as a function of LMT order for (a) Tan/Tanh ARP augmentation with velocity-selected (red diamonds) and 9-μK atoms (blue squares); (b) composite pulse augmentation with WALTZ pulses (magenta diamonds) and MLEV pulses (green squares). Both plots include Raman augmentation (black circles) for comparison. The bottoms of the gray regions indicate spontaneous emission-limited contrast in LMT interferometers augmented with WALTZ and Tan/Tanh pulses. Symbols represent contrast fits to histograms of transition probabilities. Contrast fit uncertainties are nearly equivalent to the symbol sizes. Lines are Monte Carlo predictions.

Tan/Tanh interferometers with the entire laser cooled sample clearly achieved higher contrast than interferometers based on Raman π or composite pulses. To observe contrast enhancement with Tan/Tanh pulses, we had to simplify and clean many optical

components in the Raman beam path. In the process, we replaced the original vacuum cell to remove a defect on the vacuum-side of an optical flat that created intensity ripples in the Raman beam. These improvements benefited ARP augmentation moreso than π pulse augmentation. Using velocity-selected samples with temperatures of $\sim$100 nK along the Raman beam axis, we observed a nominal increase in contrast. Since this improvement was largely driven by the $2\hbar k$ interferometer, inhomogeneity in the temperature-dependent Doppler detuning was not a dominant contrast loss mechanism. Experimental composite pulse LMT interferometers (without velocity selection) performed as well as interferometers with Raman π augmentation. Note that the WALTZ interferometers were acquired with the last $2N$ augmentations acting in reverse (i.e., $3\pi/2_{0^\circ} - \pi_{180^\circ} - \pi/2_{0^\circ}$ pulses) in order to achieve time-reversal symmetry. In this case, an atom propagating forward or backward through the interferometer would experience the same pulse sequence. This modification resulted in a 5-10% fractional improvement in contrast.

Using known experimental parameters and adjustments to the atom sample size (order 10%), our Monte Carlo simulation produced contrast values, shown in Fig. 5-8, that agreed with measurements based on Raman π augmentations. With the same experimental parameters, simulations based on Tan/Tanh augmentation pulses predicted higher levels of contrast at all LMT orders. These predictions were borne out qualitatively in experiments, though the measured contrast values were lower. Taking the same approach with composite pulse interferometers also produced optimistic contrast predictions. The discrepancy may have resulted from a favorable model of the Raman beam spatial profile, which accounted for just one of the two Raman beams. Other sources of disagreement may have included dephasing due to spatial aberrations in the Raman beam wave front and temporal variation of the Raman beam intensity.

Assuming contributions from other noise processes (e.g., laser phase noise) were unchanged with varying LMT order, the inferred sensitivity (defined as $A \times \Delta\phi/a$) was maximized with $14\hbar k$ Tan/Tanh beamsplitters and was a factor of 2.6 larger than that of a $2\hbar k$ interferometer, as shown in Fig. 5-9. If contrast is perfectly maintained,

$30\hbar k$ beam splitters can enhance the sensitivity by a factor of 15 when $T \gg \tau_{lmt}$. For our choice of short T, this sensitivity enhancement can be a factor of 10, in principle.

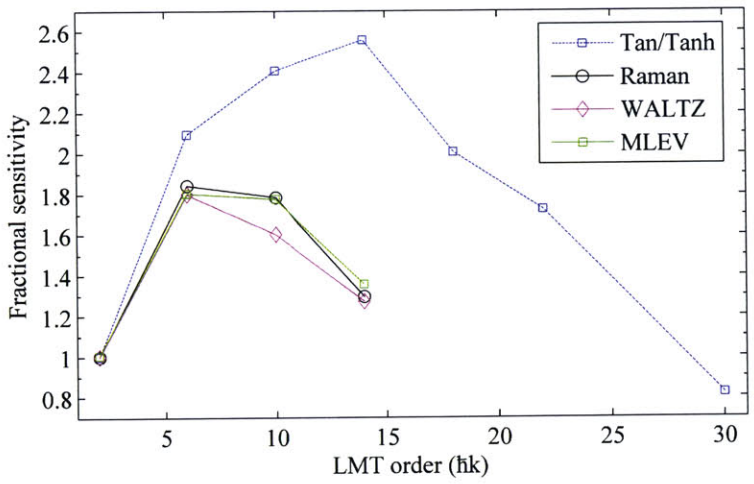

Figure 5-9: Enhancement of inferred acceleration sensitivity ($A \times \Delta\phi/a$), relative to the sensitivity of a $2\hbar k$ interferometer, as a function of LMT order for augmentation with Tan/Tanh ARP, composite, and Raman π pulses. Lines are guides for the eye.

As a function of dwell time T, and with an ARP pulse duration of $T_\pi = 3t_\pi$, the measured contrast in Fig. 5-10(a) decreased at a rate of roughly 0.03/ms for all LMT orders. Note that estimates for the $6\hbar k$ interferometer were based on a contrast measurement at $T = 1$ ms and the fairly uniform trend observed with all other LMT orders. This trend was likely caused by the transverse motion of atoms in laser beams with spatially non-uniform intensity and wave front aberrations, both of which increasingly dephase the atoms as T is lengthened [79]. In the case of wave front aberration, dephasing occurs because spatially separated and localized atom wavepackets are imprinted with different position-dependent Raman phases. With non-uniform spatial intensity, the dynamic phase during an ARP varies across the ensemble, as will be discussed below. Transverse thermal motion of atoms was substantial in this work, since a 9-μK cloud of ^{133}Cs atoms, with an initial $1/e^2$ diameter of 2 mm, expands by 40% during an interferometer with $T = 8.5$ ms. Clearly, microkelvin-temperature and velocity-selected atom samples place more stringent requirements on the transverse

spatial mode of the atom optics beams, when compared to LMT demonstrations with small BECs. With improved beam quality, however, large area interferometry becomes possible without the complexity of evaporative cooling or atom optics based on Bragg transitions, which usually require narrow-linewidth ($\sim$ 10 kHz) lasers [78, 113].

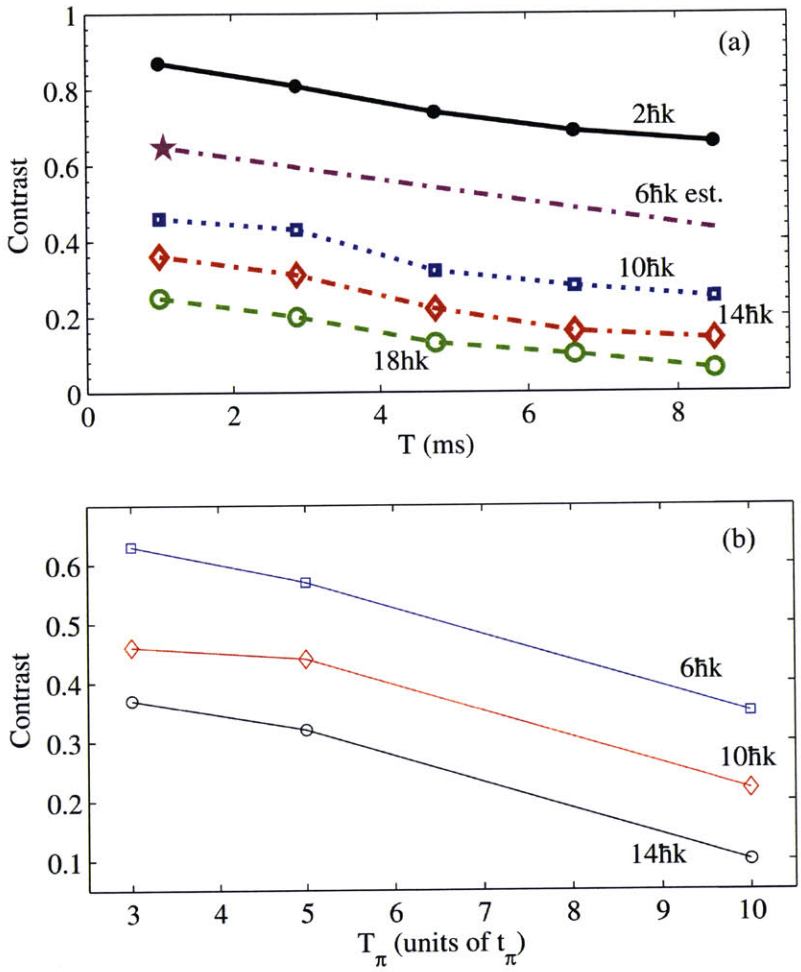

Figure 5-10: Large area interferometer contrast with various (a) dwell times and (b) Tan/Tanh pulse durations. a) The contrast trends down with T at a rate of ~ 0.3/ms for all LMT orders, suggesting the atoms are dephased by their motion through a non-ideal spatial beam mode. b) The contrast also trends down with increasing Tan/Tanh pulse duration T_π, due to spontaneous emission and dispersion of the dynamic phase. Lines are guides for the eye. Symbols represent contrast fits to histograms of transition probabilities. Fit uncertainties are smaller than the symbol sizes.

As a function of increasing ARP sweep duration T_π, the contrast seen in Fig.

5-10(b) decreased for all LMT orders considered. The dwell time for these interferometers was $T = 1$ ms. Spontaneous emission and dispersion of the dynamic phase γ most likely dominated this trend, since the pulse area more than tripled over this range of T_π. Under relevant conditions, differentiation of Eq. (5.2) with respect to Ω_{eff} reveals that for a Tan/Tanh ARP, variations in γ caused by the uncertainty in Ω_{eff} scale with the ARP duration T_π.[3] A crude adiabatic approximation thereby indicates that dephasing of γ during a $T_\pi = 10t_\pi$ ARP is approximately a factor of 3.3 larger than dephasing from a $T_\pi = 3t_\pi$ ARP. This estimate, however, neglects the effect of *re*phasing, which was discussed qualitatively in Sec. 5.3.1. Recall that if Ω_{eff} were constant, consecutive pairs of contiguous augmentation pulses would cancel γ in the adiabatic limit, because the imprinted phases would carry opposite signs. The fractionally larger loss of contrast observed experimentally at longer T_π suggests that rephasing in this experiment was hampered by poor laser beam mode quality. Monte Carlo simulations of a $6\hbar k$ interferometer with $T_\pi = 10t_\pi$ Tan/Tanh augmentation show that, in the case of an ideal Gaussian laser beam mode, the contrast is limited purely by spontaneous emission and rephasing is highly efficient. We have also experimentally observed rephasing with four-pulse interferometers comprising a $\pi/2 - \text{ARP} - \text{ARP} - \pi/2$ sequence of Doppler-sensitive atom optics with the same $\mathbf{k}_{\text{eff}}$ orientation. The four-pulse interferometer contrast was 0.35 for identical ARPs and 0 for ARPs with oppositely-directed frequency sweeps, which cause the two dynamic phases to add. Therefore, improvements to the spatial mode quality of the Raman beams may enable application of spontaneous emission-limited Tan/Tanh pulses with $T_\pi > 3t_\pi$. These more adiabatic pulses should efficiently cancel dynamic phases, particularly when LMT beamsplitters comprise an even number of augmentation pulses (i.e., even N). Cancellation of γ will also require precise control over ARP sweeps parameters. Finally, further suppression of spontaneous emission and simultaneous cancellation of the AC Stark shift is possible with far-detuned, high-power lasers.

[3]For simplicity, we have assumed that the optical intensity is unmodulated, $\delta_{max} \gg \Omega_{\text{eff}} = \Omega_{arp}$, and that there are no detuning offsets.

5.4.3 ARP sweep parameters

We additionally checked for contrast and phase sensitivity to Tan/Tanh sweep-defining parameters Ω_{arp} and δ_{max}, which can vary when RF electronics add imperfections to ARP frequency sweeps. The nominal experimental parameters were the same as above, except for $T_\pi = 5t_\pi$. Over a broad range of Ω_{arp} and δ_{max} values, a $6\hbar k$ interferometer displayed fairly small variation in contrast, as seen in Fig. 5-11. In real applications, the fractional values of these parameters will be controlled at the 1% level or better, resulting in negligible contrast instability. A bona fide assessment of phase stability requires an inertially stable system in which environmental acceleration noise is heavily suppressed. We reduced this noise in a stability measurement, discussed in Sec. 3.6, using a retroreflected Raman beam with the reflector mounted on a vibration isolating platform. Since LMT interferometry was implemented with separated Raman beams, vibration isolation was more complicated and not pursued for this initial demonstration of high contrast and correct scale factor. Questions regarding phase instability will be answered when the experiment is rehosted on an isolated platform. Nevertheless, a $6\hbar k$ interferometer with a short dwell time allowed us to resolve interferograms whose phase offsets are reported in Fig. 5-11. Clearly, the phases are controlled to well within a fringe. The phase response to δ_{max} variation, if present, cannot be resolved; the response to Ω_{arp} variation near the nominal setting of $\Omega_{arp} = \Omega_{\text{eff}}$ may be statistically significant. The standard deviations of the Ω_{arp} and δ_{max} phase offsets are both $<$70 mrad. The limited sensitivities in LMT interferometers to ARP parameters is promising and motivates further investigation at higher LMT orders.

5.5 Symmetric Raman beamsplitters

The LMT beamsplitters described above separate atom wavepackets in an asymmetric fashion: the diffracting wavepacket receives two photon recoils while the non-diffracting wavepacket continues on its original trajectory. This asymmetry is problematic in certain space-based interferometers intended to detect gravitational waves.

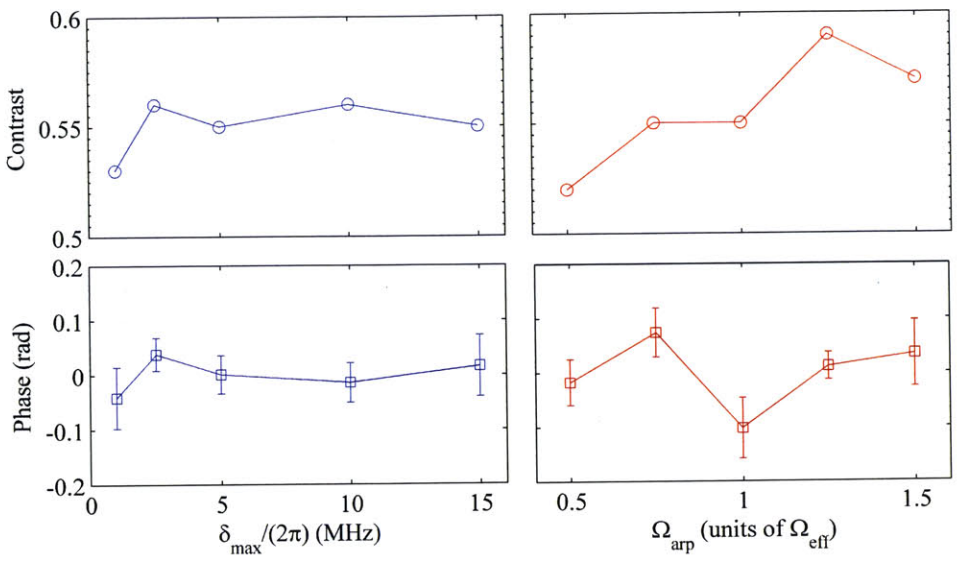

Figure 5-11: Effect of Tan/Tanh parameters Ω_{arp} and δ_{max} on the LMT interferometer contrast and phase of a $6\hbar k$ interferometer. Lines are guides for the eye, and symbols represent contrast fits to histograms of transition probabilities. Contrast fit uncertainties are similar to the symbol sizes.

While the details of atom interferometric gravitational wave detection are beyond the scope of this thesis, we briefly note that the issue at hand results from considerations of orbital dynamics and the requirement that interfering wavepackets overlap at the end of an interferometer. If the Raman beams are parallel to the tangential velocity of the atom cloud, momentum kicks from the atom optics drive changes in velocity that alter the wavepacket altitude. For long dwell times on the order of 1 s, wavepacket separation prior to the final atom beamsplitter pulse reaches the 10-μm level [116], which is roughly 1000 times the coherence length of the microkelvin-temperature atoms used in this work. The wavepackets in this scenario no longer overlap and contrast is completely suppressed. Even ultracold atoms would fail to achieve coherence lengths that produce interference.

The wavepackets can be made to overlap, and thus revive contrast, using symmetric beamsplitters and mirrors based on Raman transitions. For the symmetric beamsplitter, a $\pi/2$ Raman pulse with Doppler-insensitive (DI) Raman frequencies first creates a superposition of internal ground states. A subsequent π pulse with

Doppler-sensitive (DS) frequencies provides symmetric wavepacket deflection about the classical atom trajectory. Similarly, the mirror is composed of a sequence of $\pi_{\mathrm{DS}} - \pi_{\mathrm{DI}} - \pi_{\mathrm{DS}}$ Raman pulses. The thick blue lines in Fig. 5-12 depict the desired wavepacket trajectories for a 7-pulse, $4\hbar k$ interferometer based on symmetric atom optics. Other lines indicate loss channels that contribute spurious interference signals. The pulse timings are identical to the case of a $6\hbar k$ interferometer, shown in Fig. 5-1. In particular, a long dwell time separates the DI atom optics, which are closely preceded or followed by the DS pulses. We note that this interferometer was previously described in [54], but with microwave pulses in place of optical DI Raman pulses. Experimental results were not discussed. Other approaches to symmetric Raman beamsplitters [117, 100] produced similarly structured Mach-Zehnder interferometer arms, but with wavepackets in the same internal state. In this case, the interferometer phase becomes insensitive to AC Stark and Zeeman shifts common to both arms, and loss channels can be extirpated with resonant light that is far detuned from wavepackets in the primary interferometer arms.

To experimentally implement the symmetric interferometer, we used the retroreflected Raman beam described in Sec. 3.6. The beam was circularly polarized (rather than cross-linearly polarized) to avoid suppressing the DI transition and enable rapid switching between DI and DS Raman pulses. The atom cloud fell for 13 ms prior to interferometry, allowing the Doppler shift to lift the degeneracy between DI and DS transitions. These transitions were selectively driven by choosing the appropriate Raman detuning. Using a dwell time of 1 ms and a 40-μs separation time between DI and DS pulses, we scanned the chirp rate of the Raman difference frequency to verify that the scale factor of the symmetric interferometer was roughly twice that of a $2\hbar k$ interferometer. The contrast of the symmetric interferometer ($A_{\text{7-pulse}} = 0.11$) was two-thirds that of the $2\hbar k$ interferometer ($A_{\text{3-pulse}} = 0.17$), as seen in Fig. 5-13. Though the overall contrast values were low, the results indicate the potential for a 33% sensitivity improvement, even in our unoptimized implementation.

Low contrast values were most likely due to the combination of hot atom temperature (9 μK) and relatively low Rabi rate ($\Omega_{\mathrm{eff}}/(2\pi) = 55$ kHz), which allowed

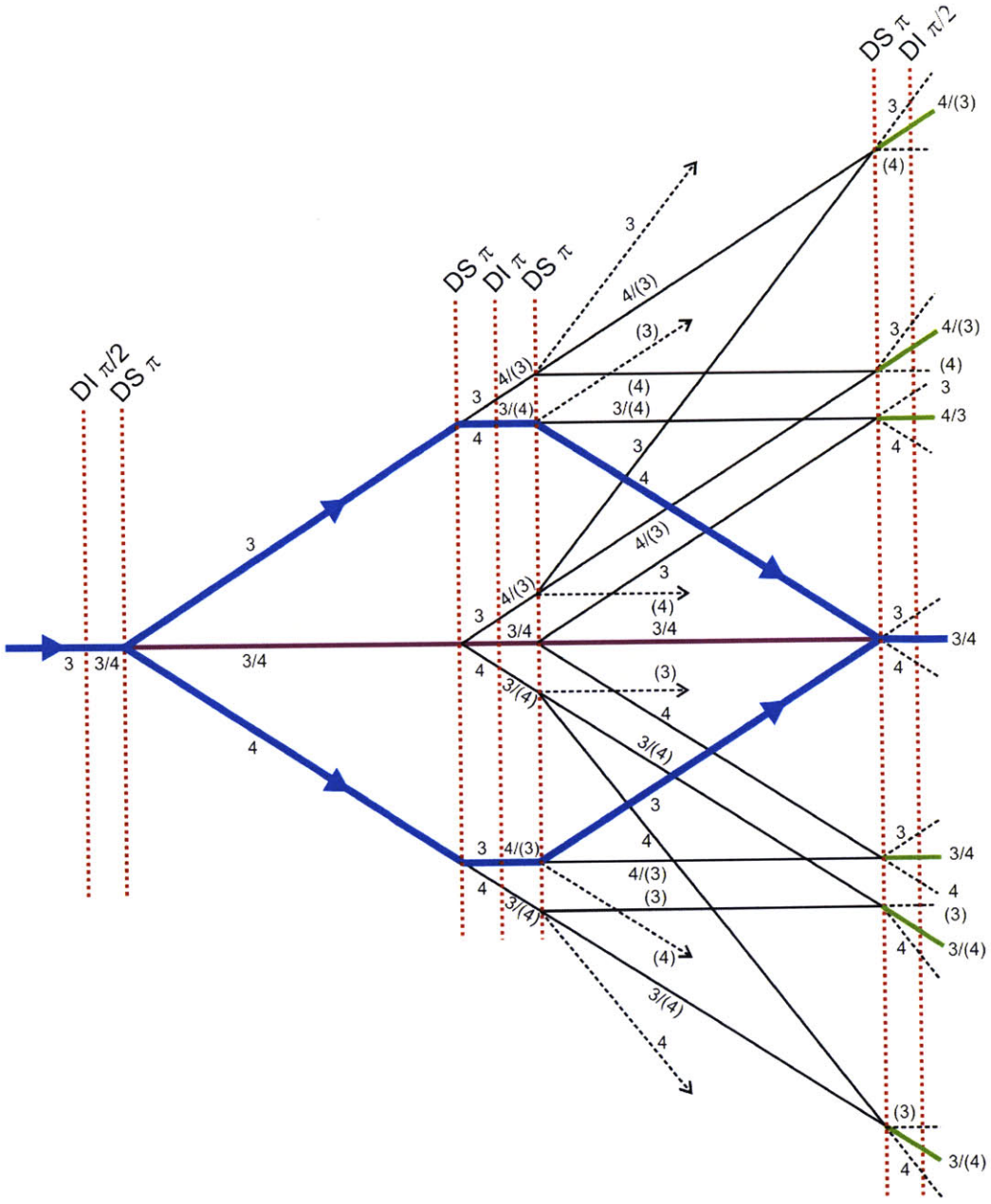

Figure 5-12: Diagram of a symmetric Raman pulse interferometer. Vertical lines (dotted red) represent Raman pulses and the thick lines (blue) indicate the primary interference channels. Spurious interfering outputs at the end of the interferometer are highlighted (green), and non-interfering paths are truncated (dashed lines). Numbers 3 and 4 refer to the internal state of the local wavepacket, with slashes identifying superposition states and parenthesis indicating population resulting from transfer inefficiency of the DI π pulse. The horizontal midline (purple) marks a troublesome loss channel, since it interferes with the primary interferometer loop.

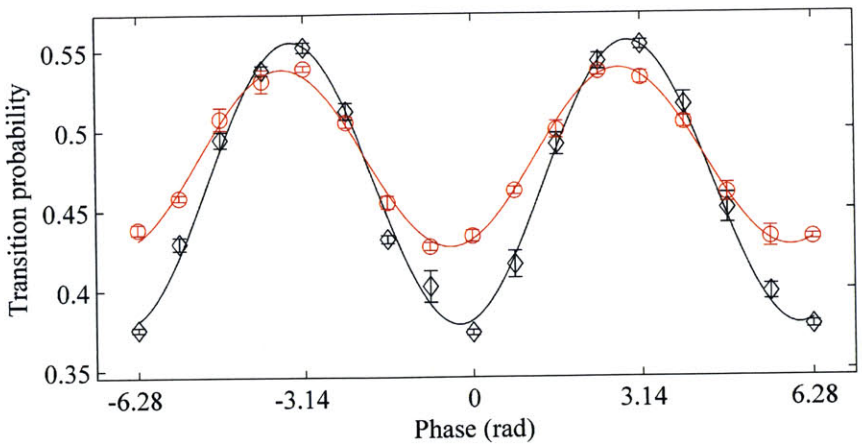

Figure 5-13: Interferogram from a symmetric, $4\hbar k$ Raman pulse interferometer (red circles), acquired by stepping the phase of the final beamsplitter pulse. All lines are sinusoidal fits. Since a $2\hbar k$ interferometer (black diamonds) achieved roughly 50% higher contrast, the symmetric interferometer potentially improved the sensitivity by 33%. The relatively low contrast values resulted from a combination of hot atom temperatures and weak Rabi rate.

substantial population transfer to interferometer loss channels, such as the purple midline path in Fig. 5-12. Additionally, the 13-ms drop time prior to interferometry limited the frequency separation between DI and DS Raman transitions and likely allowed for residual mixing of these processes. Future iterations of this experiment will benefit from efficient Raman pulses that drive either DI or DS transitions, but not both. Raman ARP may then provide a nearly ideal DI mirror that is robust to beam inhomogeneity, as will be discussed in Sec. 5.5.1. Such pulses would prevent population from reaching trajectories labeled with parenthesis in Fig. 5-12 and thereby reduce spurious interference. An even simpler approach involves substituting microwaves for DI laser pulses, as suggested in [54]. However, for a space-based sensor relying on long baseline atom interferometry, DI Raman laser beams will ultimately be necessary.

5.5.1 Mach-Zehnder ARP interferometers

The symmetric interferometer described in Sec. 5.5 is fundamentally a DI Mach-Zehnder interferometer with auxiliary DS augmentation pulses. The fidelity of DI

atom optics is relatively simple to optimize, as it is insensitive to inhomogeneities in atomic Doppler detuning and only suffers from Rabi rate variation across the atom cloud. Optimized DI atom optics would improve the prospects for a high-contrast, symmetric Raman interferometer. Section 2.3 explained how transfer efficiency with ARP in the adiabatic limit becomes robust to intensity uncertainty. This robustness can be extended to DI Mach-Zehnder interferometers based on ARP beamsplitters (see Secs. 5.5 and 4.3) and an ARP mirror, which is described next.

In general, the Mach-Zehnder atom interferometer comprises a beamsplitter–mirror–beamsplitter sequence of atom optics. For ARP atom optics, the mirror cannot be fashioned from a continuous sweep of the Raman detuning, as was done in the LMT interferometers of Sec. 5.4.2. The dynamic phase from such a pulse is never canceled in a three-pulse interferometer, and would thus lead to decoherence and phase noise from Raman beam intensity variation. Instead of a continuous sweep, we use an ARP composite pulse composed of two parts shown on the Bloch sphere in Fig. 5-14. The first part is identical to the first half of a downward inversion sweep; the second part is identical to the second half of an upward inversion sweep. In between these two parts, the phase of the drive field is instantaneously shifted by π rad in the equatorial plane. Unlike in previous discussions of ARP atom optics, this ARP mirror acts on a Bloch vector initially in the equatorial plane. Precession of the Bloch vector, in the plane orthogonal to the slowly-rotating drive field, is a manifestation of the dynamic phase. Shifting the phase in the middle of the ARP reverses the precession and cancels the dynamic phase if the intensity remains constant during the pulse [69].

An interferogram from a DI Mach-Zehnder interferometer with Tan/Tanh ARP pulses is shown in Fig. 5-15(a). Its contrast is comparable to that achieved with standard Raman atom optics. Additionally, the uncertainties in the transition probability measurements are not noticeably different for the two pulse types, indicating that phase noise from ARP was controlled. Experimental parameters were $T = 900$ μs, $\Omega_{\text{eff}}/(2\pi) = \Omega_{arp}/(2\pi) = 86$ kHz, $\delta_{max}/(2\pi) = 15$ MHz, $T_\pi = 10.3t_\pi$, and $\beta = 7.5$.

The contrast achieved with standard Raman atom optics was sensitive to fre-

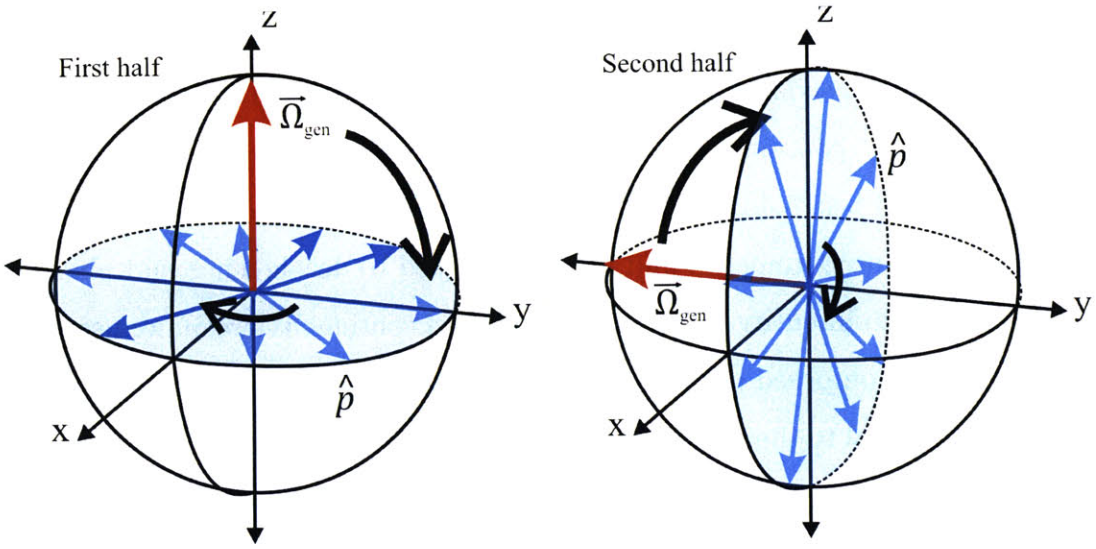

Figure 5-14: Bloch sphere depiction of an ARP mirror that acts on atomic coherences. The first half of the pulse adiabatically rotates the drive field from the z to y axis, inducing precession of Bloch vectors initially in the equatorial plane. Due to Rabi rate inhomogeneity, these vectors form a disc (blue) that remains orthogonal to the rotating drive field in the adiabatic limit. Next, the phase of the drive field is stepped by π rad, and the second half of the mirror begins. The field now rotates toward the positive z axis while reversing Block vector precession, thus canceling the dynamic phase.

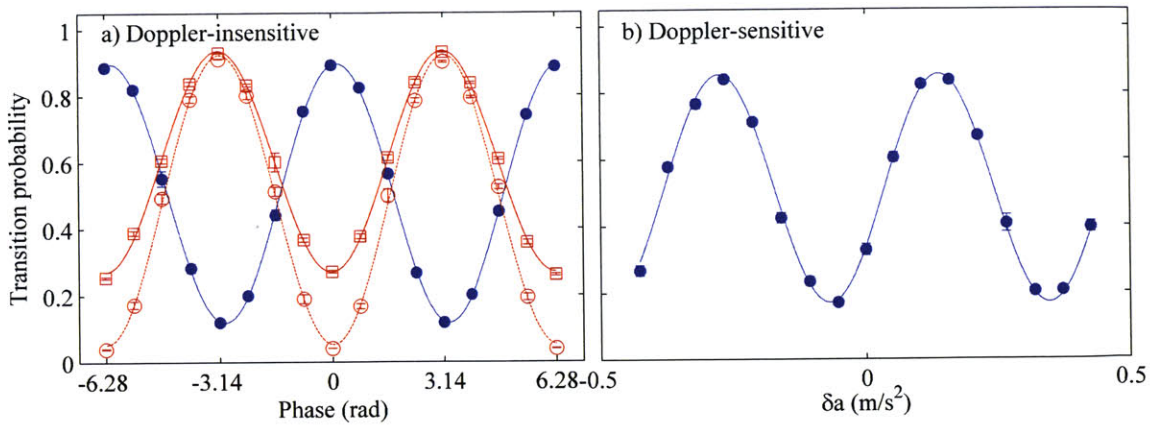

Figure 5-15: Interferograms for Mach-Zehnder ARP interferometers. a) DI Tan/Tanh ARP atom optics (blue filled circles) produced contrast values similar to the contrast achieved with standard Raman pulses (red circles/squares). Contrast fractionally improved by 25% (red circles) due to a detuning offset of -324 Hz (see text). b) DS ARP interferometer with correct scale factor and contrast of 0.68. The utility of this interferometer, relative to the standard Raman pulse approach, is limited by sensitivity of the ARP mirror to Doppler detuning inhomogeneity. All lines are sinusoidal fits.

quency errors, as evidenced by the 25% contrast variation in response to detuning, seen in Fig. 5-15(a). This sensitivity is, in fact, a result of both Rabi rate inhomogeneity and detuning offset. Rabi rate inhomogeneity disperses the Bloch vectors of different atoms, since they precess at varying rates during a standard Raman pulse. During the dwell time, the detuning δ shifts the phase of the second Raman pulse, relative to the first, by $\Phi = \delta T$. If $\Phi \approx \pi$, the second pulse rotates the Bloch vectors back toward their initial orientation, canceling their dispersion and leading to improved contrast [45]. Such contrast sensitivities, which can create instability, should not arise in the ARP Mach-Zehnder interferometer, because the mirror is insensitive to Φ.

We also implemented a DS Mach-Zehnder interferometer with these ARP atom optics and produced the interferogram shown in Fig. 5-15(b). Experimental parameters in this case were $T = 1$ ms, $\Omega_{\text{eff}}/(2\pi) = \Omega_{arp}/(2\pi) = 200$ kHz, $\delta_{max}/(2\pi) = 15$ MHz, $T_\pi = 10t_\pi$, and $\beta = 7.5$. By varying the chirp-rate of the Raman difference frequency, we verified that the scale factor was correct and also achieved good contrast.

The Doppler detuning sensitivity, however, limited the value of this interferometer over the standard Raman pulse approach. Due to its non-adiabatic phase shift, the ARP mirror achieved a velocity acceptance similar to that of a Raman π pulse. In parameter regimes where the Rabi rate is much larger than the Doppler detuning inhomogeneity, the DS Mach-Zehnder interferometer with ARP atom optics could prove useful for its robustness to intensity variation.

5.6 Summary

We have presented LMT light pulse atom interferometry using atom optics based on stimulated Raman transitions with ARP and composite pulses. The $30\hbar k$ beamsplitters reported here provide the largest momentum separation achieved to date in an interferometer without velocity selection or evaporative cooling. In principle, the beamsplitter momentum transfer could be increased beyond $30\hbar k$ by switching to diffraction of a single interferometer arm with resonant pulses. This approach is efficient when the separation between wavepacket resonances (induced by photon recoils) exceeds the temperature-dependent detuning inhomogeneity. For a 1-μK sample of ^{133}Cs atoms, $14\hbar k$ beamsplitters would provide the necessary frequency separation. By incorporating the entire laser-cooled atom sample into the measurement, our ARP technique provides superior counting statistics compared to previously demonstrated LMT atom interferometers. Retaining the full cold atom sample also enables operation at higher data-rates and reduces deadtime, since cold atoms can be rapidly recaptured in a MOT during subsequent measurements. These features would be useful measurement of dynamic signals, such as accelerations and rotations of moving platforms. For space-based applications, we have demonstrated symmetric Raman beamsplitters and mirrors that could facilitate wavepacket overlap despite long interrogation times. A demonstrated Mach-Zehnder interferometer based purely on ARP atom optics could be useful in this application.

Chapter 6

Conclusion

We have presented techniques for light pulse atom interferometry with atom optics based on a combination of frequency-swept adiabatic rapid passage (ARP) and stimulated Raman transitions with optical photons. In one application, a method for robust atomic timekeeping with ARP Ramsey sequences was developed. Raman ARP was vital to suppressing light shifts of the Ramsey phase, as well as loss of fringe contrast due to optical intensity gradients in a Gaussian laser beam. In experiments, Raman ARP reduced the phase sensitivity of Ramsey sequences to light shifts in ^{133}Cs atoms by about two orders of magnitude, relative to standard, fixed-frequency Raman transitions. Furthermore, the Ramsey fringe contrast was maintained for atom cloud displacements that approached the $1/e^2$ intensity radius of the laser beam. A stability assessment of the ARP Ramsey measurement revealed a fractional frequency uncertainty of $\sim 3.5 \times 10^{-12}$ after about 2500 s of averaging. This uncertainty was limited primarily by second-order Zeeman shifts.

In a second application, Raman ARP was used in an acceleration-sensitive Mach-Zehnder atom interferometer to achieve large momentum transfer (LMT) atom optics. The combination of ARP and high Rabi rate afforded atom beamsplitters that produced momentum splittings of up to 30 photon recoil momenta between interfering wavepackets, which is a record for Raman transitions and atoms cooled purely in an optical molasses. Enhancement of the phase shift per unit acceleration was verified for many LMT orders, and sources of contrast loss were characterized using Monte

Carlo simulations. By forgoing evaporative cooling and velocity selection, this LMT method reduces the atom shot-noise-limited measurement uncertainty and enables large area atom interferometry at higher (>10 Hz) data-rates.

6.1 Future work

The results presented in this thesis could be built upon by modifying certain aspects of the apparatus or experimental methods. The primary source of instability in our Ramsey sequences was the magnetic field environment. Operating the sensor inside magnetic shielding should strongly suppress this contribution. Efforts to add magnetic shielding have already been made in another apparatus operated by our group, and a factor-of-2 improvement to the short-term stability of the ARP Ramsey sequence was evident. To create a bona fide clock, the atomic Ramsey phase measurements must also be fed back to a disciplined crystal oscillator whose frequency is counted. The short-term stability of the clock could be lowered using higher data-rates (discussed below) and readout pulses derived from narrower-linewidth lasers, which reduce the readout uncertainty. Improving the long-term stability will likely require active optical intensity control, temperature control for RF circuits, and periodic recalibration of light background levels.

The contrast of our LMT atom interferometers with ARP atom optics was limited by optical beam quality. Better beam quality can be achieved through exclusive use of clean $\leq\lambda/10$ optical components and vacuum cell windows. To reduce phase noise and carefully characterize LMT interferometer phase shifts, the apparatus must be vibrationally isolated, and differential phase between the separate Raman lasers should be actively controlled. Reduction of atom temperatures to 1–2 μK would help reduce loss of contrast with increasing dwell time and could be achieved through polarization gradient cooling of cesium atoms [113] (which currently produces 9-μK atom temperatures in our system). Relying entirely on acousto-optic modulators for optical switching, and operating our tapered amplifier diodes with fixed current, should reduce optical intensity transients. In addition to allowing for closer LMT aug-

mentation pulse spacings, this change may limit a potential source of phase noise in ARP interferometers, since intensity has a direct impact on the ARP dynamic phase. Our preliminary demonstration of a symmetric Raman interferometer could be improved upon through use of mutually exclusive, highly efficient Doppler-insensitive and Doppler-sensitive atom optics. High transfer efficiency would prevent population from entering interferometer loss channels, which potentially add spurious phase shifts.

Sensors operating in dynamic environments must generally operate at fast data-rates (>10 Hz), primarily to avoid under-sampling inertial input, but also to improve short-term stability and minimize dead time. Our apparatus currently operates at data-rates of 1–10 Hz, with the prime limitation being small atom signal size at faster rates. To enlarge the signal size, the cold atom recapture efficiency can be improved by (1) eliminating the pusher pulse from the readout sequence and (2) using a higher-bandwidth detector to eliminate time spent resolving bandwidth-limited waveforms of atom fluorescence.

Appendix A

Allan deviations and stability nomenclature

The stability of a precision sensor characterizes the extent to which consecutive measurements deviate from one another. A powerful tool for quantifying stability is the Allan variance $\sigma_y^2(\tau)$. To compute the Allan variance, a series of many measurements from the sensor is acquired over a long period of time. The time series is divided into contiguous bins, each spanning time τ and with average value $\bar{y}_k$ (subscript k denotes the bin number). The Allan variance is given by the mean-squared deviations between consecutive bin averages:

$$\sigma_y^2(\tau) = \frac{1}{2}\left\langle (\bar{y}_{k+1} - \bar{y}_k)^2 \right\rangle . \tag{A.1}$$

The pivotal difference between the standard and Allan variances is that deviations in the former are taken with respect to the full sample mean. The Allan variance, on the other hand, uses deviations between consecutive measurements or measurement averages. Due to the random walks and drifts that commonly occur in measurements from precision sensors, the standard deviation grows without bound over long measurement times and carries little meaning. By comparison, the Allan variance converges and provides a useful metric for stability. In some cases, the Allan variance helps identify time scales at which different types of random noise, such as white or

flicker noise, become dominant. The behavior of these noise processes is shown in Fig. A-1 in an example log-log plot of Allan deviations $\sigma_y(\tau)$.

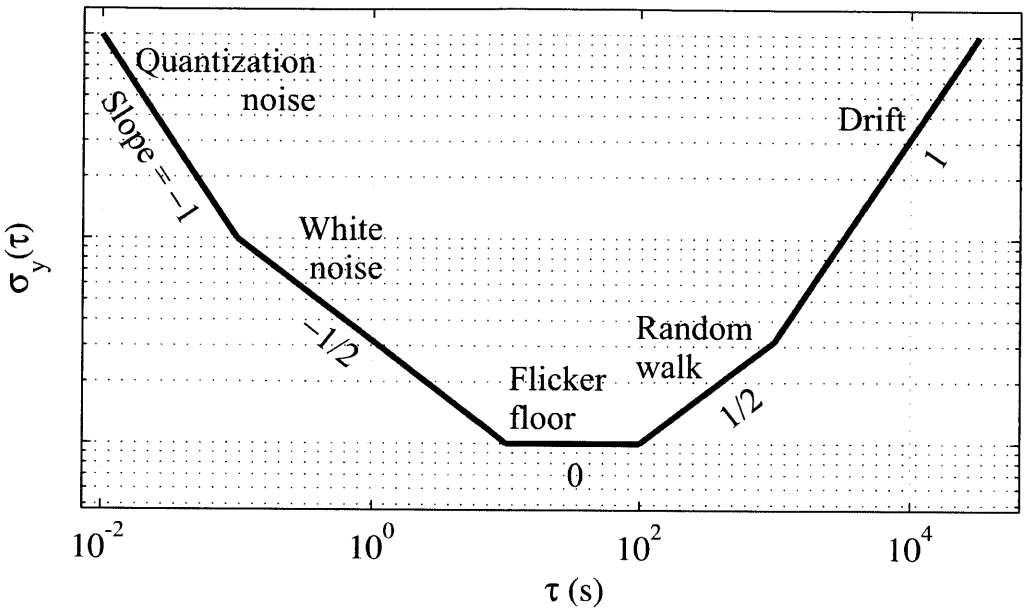

Figure A-1: Example plot of Allan deviations $\sigma_y(\tau)$ for a range of measurement averaging times τ. Different random noise processes produce Allan deviations with distinct slopes (see labels). Averaging over increasing τ benefits the stability up until the flicker floor is reached. For even long τ, random walks and drifts dominate the stability and cause an upturn in the Allan deviations.

When a particular noise process dominates a range of measurement periods τ, the Allan deviations produce a characteristic slope in this log-log plot. White noise, for example, causes $\sigma_y(\tau)$ to trend downward as $\tau^{-1/2}$, indicating that sensor stability improves when measurements are averaged over time scales associated with white noise. This behavior reflects the fact that the standard deviation of the mean for a normally distributed random variable improves as $1/\sqrt{n}$, where n is the number of samples. For this same reason, white noise-limited stability at a given τ improves with higher sampling rate and is therefore quoted in units of [amplitude]$/\sqrt{\text{Hz}}$. The amplitude represents acceleration, rotation rate, or fractional frequency. In the realm of inertial sensing, the stability at short τ is also interchangeably referred to as sensitivity or velocity (angle) random walk in the case of accelerometers (gyroscopes).[1]

[1]These random walks are different from those identified in Fig. A-1, which instead occur in

Averaging measurements beyond time scales associated with flicker noise typically degrades stability, as indicated in Fig. A-1 by the upturn in Allan deviations at times exceeding $\tau = 100$ s. The Allan deviation achieves a minimum at the so-called 'flicker floor," and its value at the corresponding τ is known as bias stability, or "the bucket," in the parlance of inertial sensing. In timekeeping applications, the minimum Allan deviation is called the fractional frequency uncertainty. The best clocks are sometimes not operated long enough for a determination of their flicker floor. In this case, their fractional frequency uncertainties are limited by the total measurement duration.

acceleration and rotation rate for accelerometers and gyroscopes, respectively.

Appendix B

Large area interferometer Monte Carlo simulations

This appendix provides a detailed description of the simulations used in Sec. 5.4.2 to characterize loss of contrast in large area atom interferometers. In broad terms, the simulation calculated scattering amplitudes for internal/momentum basis states (e.g., $|F = 3; p + \hbar k_{\text{eff}}\rangle$, with p being the initial momentum) comprising an atom subjected to Raman, ARP, or composite pulses. A sequence of these pulses produced a large momentum transfer (LMT) interferometer. The scattering amplitudes from each pulse were computed using the approach described in Sec. 2.2.2, which will be discussed further below.

B.1 Spontaneous emission and inhomogeneities in detuning and Rabi rate

Spontaneous emission was an important driver of contrast loss in this work, since LMT interferometers required 5 to 50 times the pulse area of a standard $2\hbar k$ interferometer. The exact pulse area was dependent on augmentation pulse duration t_{aug} and LMT order N. To account for spontaneous emission in simulations, we scaled the predicted contrast values using empirically determined coefficients $(1 - R_{sc})^{4Nt_{aug}+2}$, where t_{aug}

was in units of t_π, and the exponent was the number of π pulses applied. The base of the exponent $1 - R_{sc}$ was the fractional population remaining after a single π pulse. We experimentally found $R_{sc} = 0.004$ by repeatedly applying Tan/Tanh ARP inversions, with $T_\pi = 10t_\pi$, and measuring the resulting oscillation in transition probability. Spontaneous emission caused the oscillation to decay exponentially, as seen in Fig. B-1. Given the wide velocity acceptance of a Tan/Tanh pulse of this duration, population loss due to detuning or Rabi rate inhomogeneity was likely minimal. Therefore, the measured decay rate was attributed entirely to spontaneous emission.

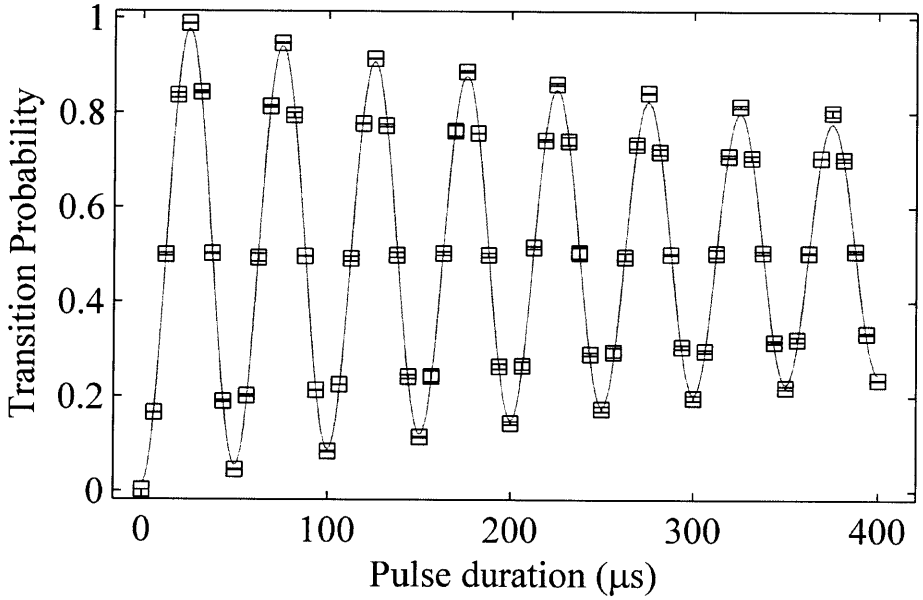

Figure B-1: Empirical determination of spontaneous emission rate. Applying to the atoms a sequence of 16 Tan/Tanh ARP inversions, with $T_\pi = 10t_\pi$, induced decaying oscillations in the transition probability. Squares are measurements and the curve (gray) is a fitted, exponentially decaying sine function. The fractional population decay rate, $R_{sc} = 0.004$ per Raman π pulse, was attributed entirely to spontaneous emission, because population loss from detuning and Rabi rate errors were minimal for such an adiabatic sweep. The Raman π pulse duration was 2.5 μs.

In experiments, interferometer phase measurements were acquired from an ensemble of atoms with varying positions and velocities. Furthermore, the atoms were subjected to the spatially nonuniform intensity profile of a nominally Gaussian laser

beam. Since the fluorescence readout detected an ensemble average of the atom transition probability, it was important to include ensemble effects in our model. Interferometer contrast, for example, can be degraded by detuning and Rabi rate inhomogeneities across the ensemble. To capture such effects, the simulation generated random, normally distributed initial atom velocities and positions. The mean position coincided with the Raman beam axis. In addition, a normalized CCD image of one of the Raman beam intensity profiles, shown in Fig. B-2, scaled the Rabi rate Ω_{eff} as a function of atom position.

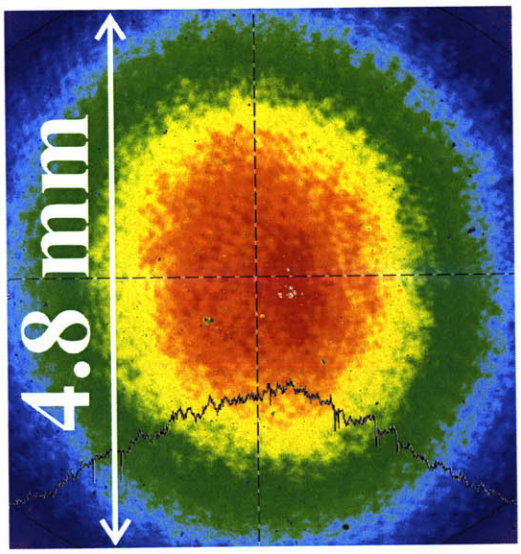

Figure B-2: Central portion of the intensity profile from one Raman beam, used in LMT interferometer simulations. Intensity inhomogeneity was an important aspect of LMT interferometer simulations with ARP pulses, since these pulses were susceptible to intensity-driven dephasing. This beam model was still optimistic, because it accounted for just one of the two Raman beams used in experiments (see Sec. 3.5.2 for implementation). Cold atoms remained within the central red/orange peak during interferometers.

B.2 Scattering amplitudes in large area interferometers

After generating a randomly distributed atom ensemble, scattering amplitudes from the interferometer pulses were calculated. The calculation was done several times for

just the the final beamsplitter pulse, since its Raman phase was varied to produce the interferogram. When the calculation was repeated for all the atoms, the resulting average transition probabilities created interferograms, to which we fit sine functions. Contrast was defined as the amplitude of the fitted sine curve.

The calculation of scattering amplitudes for diffracting wavepackets in LMT interferometers followed the approach described in Sec. 2.2.2. Recall that each Raman transition produces scattering (S) and continuing (C) wavepackets, described pictorially in Fig. 2-6. For standard Raman transitions with constant detuning and intensity, the scattering amplitudes are

$$C = \cos\left(\frac{\Omega_{\text{gen}}t}{2}\right) + i\frac{\delta_{AC}-\delta}{\Omega_{\text{gen}}}\sin\left(\frac{\Omega_{\text{gen}}t}{2}\right) \tag{B.1}$$

$$S = \frac{\Omega_{\text{eff}}}{\Omega_{\text{gen}}}\sin\left(\frac{\Omega_{\text{gen}}t}{2}\right)e^{i\varphi}, \tag{B.2}$$

and their effect on separating wavepackets is described by the equation

$$\mathbf{b}(t) = \begin{cases} C^*(t)|e\rangle - iS(t)|g\rangle, & \text{for } \mathbf{b}(0) = |e\rangle \\ -iS^*(t)|e\rangle + C(t)|g\rangle, & \text{for } \mathbf{b}(0) = |g\rangle \end{cases}. \tag{B.3}$$

Scattering amplitudes for ARP, on the other hand, are determined through numerical integration of Eq. (2.10). Composite pulses based purely on discrete Raman phase shifts can be broken into multiple, contiguous Raman transitions, and can thus be described by Eqs. (B.1) and (B.2).

Scattering diagrams for LMT interferometers must incorporate reversal of the effective Raman wave vector $\mathbf{k}_{\text{eff}}$ (not considered in Sec. 2.2.2), as this reversal is what enables LMT [77, 101]. A scattering diagram for a $10\hbar k$ LMT beamsplitter sequence is shown in Fig. B-3. Examining the number of two-photon recoils of each wavepacket (second number in the ket labels), we find an important new consequence of reversing $\mathbf{k}_{\text{eff}}$: due to these additional recoils, the Raman detunings of wavepackets generated by augmentation pulses change from one pulse to the next. Though the

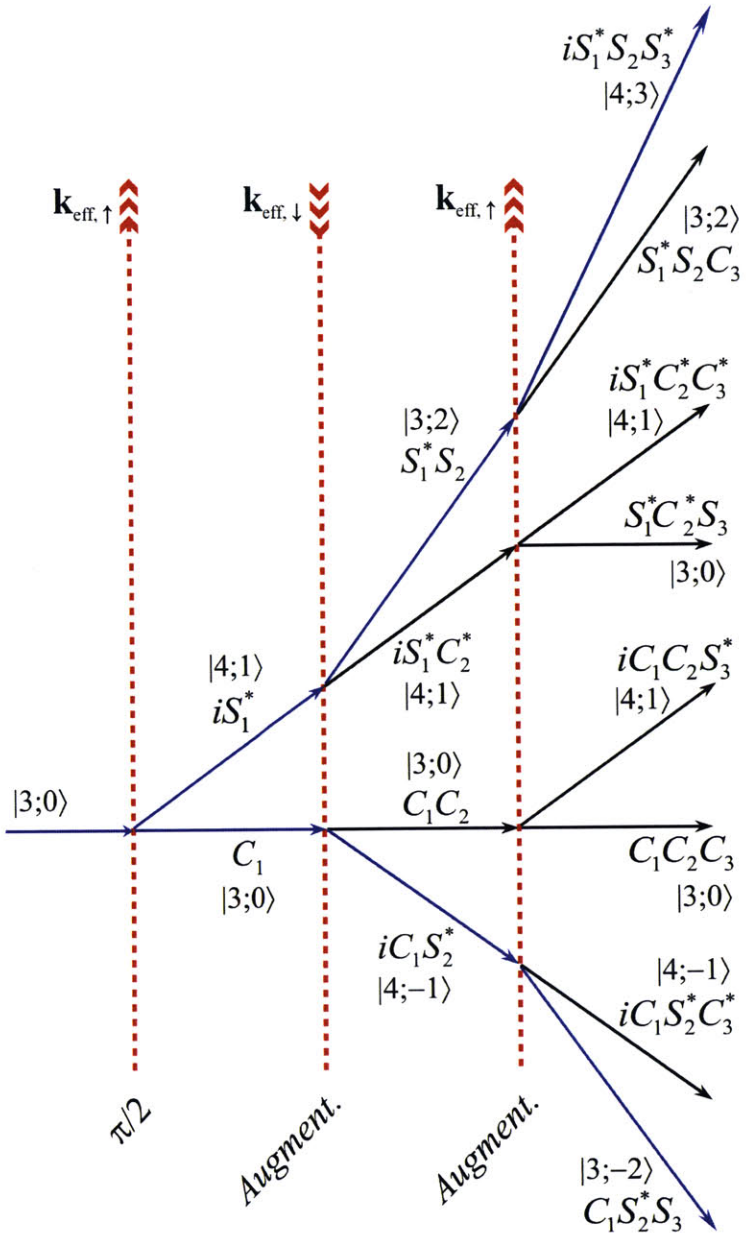

Figure B-3: Scattering diagram for a $10\hbar k$ beamsplitter comprising a Raman $\pi/2$ pulse and two augmentation pulses. Additional augmentation pulses could be added. The primary interferometer paths are blue, loss channels are black, and ket labels indicate the internal hyperfine state, followed by number of two-photon recoils for a particular wavepacket. Raman pulses are represented by the dashed vertical lines. Raman wave vector reversal from one pulse to the next causes the primary paths to diffract father apart, thereby enlarging the effective area (i.e., scale factor) of the interferoemter.

Raman detuning function for a particular wavepacket still takes the form

$$\delta(t) = \omega_1(t) - \omega_2(t) - \left[\omega_{HFS} + \frac{\hbar k_{\text{eff}}^2}{2m} + \mathbf{k}_{\text{eff}} \cdot \dot{\mathbf{z}}\right], \tag{B.4}$$

the additional recoil velocity of the associated *lower ground state* $|F = 3\rangle$ is now included in $\dot{\mathbf{z}}$. We associate $\dot{\mathbf{z}}$ with $|F = 3\rangle$, because scattering amplitudes were derived in Sec. 2.1 in a reference frame co-moving with this state. If, for example, a Raman transition couples $|F = 4; p + n\hbar k_{\text{eff}}\rangle$ to $|F = 3; p + (n+1)\hbar k_{\text{eff}}\rangle$, then $m\dot{\mathbf{z}} = \mathbf{p} + (n+1)\hbar k_{\text{eff}}\hat{\mathbf{z}}$. The definition of $\dot{\mathbf{z}}$ is unchanged if the transition goes from $|F = 3; p + (n+1)\hbar k_{\text{eff}}\rangle$ to $|F = 4; p + n\hbar k_{\text{eff}}\rangle$. Using the correct detuning function, scattering amplitudes are calculated (or determined numerically) for every wavepacket in the interferometer.

Phase factors associated with dwell times and unitary transformations between the j^{th} and $j+1^{\text{th}}$ interferometer pulses (see Sec. 2.2.2 for details) can be grouped together, yielding

$$\Phi_{j \to j+1} \equiv \int_0^{t_{j+1}} \delta_{j+1}(t)dt - \int_0^{t_j + \tau_j} \delta_j(t)dt. \tag{B.5}$$

Again, δ_j and δ_{j+1} may not be equal.

B.3 Reduction of computation time

Calculating scattering amplitudes for every wavepacket in an LMT interferometer can be computationally inefficient for large LMT orders and ARP augmentation pulses, which require numerical integration. For an order-N LMT interferometer with ARP augmentation pulses, the numerical integration described in Sec. B.2 must be performed 2^{4N+3} times for every atom. This exponential scaling makes a complete calculation intractable even for relatively small N. The number of integrations can be drastically reduced to $8N + 4$ per atom by calculating scattering amplitudes for just the primary interfering arms, pictured in Fig. 5-1. We used this approach to produce the simulated contrast values reported in Sec. 5.4.2. The truncated calculation

is suitable if loss channels do not interfere and detailed knowledge of interferometer background offsets is unnecessary. Sources of interfering loss channels in an LMT interferometer of order N are loops corresponding to all orders $<N$ (see Fig. 5-1). However, experimental observation of the correct LMT phase response to acceleration suggests that loss channels did not substantially perturb the interferometer.

Computation times can also be reduced, while retaining all scattering amplitudes, if the spatial separation between wavepackets is ignored. This assumption is relevant to the short dwell times considered in this thesis, and generally applies when external potentials are uniform across both interfering wavepackets. In this case, amplitudes from wavepackets that carry the same internal and external state labels are added coherently after every pulse and thus combined. Since each augmentation pulse adds just two new momentum states, the number of per-pulse integrations increase linearly and the total number of integrations scales, to leading order, with N^2.

Bibliography

[1] D. MacKenzie. *Inventing Accuracy: A Historical Sociology of Nuclear Missle Guidance.* The MIT Press, Cambridge, 1993.

[2] R. Hopkins, J. Miola, W. Sawyer, R. Setterlund, and B. Dow. The silicon oscillating accelerometer: A high-performance MEMS accelerometer for precision navigation and strategic guidance applications. In *Proceedings of the 2005 National Technical Meeting of The Institute of Navigation*, pages 970–979, January 2005.

[3] Honeywell. *Q-Flex QA-3000 Accelerometer data sheet*, 2006.

[4] N. Barbour and G. Schmidt. Inertial sensor technology trends. *IEEE Sensors Journal*, 1(4):332–339, Dec. 2001.

[5] Z.-K. Hu, B.-L. Sun, X.-C. Duan, M.-K. Zhou, L.-L. Chen, S. Zhan, Q.-Z. Zhang, and J. Luo. Demonstration of an ultrahigh-sensitivity atom-interferometry absolute gravimeter. *Phys. Rev. A*, 88:043610, Oct 2013.

[6] N. Barbour. Inertial components - past, present, and future. In *2001 AIAA Guidance, Navigation and Control Conference*, pages 1–11, 2001.

[7] T. A. Berkoff and A. D. Kersey. Experimental demonstration of a fiber Bragg grating accelerometer. *Photonics Technology Letters, IEEE*, 8(12):1677–1679, Dec 1996.

[8] M. A. Kasevich and S. Chu. Measurement of the gravitational acceleration of an atom with a light-pulse atom interferometer. *App. Phys. B*, 54(5):321–332, 1992.

[9] P. Gillot, O. Francis, A. Landragin, F. Pereira Dos Santos, and S. Merlet. Stability comparison of two absolute gravimeters: optical versus atomic interferometers. *Metrologia*, 51(5):L15, 2014.

[10] A. Peters, K. Y. Ching, and S. Chu. High-precision gravity measurements using atom interferometry. *Metrologia*, 38:25–61, 2001.

[11] J. M. McGuirk, G. T. Foster, J. B. Fixler, M. J. Snadden, and M. A. Kasevich. Sensitive absolute-gravity gradiometry using atom interferometry. *Phys. Rev. A*, 65:033608, 2002.

[12] G. Rosi, F. Sorrentino, L. Cacciapuoti, M. Prevedelli, and G. M. Tino. Precision measurement of the newtonian gravitational constant using cold atoms. *Nature*, 510:518–521, June 2014.

[13] F. Sorrentino, Q. Bodart, L. Cacciapuoti, Y.-H. Lien, M. Prevedelli, G. Rosi, L. Salvi, and G. M. Tino. Sensitivity limits of a Raman atom interferometer as a gravity gradiometer. *Phys. Rev. A*, 89:023607, Feb 2014.

[14] J. H. Gundlach and S. M. Merkowitz. Measurement of Newton's constant using a torsion balance with angular acceleration feedback. *Phys. Rev. Lett.*, 85:2869–2872, Oct 2000.

[15] T. L. Gustavson, A. Landragin, and M. A. Kasevich. Rotation sensing with a dual atom-interferometer Sagnac gyroscope. *Classical and Quantum Gravity*, 17(12):2385, 2000.

[16] D. S. Durfee, Y. K. Shaham, and M. A. Kasevich. Long-term stability of an area-reversible atom-interferometer Sagnac gyroscope. *Phys. Rev. Lett.*, 97:240801, Dec 2006.

[17] K. U. Schreiber, T. Klügel, J.-P. R. Wells, R. B. Hurst, and A. Gebauer. How to detect the Chandler and the annual wobble of the earth with a large ring laser gyroscope. *Phys. Rev. Lett.*, 107:173904, Oct 2011.

[18] S. J. Sanders, L. K. Strandjord, and D. Mead. Fiber optic gyro technology trends - a Honeywell perspective. In *Optical Fiber Sensors Conference Technical Digest, 2002. OFS 2002, 15th*, pages 5–8 vol.1, May 2002.

[19] T. P. Heavner, E. A. Donley, F. Levi, G. Costanzo, T. E. Parker, J. H. Shirley, N. Ashby, S. Barlow, and S. R. Jefferts. First accuracy evaluation of NIST-F2. *Metrologia*, 51(3):174, 2014.

[20] M. A. Lombardi. Microsecond Accuracy at Multiple Sites: Is It Possible Without GPS? *IEEE Instrumentation and Measurement Magazine*, pages 14–21, Oct 2012.

[21] Microsemi. *5071A data sheet*, 2014.

[22] D. W. Allan, N. Ashby, and C. Hodge. The science of timekeeping. *Hewlett Packard Application Note 1289*, 1997.

[23] Microsemi. *Quantum^{TM} SA.45s CSAC data sheet*, 2014.

[24] M. J. Mescher, R. Lutwak, and M. Varghese. An ultra-low-power physics package for a chip-scale atomic clock. In *Solid-State Sensors, Actuators and Microsystems, 2005. Digest of Technical Papers. The 13th International Conference on TRANSDUCERS '05*, volume 1, pages 311–316 Vol. 1, June 2005.

[25] R. Lutwak. The chip-scale atomic clock - recent developments. In *Frequency Control Symposium, 2009 Joint with the 22nd European Frequency and Time forum. IEEE International*, pages 573–577, April 2009.

[26] J. Kitching, L. Hollberg, S. Knappe, and R. Wynands. Compact atomic clock based on coherent population trapping. *Electronics Letters*, 37:1449–1451(2), November 2001.

[27] S. Knappe, V. Shah, P. D. D. Schwindt, L. Hollberg, J. Kitching, L.-A. Liew, and J. Moreland. A microfabricated atomic clock. *Applied Physics Letters*, 85(9):1460–1462, 2004.

[28] M. Lombardi. Fundamentals of time and frequency. In R. H. Bishop, editor, *The Mechatronics Handbook*. CRC Press, Boca Raton, 2002.

[29] B. J. Bloom, T. L. Nicholson, J. R. Williams, S. L. Campbell, M. Bishof, X. Zhang, W. Zhang, S. L. Bromley, and J. Ye. An optical lattice clock with accuracy and stability at the 10^{18} level. *Nature*, 506(7486):71 – 75, 2014.

[30] C. Monroe, H. Robinson, and C. Wieman. Observation of the cesium clock transition using laser-cooled atoms in a vapor cell. *Opt. Lett.*, 16(1):50–52, Jan 1991.

[31] J. Sebby-Strabley, K. Salit, K. Nelson, J. Ridley, and J. Kriz. Cold atom micro primary standard (CAMPS). In *Proceedings of the 43th Annual Precise Time and Time Interval Meeting*, pages 231–238, Nov 2011.

[32] K. Nelson, K. Salit, J. Kriz, D. Sandquist, and J. Sebby-Strabley. Cold atom micro primary standard (CAMPS). In *Position Location and Navigation Symposium (PLANS), 2012 IEEE/ION*, pages 1094–1098, April 2012.

[33] F.-X. Esnault, E. Blanshan, E. N. Ivanov, R. E. Scholten, J. Kitching, and E. A. Donley. Cold-atom double-Λ coherent population trapping clock. *Phys. Rev. A*, 88:042120, Oct 2013.

[34] Y.-Y. Jau, H. Partner, P. D. D. Schwindt, J. D. Prestage, J. R. Kellogg, and N. Yu. Low-power, miniature ^{171}Yb ion clock using an ultra-small vacuum package. *Applied Physics Letters*, 101(25):253518, 2012.

[35] O. Carnal and J. Mlynek. Young's double-slit experiment with atoms: A simple atom interferometer. *Phys. Rev. Lett.*, 66(21):2689–2692, 1991.

[36] D. W. Keith, C. R. Ekstrom, Q. A. Turchette, and D. E. Pritchard. An interferometer for atoms. *Phys. Rev. Lett.*, 66(21):2693–2696, 1991.

[37] F. Riehle, T. Kisters, A. Witte, and J. Helmcke. Optical Ramsey spectroscopy in a rotating frame: Sagnac effect in a matter-wave interferometer. *Phys. Rev. Lett.*, 67(2):177–180, 1991.

[38] M. A. Kasevich and S. Chu. Atomic interferometry using stimulated Raman transitions. *Phys. Rev. Lett.*, 67(2):181–184, 1991.

[39] S. Gerlich, S. Eibenberger, M. Tomandl, S. Nimmrichter, K. Hornberger, P. J. Fagan, J. Tuxen, M. Mayor, and M. Arndt. Quantum interference of large organic molecules. *Nat. Commun.*, 2:263, 2011.

[40] A. W. Overhauser and R. Colella. Experimental test of gravitationally induced quantum interference. *Phys. Rev. Lett.*, 33(20):1237–1239, 1974.

[41] R. Colella ans A. W. Overhauser and S. A. Werner. Observation of gravitationally induced quantum interference. *Phys. Rev. Lett.*, 34(23):1472–1474, 1975.

[42] A. D. Cronin, J. Schmiedmayer, and D. E. Pritchard. Optics and interferometry with atoms and molecules. *Revs. Mod. Phys.*, 81:1051–1129, 2009.

[43] H. J. Metcalf and P. van der Straten. *Laser Cooling and Trapping.* Springer-Verlag, New York, 1999.

[44] E. L. Raab, M. Prentiss, A. Cable, S. Chu, and D. E. Pritchard. Trapping of neutral sodium atoms with radiation pressure. *Phys. Rev. Lett.*, 59:2631–2634, 1987.

[45] D. L. Butts, J. M. Kinast, B. P. Timmons, and R. E. Stoner. Light pulse atom interferometry at short interrogation times. *J. Opt. Soc. Am. B*, 28:416–421, 2011.

[46] D. L. Butts. *Light pulse atom interferometry at short interrogation times for inertial navigation.* PhD thesis, Massachusetts Institute of Technology, 2012.

[47] H. J. McGuinness, A. V. Rakholia, and G. W. Biedermann. High data-rate atom interferometer for measuring acceleration. *Applied Physics Letters*, 100(1):011106, 2012.

[48] A. V. Rakholia, H. J. McGuinness, and G. W. Biedermann. Dual-axis high-data-rate atom interferometer via cold ensemble exchange. *Phys. Rev. Applied*, 2:054012, Nov 2014.

[49] S. Wu, E. Su, and M. Prentiss. Demonstration of an area-enclosing guided-atom interferometer for rotation sensing. *Phys. Rev. Lett.*, 99:173201, 2007.

[50] G. Stern, B. Battelier, R. Geiger, G. Varoquaux, A. Villing, F. Moron, O. Carraz, N. Zahzam, Y. Bidel, W. Chaibi, F. Pereira Dos Santos, A. Bresson, A. Landragin, and P. Bouyer. Light-pulse atom interferometry in microgravity. *Euro. Phys. Journ. D*, 53:353–357, 2009.

[51] R. Geiger, V. Menoret, G. Stern, N. Zahzam, P. Cheinet, B. Battelier, A. Villing, F. Moron, M. Lours, Y. Bidel, A. Bresson, A. Landragin, and P. Bouyer. Detecting inertial effects with airborne matter-wave interferometry. *Nat. Commun.*, 2:474, 2011.

[52] D. Butts, M. Bottkol, T. Thorvaldsen, S. Lim, R. Stoner, J. Choy, J. Brown, P. Sherman, M. Chaparala, S. P. Smith, D. M. S. Johnson, A. Rakholia, G. Biedermann, and M. Berarducci. A hybrid approach to an atom-interferometer-based inertial measurement unit. In *Joint Navigation Conference*, June 2015.

[53] G. Biedermann. *Gravity Tests, Differential Accelerometry, and Interleaved Clocks with Cold Atom Interferometers*. PhD thesis, Stanford University, 2007.

[54] X. Wu. *Gravity Gradient Survey with a Mobile Atom Interferometer*. PhD thesis, Stanford University, 2009.

[55] K. Takase. *Precision Rotation Rate Measurements with a Mobile Atom Interferometer*. PhD thesis, Stanford University, 2008.

[56] J. K. Stockton, K. Takase, and M. A. Kasevich. Absolute geodetic rotation measurement using atom interferometry. *Phys. Rev. Lett.*, 107:133001, Sep 2011.

[57] F. Bloch, W. W. Hansen, and M. Packard. Nuclear induction. *Phys. Rev.*, 69:127, 1946.

[58] M. H. Levitt and R. Freeman. NMR population inversion using a composite pulse. *J. Magn. Reson.*, 33:473–476, 1979.

[59] A. Abgragam. *Principles of Nuclear Magnetic Resonance*. Oxford University Press, 1996.

[60] C. J. Hardy, W. A. Edelstein, and D. Vatis. Efficient adiabatic fast passage for NMR population inversion in the presence of radiofrequency field inhomogeneity and frequency offsets. *J. Magn. Reson*, 66:470–482, 1986.

[61] S. Chelkowski and G. N. Gibson. Adiabatic climbing of vibrational ladders using Raman transitions with a chirped pump laser. *Phys. Rev. A*, 52(5):R3417–R3420, 1995.

[62] B. W. Shore, K. Bergmann, A. Kuhn, S. Schiemann, J. Oreg, and J. H. Eberly. Laser-induced population transfer in multistate systems: A comparative study. *Phys. Rev. A*, 45(7):5297–5300, 1992.

[63] J. Bateman and T. Freegarde. Fractional adiabatic passage in two-level systems: Mirrors and beam splitters for atomic interferometry. *Phys. Rev. A*, 76:013416, Jul 2007.

[64] A. Dunning, R. Gregory, J. Bateman, N. Cooper, M. Himsworth, J. A. Jones, and T. Freegarde. Composite pulses for interferometry in a thermal cold atom cloud. *Phys. Rev. A*, 90:033608, Sep 2014.

[65] J. Baum, R. Tycko, and A. Pines. Broadband and adiabatic inversion of a two-level system by phase-modulated pulses. *Phys. Rev. A*, 32(6):3435–3477, 1985.

[66] A. Tannus and M. Garwood. Improved performance of frequency-swept pulses using offset-independent adiabaticity. *J. Magn. Reson. A*, 120:133–37, 1996.

[67] T.-L. Hwang, P. C. M. van Zijl, and M. Garwood. Fast broadband inversion by adiabatic pulses. *J. Magn. Reson*, 133:200–203, 1998.

[68] E. Kupce and R. Freeman. Optimized adiabatic pulses for wideband spin inversion. *J. Magn. Reson. A*, 118:299–303, 1996.

[69] M. Garwood and L. DelaBarre. The return of the frequency sweep: Designing adiabatic pulses for contemporary NMR. *J. Magn. Reson.*, 153:155–177, 2001.

[70] M. H. Levitt. Composite pulses. *Prog. Nucl. Magn. Reson. Spectrosc.*, 18(4):61–122, 1986.

[71] M. M. T. Loy. Observation of population inversion by optical adiabatic rapid passage. *Phys. Rev. Lett.*, 32(15):814–817, 1974.

[72] L. S. Goldner, C. Gerz, J. C. Spreeuw, S. L. Rolston, C. I. Westbrook, and W. D. Phillips. Momentum transfer in laser-cooled cesium by adiabatic passage in a light field. *Phys. Rev. Lett.*, 72(7):997–1000, 1994.

[73] N. V. Vitanov and S. Stenholm. Analytic properties and effective two-level problems in stimulated Raman adiabatic passage. *Phys. Rev. A*, 55(1):648–660, 1997.

[74] N. V. Vitanov, T. Halfmann, B. W. Shore, and K. Bergmann. Laser-induced population transfer by adiabatic passage techniques. *Annu. Rev. Phys. Chem.*, 52:763–809, 2001.

[75] M. Weitz, B. C. Young, and S. Chu. Atomic interferometer based on adiabatic population transfer. *Phys. Rev. Lett.*, 73(19):2563–2566, 1994.

[76] B. C. Young. *A Measurement of the Fine Structure Constant Using Atom Interferometry.* PhD thesis, Stanford University, 1997.

[77] J. McGuirk, M. Snadden, and M. A. Kasevich. Large area light-pulse atom interferometry. *Phys. Rev. Lett.*, 85:4498–4501, Nov 2000.

[78] S.-W. Chiow, T. Kovachy, H.-C. Chien, and M. A. Kasevich. $102\hbar k$ large area atom interferometers. *Phys. Rev. Lett.*, 107:130403, Sep 2011.

[79] H. Muller, S.-W. Chiow, S. Herrmann, and S. Chu. Atom interferometers with scalable enclosed area. *Phys. Rev. Lett.*, 102:240403, Jun 2009.

[80] T. Kovachy, J. M. Hogan, D. M. S. Johnson, and M. A. Kasevich. Optical lattices as waveguides and beam splitters for atom interferometry: An analytical treatment and proposal of applications. *Phys. Rev. A*, 82:013638, Jul 2010.

[81] R. E. Stoner, D. L. Butts, J. M. Kinast, and B. Timmons. Analytical framework for dynamic light pulse atom interferometry at short interrogation times. *J. Opt. Soc. Am. B*, 28(10):2418–2429, Oct 2011.

[82] B. C. Young, M. A. Kasevich, and S. Chu. Precision atom interferometry with light pulses. In P. R. Berman, editor, *Atom Interferometry*, pages 363 – 406. Academic Press, San Diego, 1997.

[83] K. Moler, D. S. Weiss, M. A. Kasevich, and S. Chu. Theoretical analysis of velocity-selective Raman transitions. *Phys. Rev. A*, 45:342–348, Jan 1992.

[84] P. Storey and C. Cohen-Tannoudji. The Feynman path integral approach to atomic interferometry. A tutorial. *J. Phys. II France*, 4:1999–2027, 1994.

[85] J. J. Sakurai and Jim Napolitano. *Modern Quantum Mechanics*. Addison-Wesley, 2011.

[86] M. Bason, M. Viteau, N. Malossi, P. Huillery, E. Arimondo, D Ciampini, R. Fazio, V. Giovannetti, R. Mannella, and O. Morsch. High-fidelity quantum driving. *Nat. Phys.*, 8:147–152, Feb 2012.

[87] M. A. Kasevich, E. Riis, S. Chu, and R. G. DeVoe. rf spectroscopy in an atomic fountain. *Phys. Rev. Lett.*, 63:612–615, Aug 1989.

[88] S. R. Jefferts, J. Shirley, T. E. Parker, T. P. Heavner, D. M. Meekhof, C. Nelson, F. Levi, G. Costanzo, A. De Marchi, R. Drullinger, L. Hollberg, W. D. Lee, and F. L. Walls. Accuracy evaluation of NIST-F1. *Metrologia*, 39(4):321, 2002.

[89] K. B. Davis, M. O. Mewes, M. R. Andrews, N. J. van Druten, D. S. Durfee, D. M. Kurn, and W. Ketterle. Bose-Einstein condensation in a gas of sodium atoms. *Phys. Rev. Lett.*, 75:3969–3973, Nov 1995.

[90] M. H. Anderson, J. R. Ensher, M. R. Matthews, C. E. Wieman, and E. A. Cornell. Observation of Bose-Einstein condensation in a dilute atomic vapor. *Science*, 269(5221):198–201, 1995.

[91] J. Rudolph, W. Herr, C Grzeschik, T. Sternke, A. Grote, M. Popp, D. Becker, H. Mutinga, H. Ahlers, A. Peters, C. Lammerzahel, K. Sengstock, N. Gaaloul, W. Ertmer, and E. Rasel. A high-flux BEC source for mobile atom interferometers. *arXiv*, (:1501.00403), Jan 2015.

[92] K. I. Lee, J. A. Kim, H. R. Noh, and W. Jhe. Single-beam atom trap in a pyramidal and conical hollow mirror. *Opt. Lett.*, 21(15):1177–1179, 1996.

[93] Q. Bodart, S. Merlet, N. Malossi, F. Pereira Dos Santos, P. Bouyer, and A. Landragin. A cold atom pyramidal gravimeter with a single laser beam. *Appl. Phys. Lett.*, 96:134101, 2010.

[94] J. F. Barry, D. J. McCarron, E. B. Norrgard, M. H. Steinecker, and D. DeMille. Magneto-optical trapping of a diatomic molecule. *Nature*, 512:286âĂŞ289, Aug 2014.

[95] T. Muller, M. Gilowski, M. Zaiser, P. Berg, Ch. Schubert, T. Wendrich, W. Ertmer, and E. M. Rasel. A compact dual atom interferometer gyroscope based on laser-cooled rubidium. *The European Physical Journal D*, 53(3):273–281, 2009.

[96] K. E. Gibble, S. Kasapi, and S. Chu. Improved magneto-optic trapping in a vapor cell. *Opt. Lett.*, 17(7):526–528, Apr 1992.

[97] D. W. Preston. Doppler-free saturated absorption: Laser spectroscopy. *Am. J. Phys.*, 64:1432–1436, Nov 1996.

[98] I. Dotsenko. *Raman spectroscopy of single atoms.* PhD thesis, Institute of Applied Physics, University of Bonn, 2002.

[99] A. Peters. *High-Precision Gravity Measurements Using Atom Interferometry.* PhD thesis, Stanford University, 1998.

[100] N. Malossi, Q. Bodart, S. Merlet, T. Leveque, A. Landragin, and F. Pereira Dos Santos. Double diffraction in an atomic gravimeter. *Phys. Rev. A*, 81:013617, 2010.

[101] D. L. Butts, K. Kotru, J. M. Kinast, A. M. Radojevic, B. P. Timmons, and R. E. Stoner. Efficient broadband Raman pulses for large-area atom interferometry. *J. Opt. Soc. Am. B*, 30(4):922–927, Apr 2013.

[102] K. Kotru, J. M. Brown, D. L. Butts, J. M. Kinast, and R. E. Stoner. Robust Ramsey sequences with Raman adiabatic rapid passage. *Phys. Rev. A*, 90:053611, Nov 2014.

[103] N. Ramsey. A molecular beam resonance method with separated oscillating fields. *Phys. Rev.*, 78(6):695–699, 1950.

[104] V. Shah, R. Lutwak, R. Stoner, and M. Mescher. A compact and low-power cold atom clock. In *Frequency Control Symposium (FCS), 2012 IEEE International*, pages 1–6, May 2012.

[105] F.-X. Esnault, J. Kitching, and E. A Donley. A compact cold-atom frequency standard based on coherent population trapping. In *Frequency Control Symposium (FCS), 2012 IEEE International*, pages 1–3, May 2012.

[106] E. A. Burt and W. M. Klipstein. The cesium physics package design for the PARCS experiment. In *Frequency Control Symposium and Exposition, 2004. Proceedings of the 2004 IEEE International*, pages 71–79, Aug 2004.

[107] J. E. Thomas, P. R. Hemmer, S. Ezekiel, C. C. Leiby, R. H. Picard, and C. R. Willis. Observation of Ramsey fringes using a stimulated, resonance Raman transition in a sodium atomic beam. *Phys. Rev. Lett.*, 48:867–870, Mar 1982.

[108] M. Weitz, B. C. Young, and S. Chu. Atom manipulation based on delayed laser pulses in three- and four-level systems: Light shifts and transfer efficiencies. *Phys. Rev. A*, 50:2438–2444, Sep 1994.

[109] B. Canuel, F. Leduc, D. Holleville, A. Gauguet, J. Fils, A. Virdis, A. Clairon, N. Dimarcq, Ch. J. Bordé, A. Landragin, and P. Bouyer. Six-axis inertial sensor using cold-atom interferometry. *Phys. Rev. Lett.*, 97:010402, Jul 2006.

[110] S. Dimopoulos, P. Graham, J. Hogan, M. A. Kasevich, and S. Rajendran. Atomic gravitational wave interferometric sensor. *Phys. Rev. D*, 78:122002, Dec 2008.

[111] S. Dimopoulos, P. W. Graham, J. M. Hogan, and M. A. Kasevich. General relativistic effects in atom interferometry. *Phys. Rev. D*, 78:042003, Aug 2008.

[112] A. Sugarbaker. *Atom Interferometry in a 10 m Tower*. PhD thesis, Stanford University, 2014.

[113] H. Müller, S.-W. Chiow, Q. Long, S. Herrmann, and S. Chu. Atom interferometry with up to 24-photon-momentum-transfer beam splitters. *Phys. Rev. Lett.*, 100:180405, May 2008.

[114] P Clade, S. Guellati-Khélifa, F. Nez, and F. Biraben. Large momentum beam splitter using bloch oscillations. *Phys. Rev. Lett.*, 102:240402, Jun 2009.

[115] B. Everitt and D. J. Hand. *Finite Mixture Distributions*. Monographs on applied probability and statistics. Chapman and Hall, 1981.

[116] D. M. S. Johnson. *Long Baseline Atom Interferometry*. PhD thesis, Stanford University, 2011.

[117] T. Leveque, A. Gauguet, F. Michaud, F. Pereira Dos Santos, and A. Landragin. Enhancing the area of a Raman atom interferometer using a versatile double-diffraction technique. *Phys. Rev. Lett.*, 103:080405, 2009.